第 13 回
核燃焼プラズマ
統合コード研究会

13th Burning Plasma Simulation Initiative (BPSI) Meeting

日時：2015 年 12 月 10 日(木)－11 日(金)
場所：九州大学筑紫キャンパス
応用力学研究所 2 階大会議室

第 13 回核燃焼プラズマ統合コード研究会

13th Burning Plasma Simulation Initiative (BPSI) Meeting

(Ver.3)

日時：2015 年 12 月 10 日(木)－11 日(金)
場所：九州大学筑紫キャンパス　応用力学研究所 2 階大会議室

(18 min talk+7 min discuss or (15 or 10) min talk+5min discuss)

12 月 10 日(木)

9:00 – 9:10 はじめに 福山 (京大)
(座長：糟谷)
9:10 – 9:35 講演 1-1 矢木 (原子力機構)
Simulation study on transport barrier in tokamak plasmas
9:35 – 10:00 講演 1-2 林 (原子力機構)
Integrated modeling of impurity transport in core and SOL/divertor plasmas
10:00 – 10:15 講演 1-3 前田 (京大)
Heat transport simulation of H/He experiment plasma in LHD
10:15 – 10:40 講演 1-4 村上 (京大)
Integrated simulation of deuterium plasma experiment of LHD

10:40 – 10:55 休憩

(座長：小菅)
10:55 – 11:20 講演 1-5 福山 (京大)
Analysis of EC wave propagation in high-density tokamaks
11:20 – 11:35 講演 1-6 池田 (京大)
Particle simulation of ECR plasma production in tokamaks
11:35 – 11:50 講演 1-7 二口 (京大)
Kinetic linear stability analysis of Alfven eigenmode in tokamaks

11:50 – 13:00 昼休み

(座長：本多)
13:00 – 13:25 講演 2-1 登田 (核融合研)
Progress in applying gyrokinetic heat diffusivity model to transport simulations for helical plasmas

13:25 – 13:50　講演 2-2　　沼波（核融合研）
Sensitivity and prediction of plasma profile in turbulent transport of helical plasmas
13:50 – 14:15　講演 2-3　　仲田（核融合研）
Multi-species ITG-TEM turbulence simulations in ITER D-T-He plasma
14:15 – 14:40　講演 2-4　　糟谷（九大）
Simulation study of turbulence and diagnostic in toroidal plasmas

14:40 – 14:55　休憩

(座長：林)
14:55 – 15:20　講演 2-5　　本多（原子力機構）
Development of the fluid-type transport code on the flux coordinates in tokamaks
15:20 – 15:45　講演 2-6　　Nicolas（核融合研）
Bifurcation of the interchange mode growth rate and rotation frequency due to the perpendicular heat conductivity
15:45 – 16:10　講演 2-7　　奴賀（京大）
Fokker-Planck simulation for runaway electron generation including the hot-tail effect
16:10 – 16:25　講演 2-8　　永井（京大）
Burning plasma start-up simulation by the TASK code
16:25 – 16:40　休憩

(座長：福山)
16:40 – 17:05　講演 2-9　　大澤（九大）
Hydrogen isotope trapped in tungsten vacancy
17:05 – 17:30　講演 2-10　　佐々木（九大）
Eigenmode analysis of geodesic acoustic modes driven by fast ions
17:30 – 17:55　講演 2-11　　小菅（九大）
Analysis of triplet term in parallel momentum flux

17:55　散会

19:30 – 22:00　懇親会（十徳や博多駅筑紫口店にて）

12 月 11 日(金)

9:00 – 9:05 事務連絡

(座長：小関)

9:05 – 9:30 講演 3-1 河村 (核融合研)
Transport analysis of impurity in the LHD peripheral region during neon gas-puff

9:30 – 9:55 講演 3-2 滝塚 (阪大)
Bohm criterion and virtual diverter model for SOL-divertor simulation

9:55 – 10:15 講演 3-3 東郷 (東大)
Numerical analysis of the effects of radial plasma diffusion on the detached divertor plasmas

10:15 – 10:30 休憩

(座長：矢木)

10:30 – 10:55 講演 3-4 横山 (核融合研)
Statistical analysis for deducing "transport model" in LHD plasmas (continued)

10:55 – 11:20 講演 3-5 小関 (原子力機構)
Predictive simulation of fusion plasma by data assimilation

11:20 – 11:45 講演 3-6 藤田 (名大)
Development of PHZ pinch model with plasma rotation effects on particle orbit

11:45 – 12:00 まとめ 糟谷 (九大)

12:00 – 13:00 昼休み

13:00 – 17:00 核融合エネルギーフォーラムサブクラスター会合

17:00 散会

Simulation study on transport barrier in tokamak plasmas

M. Yagi, H. Seto, Y. W. Cho[1], and T. S. Hahm[1]

Japan Atomic Energy Agency, Rokkasho, Aomori, Japan
[1]Seoul National University, Seoul 151-744, Republic of Korea

1. Introduction

To understand physical mechanism of transport barrier formation is a crucial issue for designing advanced operation scenario in JT-60SA and ITER. There are 4 approaches to solve this problem. Namely, (1) 1 dimensional transport model combined with local gyro-kinetic model such as GS2, TGLF. TRINITY code is an example for this approach[1]. (2) Two-fluid model taking account of neoclassical transport. CENTRI code is an example for this approach[2]. However, it only covers MHD scale, practically (n < 20, where n is toroidal mode number). (3) Global gyro-fluid model where the neoclassical transport is usually simplified. (4) Global gyro-kinetic model where full electron dynamics is still difficult to handle. In JAEA, the project for multi-scale simulation with transport/MHD is going on. (1) TRESS(transport code)+GKV[3], (2) LHTOK Project (IFERC-CSC): The neoclassical flows are implemented into BOUT++ code to investigate L/H transition and ETB formation[4]. (3) MS_Turb Project (IFERC-CSC): The neoclassical flows are implemented into GF-ITG code to revisit ITB formation investigated by Tokunaga et al[5]. (4) Near future. In this paper, the third part is briefly reported.

2. Model equations

GF-ITG code consists of three field equations(ion continuity equation, parallel momentum equation and ion temperature evolution equation)[5]

$$\frac{dW}{dt}+\kappa_n\frac{1}{r}\frac{\partial\Phi}{\partial\vartheta}+A\nabla_{//}V=\varepsilon_a\hat{\omega}_d F+\rho_*\frac{q}{\varepsilon}\mu_1\frac{1}{r}\frac{\partial}{\partial r}(rU_p)-\rho_*^2\mu\nabla_\perp^4 F \tag{1}$$

$$\frac{dV}{dt}=-A\nabla_{//}F+4\mu\nabla_\perp^2 V-\mu_1 U_p-A\sqrt{\frac{1}{\tau}}\frac{2}{5}\sqrt{\pi}\left|k_{//}\right|V+A\frac{2}{5}\frac{1}{\tau}\nabla_{//}T \tag{2}$$

$$\frac{3}{2}\left(\frac{dT}{dt}+\kappa_T\frac{1}{r}\frac{\partial\Phi}{\partial\vartheta}\right)-\left(\frac{dn}{dt}+\kappa_n\frac{1}{r}\frac{\partial\Phi}{\partial\vartheta}\right)=\frac{5}{2\tau}\varepsilon_a\hat{\omega}_d T-\frac{9}{5\sqrt{\pi}}A\left|\nabla_{//}\right|T+\frac{2}{5}A\nabla_{//}V+\chi_\perp\nabla_\perp^2 T+S_T\delta_{0,0} \tag{3}$$

where $W=n-\nabla_\perp^2 F$, $n=\Phi-\langle\Phi\rangle$, $F=\Phi+p/\tau$, $p=n+T$. The magnetic curvature operator is given by

$$\hat{\omega}_d=2\cos\vartheta\frac{1}{r}\frac{\partial}{\partial\vartheta}+2\sin\vartheta\frac{\partial}{\partial r} \tag{4}$$

The poloidal flow is given by

$$U_p = V + \rho_* \frac{q}{\varepsilon}\frac{\partial}{\partial r}\left(F - \kappa_{nc} T\right) \tag{5}$$

The neoclassical viscosities are given by[6,7]

$$\mu_1 = \frac{0.66\varepsilon^{1/2}\nu_i}{(1+1.03\nu_{*i}^{1/2}+0.31\nu_{*i})(1+0.66\varepsilon^{3/2}\nu_{*i})} \tag{6}$$

$$\kappa_{nc} = \frac{1}{1+\nu_{*i}^2\varepsilon^3}\left(\frac{1.17-0.35\nu_{*i}^{1/2}}{1+0.7\nu_{*i}^{1/2}} - 2.1\nu_{*i}^2\varepsilon^3\right) \tag{7}$$

For the normalization, Bohm time $t_B = a^2/\chi_B, \chi_B = cT_e/eB$ and the minor radius a are used[5].

3. Analytical solutions of neoclassical flow

For simplicity, we assume the cylindrical geometry without turbulence to obtain the steady state solution. The equations are given by

$$\frac{\partial}{\partial t}\frac{1}{r}\frac{\partial}{\partial r}r\frac{\partial}{\partial r}\left(\Phi + T\right) = -\frac{1}{\rho_*}\frac{q}{\varepsilon}\mu_1\frac{1}{r}\frac{\partial}{\partial r}r\left(V + \rho_*\frac{q}{\varepsilon}\frac{\partial}{\partial r}\left(\Phi + (1-\kappa_{nc})T\right)\right) \tag{8}$$

$$\frac{\partial V}{\partial t} = -\mu_1\left(V + \rho_*\frac{q}{\varepsilon}\frac{\partial}{\partial r}\left(\Phi + (1-\kappa_{nc})T\right)\right) \tag{9}$$

$$\frac{\partial T}{\partial t} = \chi\frac{1}{r}\frac{\partial}{\partial r}r\frac{\partial T}{\partial r} + S_T \tag{10}$$

where $S_T = \hat{\chi}T_0 J_0(j_{0,1}r), \quad \hat{\chi} = j_{0,1}^2\chi, \quad j_{0,1}$ is the solution of $J_0(j_{0,1}) = 0$. The analytical solutions are written as

$$\Phi(r,t) = J_0(j_{0,1}r)\left(c_1 + c_2 e^{-(\mu_1+\mu_{nc})t} + \left(1 + \frac{\mu_{nc}\kappa_{nc}}{\hat{\chi}-\mu_1-\mu_{nc}}\right)T_0 e^{-\hat{\chi}t}\right) \tag{11}$$

$$V(r,t) = J_1(j_{0,1}r)\rho_*\frac{q}{\varepsilon}j_{0,1}\left(c_1 + T_0(1-\kappa_{nc}) - \frac{\varepsilon^2}{q^2}c_2 e^{-(\mu_1+\mu_{nc})t} - \frac{\mu_1\kappa_{nc}T_0}{\hat{\chi}-\mu_1-\mu_{nc}}e^{-\hat{\chi}t}\right) \tag{12}$$

$$T(r,t) = T_0 J_0(j_{0,1}r)\left(1 - e^{-\hat{\chi}t}\right) \tag{13}$$

where $\mu_{nc} = q^2/\varepsilon^2\,\mu_1$. Imposing initial conditions: $\Phi(r,0) = V(r,0) = 0$, the steady state solution of the electric field is given by

$$E_r(r,\infty) = -\frac{\partial}{\partial r}\Phi(r,\infty) = j_{0,1}J_1(j_{0,1}r)T_0\left(-1 + \frac{\kappa_{nc}}{1+\varepsilon^2/q^2}\right) \tag{14}$$

where $\kappa_{nc} = 1.17(banana), -0.5(plateau), -2.1(collisional)$. The electric field will change the sign from positive to negative according to banana-plateau transition.

4. Simulation results

In nonlinear simulation by GF-ITG, we choose the source $S_T = 8\chi(1-2r^2)$, and initial value $T_{0,0}(r,t=0) = 0.5((1-r^2)^2 + T_1)$, $T_1 = 10^{-3}$. Figure 1 shows q profile. The minimum point is located at $r = 0.5$. Figure 2 shows the time evolution of fluctuating internal energy. The dominant Fourier modes are shown. It is seen that the energy of (0,0) and (1,0) modes decrease. Figure 3 shows time evolution of mean ion temperature profile.

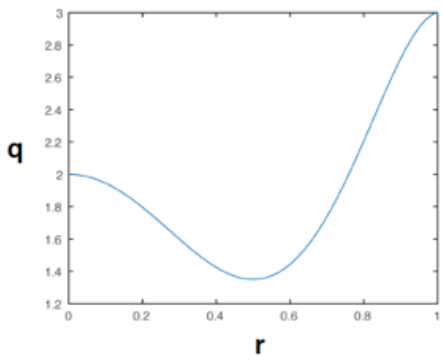

Fig.1 q profile

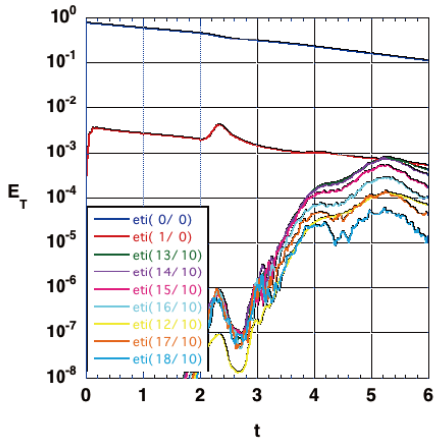

Fig.2 Time evolution of internal energy

The mean ion temperature decreases and the steady state is not obtained in this simulation.

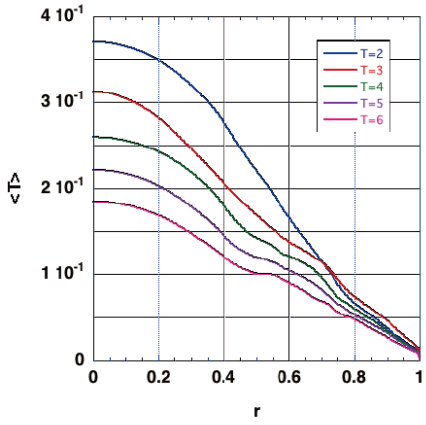

Fig.3 Time evolution of mean ion temperature profile

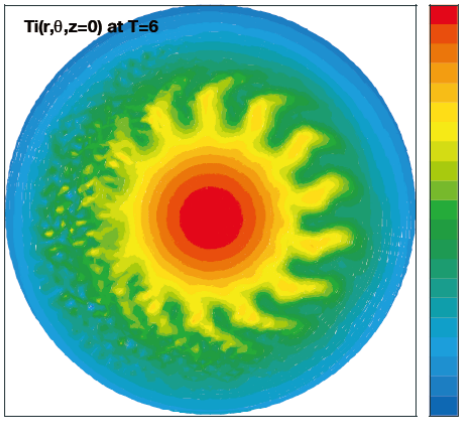

Fig.4 Contour plot of $T(r,\vartheta,z=0)$ at T=6.

Figure 4 shows the contour plot of $T(r,\vartheta,z=0)$ at $T=6$. Outside of q minimum point, the large structure develops. The heating source is used to maintain the large structure. More simulation study is necessary to understand flow effect on ITB formation.

5. Discussion

In the previous study, we have compared flux driven simulation and fixed gradient simulation without neoclassical flows. In these cases, we have observed ITG growth and saturation for

both cases. In the present case, flux driven simulation gives no ITG growth instead low n mode growth and saturation. We will perform fixed gradient simulation with neoclassical flows and investigate evolution of each mode. If we have saturation of ITG turbulence for this case, then we will apply the perturbative source and observe the plasma response. It will help us to understand the effect of neoclassical flows on ITB formation. It is left for a future work.

Acknowledgments

The author would like to thank Drs. N. Miyato, A. Matsuyama and T. Takizuka for useful comments. The computation was carried out using the HELIOS supercomputer system at IFERC-CSC.

References

[1] M. Barnes et al., Physics of Plasmas **17** 056109(2010).

[2] P. J. Knight et al., Computer Physics Communications **183**, 2346(2012).

[3] M. Honda and M. Nakata, 32th JSPF annual meeting, Nagoya, 24aE06P(2015).

[4] H. Seto, M. Yagi and X.Q. Xu, 15th International Workshop on Plasma Edge Theory in Fusion Devices, Nara, Japan, P1-10(2015).

[5] S. Tokunaga et al., Nucl. Fusion 49 075023(2009).

[6] J. D. Callen et al., Plasma Physics and Controlled Nuclear Fusion Research **(**International Atomic Energy Agency, Vienna, 1987**)**, Vol. I, p. 157; μ_1 is given here.

[7] F. L. Hinton and R. D. Hazeltine, Rev. Mod. Phys. 48 239(1976); κ_{nc} is given by eq.(6.136).

Integrated modeling of impurity transport in core and SOL/divertor plasmas

N. Hayashi, K. Shimizu, K. Hoshino, M. Honda
Japan Atomic Energy Agency

Impurity seeding plays a key role to reduce the heat load on divertor plates in tokamak plasmas. However, the accumulation of seeded impurity in the core may reduce the core confinement by enhancing the radiation and dilution. In order to study the transport of impurity in SOL/divertor and core regions and its self-consistent effect on the divertor heat load and the core energy confinement, the integrated modeling code for core and SOL/divertor plasmas including impurity is one of the effective methods. For this integrated modeling, it is necessary to couple a core impurity transport code with a SOL/divertor impurity transport code. In this paper, we have developed a model to couple 1-dimensional (1D) fluid code for core impurities with 2D Monte-Carlo (MC) code for SOL/divertor impurities.

We have been developing an integrated modeling code TOPICS (formerly called TOPICS-IB [1]), in which a 1.5D core transport solver is coupled with a 2D divertor code SONIC [2]. The 1.5D core transport solver in TOPICS, however, treats only fully striped ions and can not treat many charge states of impurity and resultant radiations. To treat core impurity physics in TOPICS, we developed a 1D core impurity transport code IMPACT, which calculates ionization/recombination processes, radiations, radial diffusive/convective transports of multi impurity species, and couple IMPACT with TOPICS. One of the features of SONIC is the MC approach in an impurity-part code IMPMC, which has a lot of flexibility in impurity modeling such as interactions with walls and kinetic effects. However, the IMPMC run including the core region takes much calculation time and thus requires coupling with IMPACT. At the interface boundary of IMPMC, only inward diffusive flow is obtained because MC codes need a region beyond the interface to evaluate the net flow. Outflow is a direct boundary condition for MC codes. On the other hand, the fluid code IMPACT uses the net flow and thus can not use directory the inward diffusive flow of IMPMC as a boundary condition. Therefore, we develop a interface model to couple the codes as shown in Fig.1. When the diffusive transport is considered, low charge state Z impurities in a low temperature T region go to high-T region and high-Z impurities in a high-T region go to the low-T region, vice versa. Thus, the dependence of radial impurity particle flux on Z is expected in the upper figure of Fig.1. A procedure to couple is as follows; (1) Evaluate impurity densities of each charge state near the boundary in IMPMC, Set them to boundary densities in IMPACT and Run IMPACT and Evaluate a net flow F, (2) Evaluate inflow F_- in IMPMC, (3) Evaluate outflow F_+ from a relation of $F = F_+ -$

F_-, Give it to IMPMC and Run IMPMC. The above procedure is iterated to obtain a stationary state solution, or used in the time evolution. To verify the applicability of this model, we calculate a simple case where Ar is used as an impurity and only the constant anomalous diffusivity is assumed. Figure 2 shows the dependence of radial particle flux on the charge state at the boundary of ρ=0.97 obtained from IMPACT. The Z dependence almost agrees with the expectation in Fig.1, but distorts largely. The peak at Z=16 due to its largest accumulation in the core edge region.

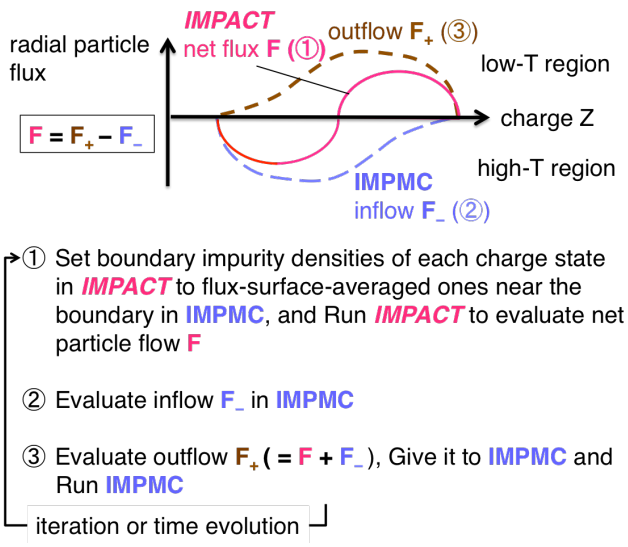

Fig.1 Schematic view of dependence of radial impurity particle flux on charge state Z (upper) and model procedure to couple impurity fluid code ***IMPACT*** and impurity MC code **IMPMC** (bottom)

The obtained flux profile as well as profiles of impurity densities almost agree with those obtained from IMPMC including the core region beyond ρ=0.97 without the interface model. As a result, the applicability of interface model is confirmed in the IMPCAT side. Next, we will run IMPMC with test particles generated at the boundary of IMPMC side on the basis of outflow F+ in Fig.2 and confirm the model applicability in the IMPMC side by comparing obtained results with those obtained from IMPMC including the core region without the interface model. Then, we will analyze more complicated cases including the neoclassical transport.

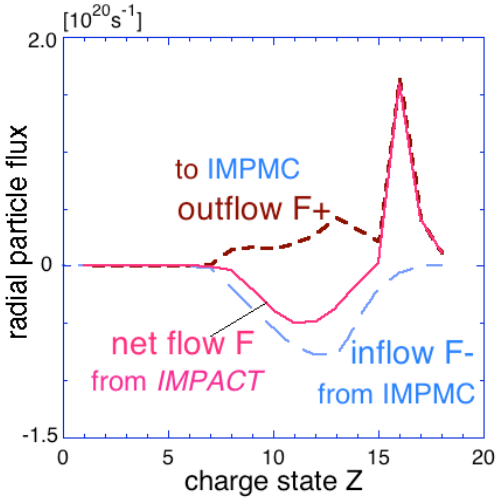

Fig.2 Dependence of radial Ar particle flux on charge state Z at interface of ρ=0.97 in case where only anomalous diffusivity D_{an}=0.3m^2/s is assumed in whole region.

References

[1] N. Hayashi et al Phys. Plasmas **17** (2010) 056112.

[2] M. Yagi et al Contrib. Plasma Phys. **52** (2012) 372.

Integrated heat transport simulation of the helium-hydrogen plasma of LHD by TASK3D

S. Maeta, S. Murakami, H. Yamaguchi, A. Fukuyama, K. Nagaoka[a], H. Takahashi[a], H. Nakano[a], M. Osakabe[a], K. Tanaka[a], M. Yokoyama[a], and LHD Exp Group[a]

Department of Nuclear Engineering, Kyoto University, Kyoto 615-8540, Japan
[a]National Institute for Fusion Science,322-6 Oroshi-cho, Toki 509-5292, Japan

The heat transport of the helium-hydrogen experiment plasma is studied to make clear the ion species dependence on the heat transport. We evaluate the NBI heat deposition of multi-ion plasma by GNET code[1, 2] and study the heat transport by TASK3D. It is found that the turbulent transport improvement is necessary to explain the increase in ion temperature in the high fraction helium plasma. We apply the turbulent transport improvement models and obtain relatively good agreements.

Introduction

Various physical phenomena with wide ranges of time and space scales are connected in the fusion plasma. Thus, in order to predict the performance of the fusion plasma, an integrated simulation combining various physics models is required. Many integrated simulation code has been developed for tokamak and helical plasmas. TASK3D is an integrated simulation code for helical plasma and has been applied to the analyses of the plasma transport of LHD plasmas[3, 4].

On the other hand, the deuterium experiment project from 2017 is planned in LHD, where the deuterium NBI heating beams with the power more than 30MW are injected to the deuterium plasma. Main objects of this project are to make clear the isotope effect on the heat and particle transport in the helical plasma, and to study energetic particle confinement in a helical magnetic configuration measuring triton burn-up neutrons.

In the 2014 campaign of LHD we have performed the helium-hydrogen plasma experiment to make clear the ion species dependence on the heat transport, which would be related to the isotope effect on the plasma confinement. We have found that the central ion temperature goes up as the helium fraction increases in the helium-hydrogen plasma.

In this paper we study the heat transport of the helium-hydrogen experiment plasma to make clear the ion species dependence on the heat transport.

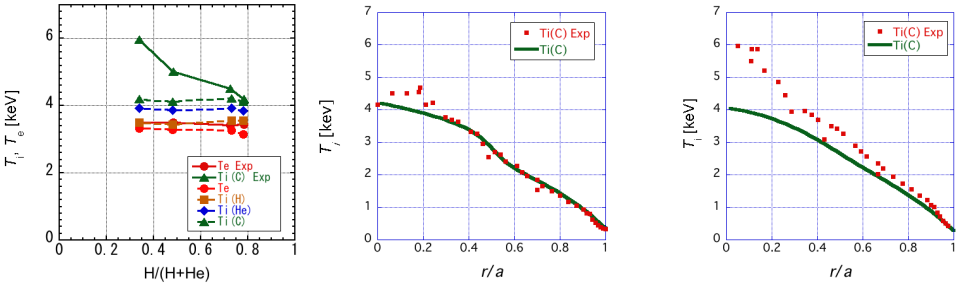

(a) (b) H/(H+He)=0.73 (c) H/(H+He)=0.34

Figure 1: Comparisons of the ion and electron temperatures of the simulation and experiment results. (a) the helium density rate dependency, (b) the low helium density rate case, and (c) the high helium density rate case. Solid lines and dots show the experiment and simulation results, respectively.

Heat transport simulation of hydrogen-helium plasma

We evaluate the NBI heat deposition of multi-ion plasma by GNET code[1, 2] and study the heat transport by TASK3D.

In the previous studies we found that the turbulent transport models for electron, the gyro-Bohm χ_e^{TB}, and for ion, the gyro-Bohm(gradT) χ_i^{TB}, show relatively good agreements with the experimental results of the hydrogen experiment plasma[4]. We, first, apply these turbulent transport model to the helium-hydrogen plasma. Figure 1 shows the heat transport simulation results based on the turbulent transport model for hydrogen plasma. We can see that the ion temperature does not agree with the experimental results as the helium density rate is increased. Thus, we considered three other turbulent transport models; the conventional model, the Z_{eff}depending model and the strongly A_{eff} depending model.

To reproduce the experiment results of the ion temperature, a conventional transport improvement model is assumed as $\chi_i^{TB} = \overline{\chi_i^{TB}} \times A_{eff}^{-\alpha}$, where the effective mass number is given by $A_{eff} = \sum_i n_i A_i / n_e$. Figure 2 shows that the of the ion temperatures of the simulation and experiment results assuming the conventional improvement model with $\alpha = 0.5$ and 10. It is found that the conventional model can not fit the strong helium density rate dependency observed in the experiment plasma.

Next, we assume the turbulent transport improvement model depending on the Z_{eff}, which is introduce to explain the transport improvement in the high Ti plasma with the carbon pellet injection[5]. Figure 3 shows the comparisons of the simulation and experimental results assuming the Z_{eff} dependent turbulent improvement model. We can see a slight different tendency with the experiment results.

Finally, we assume a new model strongly depending on the effective mass number

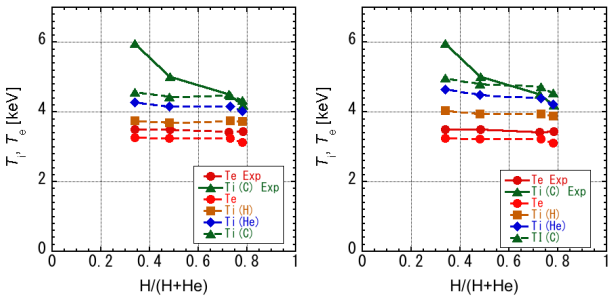

(a) $\alpha = 0.5$ (b) $\alpha = 1.0$

Figure 2: Comparisons of the ion temperatures of the simulation and experiment results assuming the conventional improvement model with $\alpha = 0.5$ and 10.

$\chi_i^{TB} = \overline{\chi_i^{TB}} \times \exp(-kF(A_{eff} - c))$. We determined constant numbers $c = 1.4$ and $k = 2.0$ to minimize the difference between the temperatures of experiments and using least squares method. Figure 4 shows the comparisons of the simulation and experimental results assuming the strongly A_{eff} depending model. We obtain good agreements in the H/He dependences and in radial profiles of T_c.

Conclusions

We have developed the integrated simulation code TASK3D to predict the plasma performance in the 3D magnetic configuration plasma. We have studied the heat transport of H/He plasma by TASK3D comparing with the experimental results of LHD to clarify the ion temperature increase and the isotope effect. Three turbulent transport models are assumed; the conventional model, the Z_{eff}depending model and the strongly A_{eff} depending model. A relatively good agreement is obtained with the strongly A_{eff} depending model (c=1.4 and k=2.0) and Z_{eff} model.

References

[1] H. Yamaguchi and S. Murakami, Plasma Fusion Res. **9** (2014) 3403127.

[2] S. Murakami, et al., Nuclear Fusion **46** (2006) S425.

[3] S. Murakami, et al., Plasma Phys. Control. Fusion **57** (2015) 054009.

[4] A. Sakai, et al., Plasma Fusion Res. **9** (2014) 3403124.

[5] S. Murakami, et al., Proc. IAEA Fusion Energy Conf. 2014, Russia (2014) TH/P6-38.

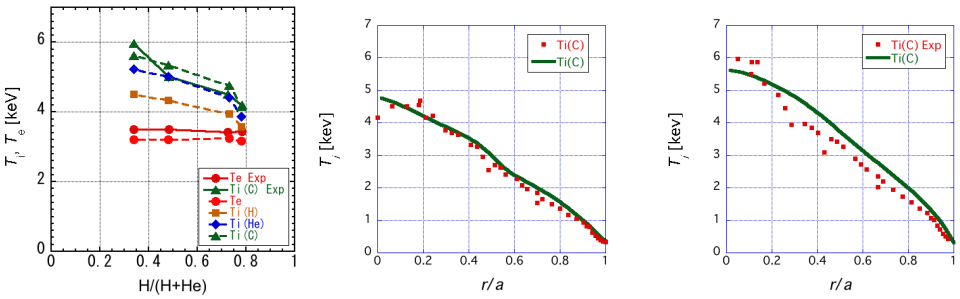

(a) (b) H/(H+He)=0.73 (c) H/(H+He)=0.34

Figure 3: Comparisons of the ion and electron temperatures of the simulation and experiment results assuming the Z_{eff} dependent improvement model, (a) the helium density rate dependency, (b) the low helium density rate case, and (c) the high helium density rate case.

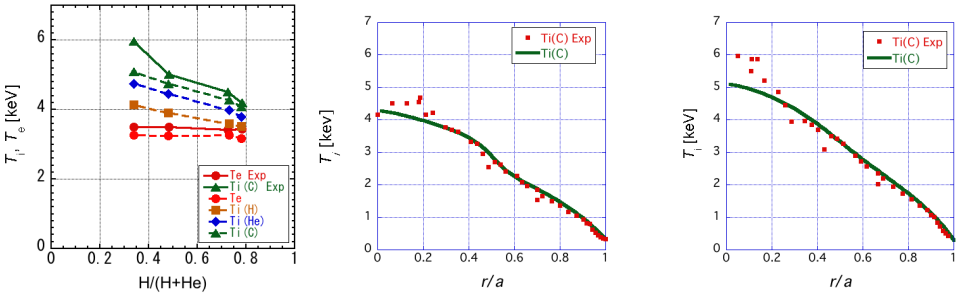

(a) (b) H/(H+He)=0.73 (c) H/(H+He)=0.34

Figure 4: Comparisons of the ion and electron temperatures of the simulation and experiment results assuming the strongly A_{eff} depending model, (a) the helium density rate dependency, (b) the low helium density rate case, and (c) the high helium density rate case.

Integrated Simulation of Deuterium Experiment Plasma in LHD

S. Murakami, H. Yamaguchi, M. Homma, S. Maeta, A. Sakai, A. Fukuyama, K. Nagaoka*, H. Takahashi*, H. Nakano*, M. Osakabe*, M. Yokoyama*, K. Tanaka*, K. Ida*, M. Yoshinuma*, M. Isobe*, H. Tomita**, K. Ogawa* and LHD Exp Group*

Department of Nuclear Engineering, Kyoto Univ., Nishikyo, Kyoto 615-8540, Japan
**National Institute for Fusion Science, 322-6 Oroshi, Toki 509-5292, Japan*
***Department of Quantum Engineering, Nagoya Univ., Nagoya, Japan*
e-mail: murakami@nucleng.kyoto-u.ac.jp

The deuterium experiment plasma of LHD is investigated by applying the integrated simulation code TASK3D and the 5-D drift kinetic equation solver GNET. (i) More than 20% of ion temperature increment is obtained in the deuterium plasma ($n_D/n_H + n_D = 0.8$) due to the isotope effect assuming the turbulent transport model based on the H/He plasma experiment of LHD. (ii) The triton burn-up simulation shows the triton slowing down distribution and more than 7.0×10^{11} $\mathrm{m^{-3}s^{-1}}$ of 14MeV neutron production by the D-T fusion reaction at the plasma center.

Introduction

The deuterium experiment project from 2017 is planned in LHD, where the deuterium NBI heating beams with the power more than 30MW are injected into the deuterium plasma. Principal objects of this project are to clarify the isotope effect on the heat and particle transport in the helical plasma and to study energetic particle confinement in a helical magnetic configuration measuring triton burn-up neutrons.

We have developed an integrated transport simulation code, TASK3D[1], and applied to the high ion temperature plasma of LHD[2]. We obtain relatively good agreements between the simulated and experimental radial profiles of the density and temperature in the steady state hydrogen plasmas. Also, to study the kinetic behavior of the energetic particle in helical plasmas, we have developed the GNET[3] code, in which the drift kinetic equation of energetic particles is solved in five-dimensional phase space. In this paper, we predict the plasma performance of the deuterium experiment plasma in LHD by applying the TASK3D and GNET codes.

Prediction of high-Ti deuterium experiment plasma

We perform the integrated heat transport simulation of deuterium plasma by TASK3D code. A typical density profiles are assumed as $n_s(r/a) = n_{s0}\{1 - (r/a)^8\}$ where n_s is the s-species density profile satisfying the charge neutrality $n_e = \sum_i n_i$. We assume two central density cases; $n_{e0} = 2.0$ and 3.0×10^{19} $\mathrm{m^{-3}}$, and the deuterium-hydrogen density ratio as $n_D/n_D + n_H = 0.8$.

We evaluate the heat deposition profiles for the multi-ion species plasma (e, H, He, C) by using GNET code. Three tangential NBI heating (#1-3) with the beam energy $E_b = 180$keV and the heating power $P_{tNBI} = 14$MW, and two perpendicular NBI heating (#4 and 5) with $E_b = 60-80$keV and $P_{pNBI} = 18$MW are injected to the deuterium plasma of LHD. Figure 1-(left) shows the heat deposition profiles of the electron, deuterium and hydrogen ions. We can see peaked heating profiles of the electron and deuterium ion heating.

One-dimensional (1-D) diffusive heat transport equation with multi-ion species (H, He, C) is solved using the heat deposition profiles by GNET. We assume that the heat transport consists of the neoclassical and turbulent transport. The neoclassical transport database, DGN/LHD, evaluates the neoclassical heat transport for all species, and the radial electric field is determined by the ambipolar condition of neoclassical electron and ion fluxes.

In our previous studies, we have assumed the gyro-Bohm model for the electron heat conduction and the gyro-Bohm grad-T_i model for the ion one[4] as the turbulent transport model for the hydrogen plasma. However, it is necessary to consider the isotope effect in the deuterium plasma case. To solve this problem we have performed the H/He experiment in the 2014 campaign of LHD. We have varied the H-He ratio, $\xi_H = n_H/n_H + n_{He}$, keeping the electron density profile. It is found that the ion temperature increases as ξ_H decreases while the electron temperature shows almost no change. To take into account this ion temperature increment we assume a turbulent transport model, in which we multiply an improvement factor depending on the effective mass number$A_{eff} = \sum_i (M_i/Z_i)$ to the gyro-Bohm grad-T_i model.

Figure 1-(right) shows the deuterium ion temperatures in the deuterium experiment plasma of LHD with and without the isotope effect on the turbulent transport by the A_{eff} depending model. It is found that the deuterium ion temperature reaches more than 6 keV with the isotope effect in the deuterium experiment plasma. On the other hand, the ion temperature reaches about 5 keV if we assume a pure hydrogen plasma. This result indicates that we will obtain about 20% higher ion temperature than that of the hydrogen plasma in the deuterium experiment of LHD if we assume an isotope effect on the turbulent transport based on the He/H experiment results.

Triton burn-up simulation

We perform the triton burn-up simulation of the deuterium experiment of LHD and evaluate the D-T fusion reaction rates to compare with the experimental results of the 14 MeV neutron diagnostic system. The radial profile of the 1 MeV triton production rate due to the D-D fusion reaction between D-beam and D-thermal ions is evaluated by GNET using the radial profiles of T_D and n_D obtained by TASK3D. As a result we obtain a center peaked triton production rate about 1.4×10^{14} m^{-3}s^{-1} in the $n_{e0} = 2.0 \times 10^{19}$ m^{-3} case.

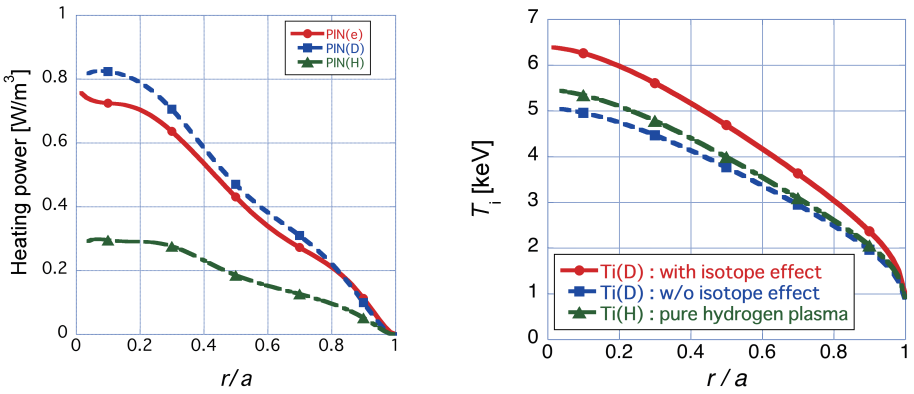

Figure 1: *Radial profiles of the NBI heat depositions (left) and ion temperatures (right) in the deuterium experiment plasma with* $n_{e0} = 2.0 \times 10^{19}$ m^{-3} *and* $n_D/n_H + n_D = 0.8$.

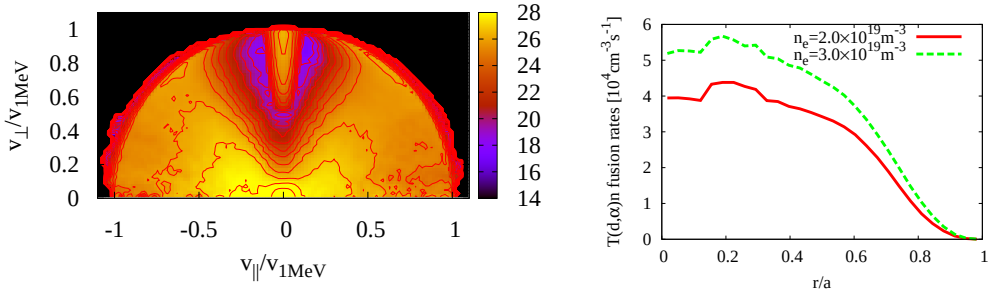

Figure 2: *Slowing down distribution of 1MeV tritons in the velocity space (left) and radial profiles of 14MeV neutron production rate by the D-T fusion reaction[$P_{tNBI} = 1MW$] (right).*

Next we solve the 5-D drift kinetic equation for the 1MeV tritons by GNET and evaluate the slow down distribution in the real and velocity space. Figure 2-(left) shows the slowing down velocity space distribution of the 1MeV tritons in LHD. We can see a large loss region near the helically trapped particles. About 25% of tritons escape with almost the initial energy of 1 MeV by the prompt orbit loss due to drift motion immediately after their birth ($t < 10^{-5}$ s). After the prompt orbit loss, the collisionless diffusive loss ($10^{-5} < t < 10^{-2}$) and, then, the collisional diffusive loss ($t > 10^{-2}$ s) become dominant. We evaluate the radial profile of 14MeV neutron production rate using the triton distribution by GNET and T_D, n_D profiles by TASK3D [Fig. 2-(right)]. It is found that more than 7.0×10^{11} $\mathrm{m^{-3}s^{-1}}$ of 14MeV neutrons are generated by the D-T fusion reaction at the plasma center.

[1] M. Sato et al., Plasma Fusion Res. **3**, S1063 (2008).

[2] S. Murakami et al., Plasma Phys. Control. Fusion **57**, 054009 (2015).

[3] S. Murakami et al., Nuclear Fusion **46**, S425 (2006).

[4] Wakasa, A. et al., Proc. 39th EPS Conf. and 16th Int. Cong. Plasma Phys., 2012, **P2.028**.

Particle simulation of plasma production by electron cyclotron waves in Tokamak

Tomohide Ikeda, Atsushi Fukuyama

Graduate School of Engineering, Kyoto university

1 Introuction

Plasma production and start up by electron cyclotron waves in tokamak has been successfully applied to reduce the magnetic flux comsumption and the peak value of toroidal electric field, though the physics mechanism has not been understood well. Various phenomena are coupled with each other - electron accelation at the electron cyclotron resonance, ionization by collisions with neutral particles, current drive by toroidal electric field and electron cyclotron waves, suppresion of particle losses by vertical magnetic field, generation of closed magnetic configuration, and so on. In order to analyze these pheomena self-consistently, we are developing a particle simulational module, TASK/PIC. In this report, we show the status of the two-dimentions electromagnetic particle simulation code and the results on the excitation and propagation of the electron cyclotron waves.

2 Numerical model

The governing equations in TASK/PIC are the equation of motion for electron and ion (1), Gauss's law for the scalar potential ϕ (2), time evolution of the vector potential $\boldsymbol{A}$ (3) and equations for the electric field $\boldsymbol{E}$ and the magnetic field $\boldsymbol{B}$ (4):

$$m\frac{\mathrm{d}\boldsymbol{v}}{\mathrm{d}t} = q(\boldsymbol{E} + \boldsymbol{v} \times \boldsymbol{B}), \tag{1}$$

$$-\nabla^2\phi = \frac{\rho}{\epsilon_0}, \tag{2}$$

$$\nabla^2\boldsymbol{A} + \mu_0\boldsymbol{j} - \mu_0\epsilon_0\frac{\partial\nabla\phi}{\partial t} - \mu_0\epsilon_0\frac{\partial^2\boldsymbol{A}}{\partial t^2} = 0, \tag{3}$$

$$\boldsymbol{E} = -\nabla\phi - \frac{\partial\boldsymbol{A}}{\partial t}, \qquad \boldsymbol{B} = \nabla \times \boldsymbol{A}. \tag{4}$$

We normalize the physical quantities by the electron plasma frequency ω_{pe} for the average electron density n_0, $\omega_{pe}^2 = n_0e^2/m_e\epsilon_0$, and the grid spacing Δ of the order of the Debye length.

In our alogrithm, $\bar{\boldsymbol{v}}$ and $\bar{\boldsymbol{A}}$ are defined at the integer mesh in time, while $\bar{\boldsymbol{x}}$, $\bar{\phi}$, $\bar{\boldsymbol{E}}$ and $\bar{\boldsymbol{B}}$ are at the half-integer mesh in time. We assume uniformity in the z direction and solve eq.(2) by FFT or finite difference method. For the particle shape, we use the spline function of the second order. The spline function of the first order is used for the half-integer grid, and the spline function of the second order in the integer grid. We consider a rectangle space in the x-y plane, and employ the boundary condition in periodic or of the conducting wall.

3 Simulation result

The initial particle distribution is uniform in space, and the velocity distribution are Maxwellian. Simulation parameters are as follows: total number of particles for each species (electron, ion): 160000, number of grids: 100×100, $\beta \equiv \omega_{pe}\Delta/c = 0.1$, the time interval $\Delta t = 0.02$. Further, the externally applied fields are as follows: the static magnetic field with linear gradient $\bar{B}_{y0} = \bar{B}_{ymin} + (B_{ymax} - B_{ymin}) \cdot x/100$ and the wave guide elctric field at $x = 0$ and $25 < y < 75$, $\bar{A}_{ywg}(\bar{A}_{zwg}) = \bar{A}_{wg} \sin \bar{\omega}\bar{t}$ which correspond to $\bar{E}_{ywg}(\bar{E}_{zwg}) = -\partial \bar{A}_{ywg}(\bar{A}_{zwg})/\partial \bar{t} = -\bar{\omega}\bar{A}_{wg} \cos \bar{\omega}\bar{t}$.

First, we show the time evolution of total energy with periodic boundary condition up to $\bar{t} = 1000$ in Fig.1. When $B_{y0} = 0$, the potential energy PE_{tot} increase and the kinetic energy KE_{tot} decrease up to around $\bar{t} = 200$. After that they almost saturated, but the total energy E_{tot} gradually increase from the begining. When uniform magnetic field B = 6, PE_{tot}, KE_{tot} and E_{tot} gradually increase all along. We have to resolve this problem.

Next, we excite the electromagnetic waves with $\bar{A}_{ywg} = \bar{A}_{wg} \sin \bar{\omega}\bar{t}$ (O-mode) or $\bar{A}_{zwg} = \bar{A}_{wg} \sin \bar{\omega}\bar{t}$ (X-mode) with $\bar{A}_{wg} = 1$ and $\bar{B} = 6$. In Fig.2, in the case of X-mode, absorption of the elctromagnetic wave occurs near the electron cyclotron resonance $\bar{\omega} = \bar{B} = 6$. As is theoretically predicted for the ordinary-mode, the absorption does not occur. It is because finite Larmor radius effect is small with the present parameters. If we make Δ smaller than cyclotron radius v_{te}/ω_{ce}, the absorption will be confirmed.

Fig.1(a): $\bar{B} = 0$

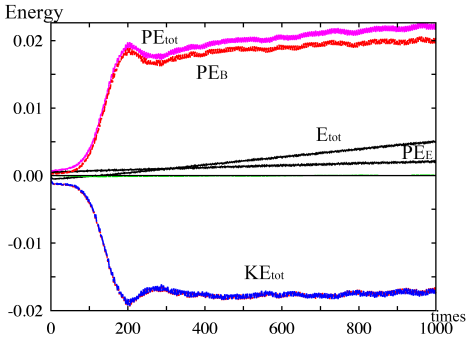

Fig.1(b): $\bar{B} = 6$

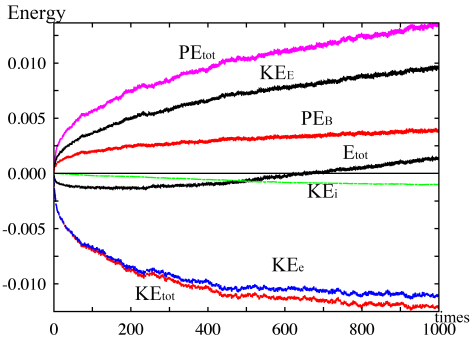

Fig.1: Time evolution of total energy with periodic boundary condition

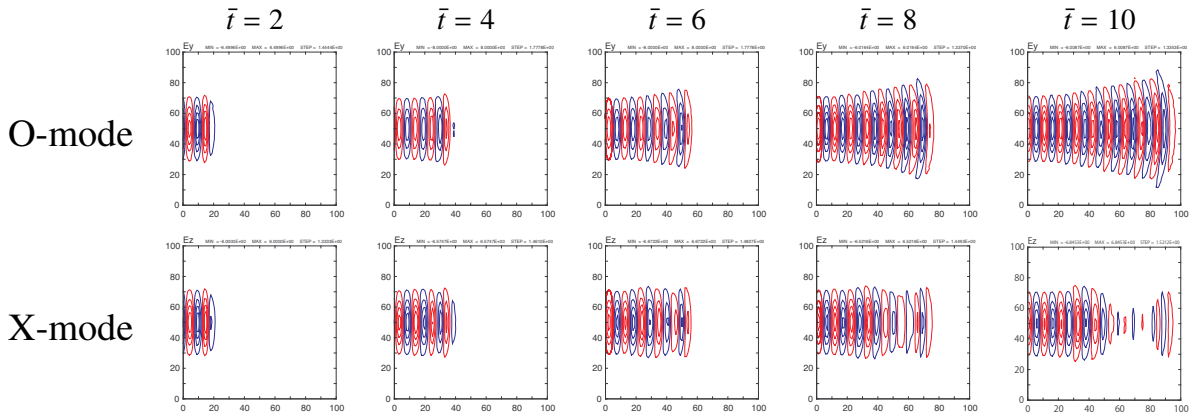

Fig.2: Wave propagation with $\bar{\omega} = 6$ and $\bar{B} = 4 \sim 8$

Finally, we show the time evolution of electron temperature profile in Fig.3. $T_{\parallel}$ is the parallel components of the electron temperature, $T_{\perp}$ is the perpendicular component of the electron temperature and T_e is the electron temperature $T_e = (T_{\parallel} + 2T_{\perp})/3$. In the case of X-mode excitation, $T_{\perp}$ around $x = 40 \sim 50$ increases up to about 7 times the initial temperature.

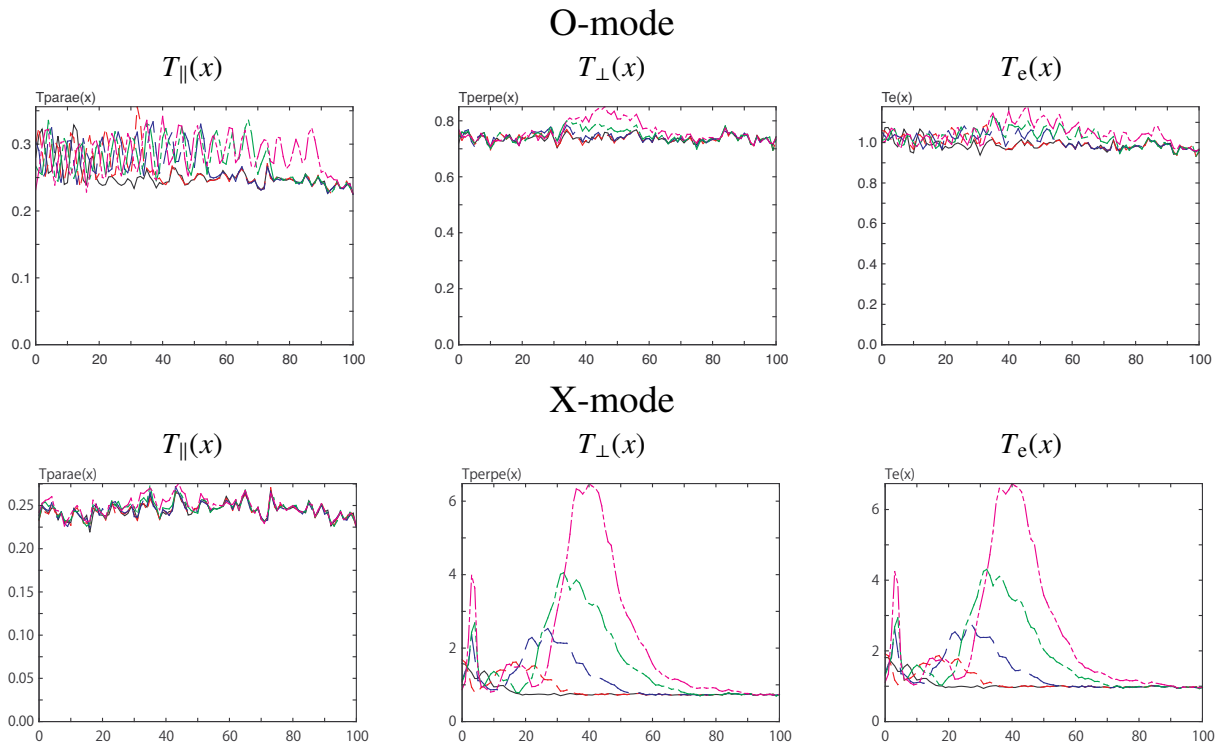

Fig.3: Time evolution of electron temperature profile

4 Summary and Outlook

We have been developing a two-dimentional electromagnetic PIC simulation code TASK/PIC, in order to analayze the plasma production near the electron cyclotron resonance. We use the parallel processing by MPI only for particle motion. After discussion on the conservation of total energy, we have shown the propagation of the electromagnetic waves excited by the waveguide model. We have shown the propagation and absorption of ordinaly and extraordinaly waves propagation and confirmed electron heating near the electron cyclotron resonance. Owing to small finite Larmor radius effect, the absorption cannot be confirmed for ordinary mode.

The remaining issues include to improve phisycal models, such as relativistic effect, absorbing boundary condition, plasma production by ionization, to enhance computional performance, full-scale parallelization, introdution of region splitting, and the use of OpenMP, and to extend to toroidal configuration.

Linear kinetic analysis of Alfvén eigemodes in tokamak plasmas

トカマクプラズマにおけるアルヴェン固有モードの運動論的線形安定性解析

Taisei Futakuchi, Atsushi Fukuyama
二口泰成，福山　淳

Graduate School of Engineering, Kyoto University
Kyoto-Daigaku-Katsura, Nishikyo-ku, Kyoto 615-8540, Japan
京都大学大学院工学研究科 615-8540 京都市西京区京都大学桂

The excitation of Alfvén eigenmodes driven by fast ions is studied in tokamak plasmas using the full wave code TASK/WM. The dielectric tensor for species with anisotropic velocity distribution function is numerically calculated and complex eigenmode frequency is obtained.

1 Introduction

In tokamak plasmas, Alfvén eigenmodes are excited by fast ions generated as a result of fusion reaction, ICRF heating or NBI heating. Resonant interaction between fast ions and the destabilized Alfvén eigenmodes (AEs) may cause rapid transport of fast ions, which leads to a loss of fast ions, decreasing heating efficiency and damaging plasma facing components. Therefore stability analysis of Alfvén eigenmodes is important and it has been extensively explored theoretically, experimentally and numerically.

There are various AEs which have different frequencies, such as toroidicity-induced Alfvén eigenmode (TAE), beta induced AE (BAE) and so on. Some of them are affected by mode conversion (e.g. kinetic Alfveén eigenmode (KAE)) and lower frequency modes are coupled with other waves (e.g. ion acoustic wave). Therefore careful study of AE using appropriate model which can properly describe the dynamics in the focused scale is required.

We have analyzed the linear stability of AEs by the full wave code TASK/WM. The model used in the analysis and some examples of analyses with the code is presented in this report.

2 Full wave analysis code TASK/WM

In the full wave code TASK/WM, Maxwell's equation for the wave electric field $\mathbf{E}$ with frequency ω

$$\boldsymbol{\nabla}\times\boldsymbol{\nabla}\times\boldsymbol{E}=\frac{\omega^2}{c^2}\overleftrightarrow{\epsilon}\cdot\boldsymbol{E}+\mathrm{i}\,\omega\mu_0\,\boldsymbol{j}_{\mathrm{ext}} \qquad (1)$$

is solved with the kinetic dielectric tensor $\overleftrightarrow{\epsilon}$ for various plasma models. With poloidal and toroidal mode expansion, parallel wave number is correctly taken into account to describe the wave-particle resonant interaction. Eigenmode with complex wave frequency is obtained by maximizing the wave amplitude for given external current proportional to the plasma pressure.

Since the response of plasmas is determined by the dielectric tensor, the model of the dielectric tensor is important. However, the more general the model is, the less tractable.

For simplicity, the model based on the drift kinetic equation system[1] is adopted in the present analyses. This model which consists of the linear current density and the drift kinetic equation can describe the poloidal mode coupling due to the interaction between drift motion of the fast particles and AEs. The induced current density is calculated by integrating perturbed distribution function of fast ions in velocity space

$$\mathbf{j}_p=\int \mathrm{d}\mathbf{v}\, e_\alpha \mathbf{v}_d f_{\alpha 1}=\overleftrightarrow{\sigma}\mathbf{E}=-\mathrm{i}\epsilon_0\omega\overleftrightarrow{\chi}\mathbf{E} \qquad (2)$$

and the induced current is proportional to the wave electric field in a linear analysis. Then, the electric susceptibility tensor $\overleftrightarrow{\chi}$ is calculated by using perturbed distribution function which is described by the drift kinetic equation

$$\left[\frac{\partial}{\partial t}+v_\parallel\nabla_\parallel+(\mathbf{v}_d+\mathbf{v}_E)\cdot\boldsymbol{\nabla}+\frac{e_\alpha}{m_\alpha}(v_\parallel E_\parallel+\mathbf{v}_\mathrm{d}\cdot\mathbf{E})\frac{\partial}{\partial\varepsilon}\right]f_\alpha=0,$$

where $\mathbf{v}_E$ is the $\mathbf{E}\times\mathbf{B}$ drift velocity and $\mathbf{v}_d$ is the magnetic drift velocity. It is necessary to linearize this equation in terms of the perturbed distribution function. Since it is a system of differential equations including the term $\mathbf{v}_d\cdot\nabla f$, it is complicated to solve the equation directly. Even if the radial derivative

term of $\mathbf{v}_d \cdot \nabla f$ is neglected, the drift kinetic equation is infinite dimensional system of equations in Fourier expansion. Considering only several sideband harmonics by truncating terms satisfying $\mathbf{k} \cdot \mathbf{v}_d/\omega \ll 1$, or assuming low drift frequency, the problem becomes tractable. Based on these assumptions, approximate electric susceptibility tensor $\overleftrightarrow{\chi}$ is calculated in Fourier expansion form as

$$
\begin{aligned}
\overleftrightarrow{\chi}_{mm'} &= \begin{pmatrix} 1 & \mathrm{i} & 0 \\ \mathrm{i} & -1 & 0 \\ 0 & 0 & 0 \end{pmatrix} P_{m-1,m-2}\delta_{m',m-2} \\
&+ \begin{pmatrix} 0 & 0 & \mathrm{i}\,Q_{m-1,m-1} \\ 0 & 0 & -Q_{m-1,m-1} \\ \mathrm{i}\,Q_{m,m-1} & -Q_{m,m-1} & 0 \end{pmatrix} \delta_{m',m-1} \\
&+ \begin{pmatrix} -(P_{m-1,m}+P_{m+1,m}) & \mathrm{i}\,(P_{m-1,m}-P_{m+1,m}) & 0 \\ -\mathrm{i}\,(P_{m-1,m}-P_{m+1,m}) & -(P_{m-1,m}+P_{m+1,m}) & 0 \\ 0 & 0 & -R_{m,m} \end{pmatrix} \delta_{m',m} \\
&+ \begin{pmatrix} 0 & 0 & -\mathrm{i}\,Q_{m+1,m+1} \\ 0 & 0 & -Q_{m+1,m+1} \\ -\mathrm{i}\,Q_{m,m+1} & -Q_{m,m+1} & 0 \end{pmatrix} \delta_{m',m+1} \\
&+ \begin{pmatrix} 1 & -\mathrm{i} & 0 \\ -\mathrm{i} & -1 & 0 \\ 0 & 0 & 0 \end{pmatrix} P_{m+1,m+2}\delta_{m',m+2}
\end{aligned}
$$

$$
\begin{aligned}
P_{m,m^*} &= \frac{a}{4}\int \mathrm{d}\mathbf{v}\,\frac{1}{1-k_{\parallel m}v_\parallel/\omega}\,{v_d}^2 c_{m^*} f_{\alpha 0} \qquad (3)\\
Q_{m,m^*} &= \frac{a}{2}\int \mathrm{d}\mathbf{v}\,\frac{1}{1-k_{\parallel m}v_\parallel/\omega}\,v_d v_\parallel c_{m^*} f_{\alpha 0} \qquad (4)\\
R_m &= a\int \mathrm{d}\mathbf{v}\,\frac{1}{1-k_{\parallel m}v_\parallel/\omega}\,{v_\parallel}^2 c_m f_{\alpha 0} \qquad (5)\\
a &= \frac{e_\alpha^2}{\omega^2\epsilon_0 T_\alpha},\\
c_m &= \hat{T} - \frac{\omega_{*m}}{\omega} = -T_\alpha\frac{\partial \ln f_{\alpha 0}}{\partial \varepsilon} - \frac{\mathrm{i}T_\alpha}{r\omega e_\alpha B}\frac{\partial \ln f_{\alpha 0}}{\partial r}\frac{\partial}{\partial \theta}
\end{aligned}
$$

In the case of steady state (Maxwellian distribution), Eq.(3) to (5) are easily calculated with plasma dispersion relation. In the case that fast ion has anisotropic distribution function or localized density profile, it is necessary to integrate numerically in complex velocity space.

In order to consider kinetic effects such as finite Larmor radius (FLR) effects and coupling of Alfvén waves with low frequency waves, the model based on the gyrokinetic equation is required[2],[3].

3 Simulation results

Fig.1 and Fig.2 are examples of analyses by TASK/WM describing excitation by fast ions in the case of Maxwellian distribution function. These figures are contour of $|E|^2$ in complex frequency space and we can find eigenmode frequencies from them.

The mode whose frequency is around 80kHz is toroidaicity-induced Alfvén eigenmode (TAE) and its growth rate has good agreement (Fig.3) with the one calculated by approximate formula by G. Y. Fu [4]

$$
\frac{\gamma}{\omega_{TAE}} \simeq \frac{9}{4}\left[\beta_\alpha\left(\frac{\omega_{*\alpha m}}{\omega_{TAE}} - \frac{1}{2}\right)F\left(\frac{v_A}{v_{T_\alpha}}\right) - \beta_e\frac{v_A}{v_e}\right]. \qquad (6)
$$

In addition, it is shown that lower frequency modes are more strongly excited by the increase of fast ion temperature and the mode frequency having the highest growth rate gets close to TAE frequency. This mode is considered as a kind of energetic particle mode (EPM).

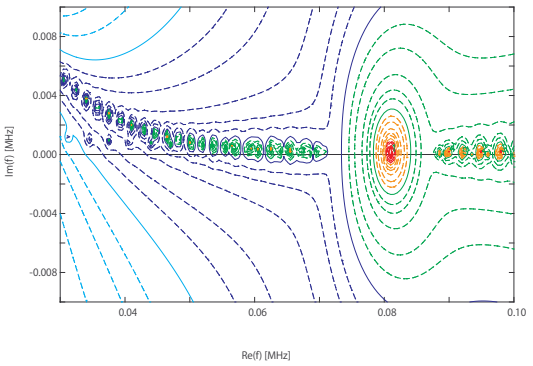

Fig. 1 Contour of the wave amplitude in a complex frequency plane with fast ion components 0.2%, T= 100keV

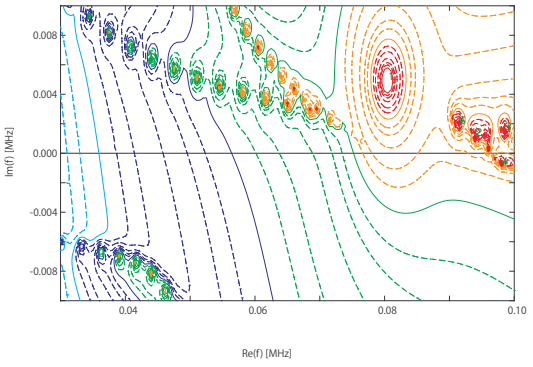

Fig. 2 Contour of the wave amplitude in a complex frequency plane with fast ion components 0.2%, T= 500keV

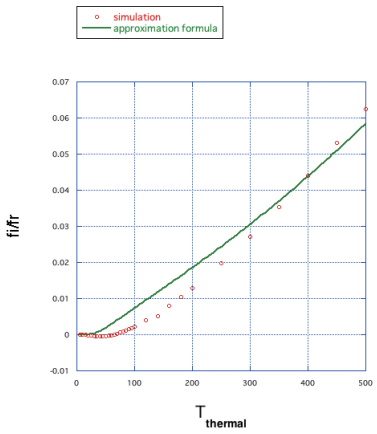

Fig. 3 Comparison of the fast ion temperature dependence of the growth rate between the numerical results and these of the approximate fomula.

4 Future work

We are now developing a code to analyze AEs excited by fast ions which have arbitrary velocity distribution function. Then, it is possible to carry out self-consistent analysis of AEs including the modification of velocity distribution function calculated by the Fokker-Plank code.

REFERENCES

[1] Y.M. Li, S.M. Mahajan and D.W. Ross, Phys. Fluids **30**, 1466 (1987)

[2] L. Chen and F. Zonca, Nucl. Fusion **47**, S727 (2007)

[3] L. Chen and F. Zonca, EPL **96**, 35001 (2011)

[4] G. Y. Fu and J. W. Van Dam, Phys. Fluids B **1**, 2404 (1989)

Progress in applying gyrokinetic heat diffusivity model to transport simulations for helical plasmas

S. Toda, M. Nunami, A. Ishizawa[1], S. Murakami[2], T. -H. Watanabe[3] and H. Sugama
National Institute for Fusion Science, Oroshi-cho 322-6, Toki, Gifu, 509-5292, Japan
[1]*Graduate School of Energy Science, Kyoto Uni., Gokasho, Uji, Kyoto, 611-0011, Japan*
[2]*Department of Nuclear Engineering, Kyoto Uni., Nishikyo, Kyoto, 615-8540, Japan*
[3]*Department of Physics, Nagoya University, Furo-cho, Nagoya, Aichi, 464-8602, Japan*

Turbulent transport is one of the most critical issues for plasma confinement in magnetic fusion devices. Recently, a large number of the gyrokinetic simulations have been done in toroidal plasmas [1]. The GKV-X code solving the gyro-kinetic equation has been used to examine the ITG mode and zonal flows in the LHD for studying the turbulent transport in helical plasmas [2]. The reduced model of $\chi_i \sim \rho_{ti}^2 v_{ti} f(\mathcal{L}, \tilde{\tau}_{ZF})/R$ is taken [3] using the GKV-X code for the high-T_i LHD discharge. Here, $\mathcal{L}$ is the mixing length estimate $\tilde{\gamma}_{\tilde{k}_y}/\tilde{k}_y^2$ integrated over the $\tilde{k}_y$ space, where $\tilde{\gamma}_{\tilde{k}_y}$ is the normalized linear growth rate of the ITG mode and $\tilde{\tau}_{ZF}$ is the normalized decay time of zonal flows [4, 5]. However, it is costly to carry out linear calculations of the growth rate by the gyrokinetic simulation at each time step of the dynamical transport code such as TASK3D [6], because the transport analysis of helical plasmas demands a high radial resolution so as to accurately evaluate the radial electric field and the field configuration. In this study, how to apply the reduced model of the turbulent heat diffusivity for the ITG mode derived from the gyrokinetic simulation to the transport code is shown with a low computational cost. Modeling of the term $\mathcal{L}$ in the reduced model for the ITG mode is necessary to be involved with a parameter dependence of the plasma instability in the dynamical transport code. The ion temperature gradient scale length $L_{T_i}(= -T_i/(\partial T_i/\partial r))$ is chosen for the parameter to apply $\mathcal{L}$ to avoid the linear gyrokinetic analysis at each time step of the transport simulation. The field configuration is fixed at the initial state in the transport simulation. We have developed the formula for $\mathcal{L}$ in terms of L_{T_i}. The decay time of zonal flows depends on the magnetic field configuration and is independent of the plasma profile. The formula of the zonal flow decay time is needed to be calculated only at the initial state. The calculation by substituting these formulae for $\mathcal{L}$ and $\tilde{\tau}_{ZF}$ to the reduced model [3] reproduces the results of the reduced model itself within allowable errors. The computational cost to obtain the value of the turbulent ion heat diffusivity by this modeling at each time step of the transport simulation is much smaller than that of the linear gyrokinetic simulation. The simulation results for the high-T_i discharge of the shot number 88343 have been shown [7]. In this study, the modeling of the mixing length estimate term and the zonal flow decay time is done for the high-T_i discharge of #109081. The value of the density gradient scale length in the case of #109081 is different from that in the case of #88343. The density gradient scale length affects the characteristic of the ITG instability. This additional modeling is applied to the transport code and enables us to study the simulation results with the experimental results in LHD.

Firstly, the linear analysis is done using the GKV-X code for the additional modeling of the turbulent ion heat diffusivity. The ITG instability is examined in the high-T_i LHD discharge #88343 [8]. On the other hand, the analysis of the plasma dynamics using TASK3D was done for #109081 in LHD [9]. A reduced model for the ITG turbulent heat diffusivity in terms of the functions $\mathcal{L}\left(\equiv \int(\tilde{\gamma}_{\tilde{k}_y}/\tilde{k}_y^2)d\tilde{k}_y\right)$ and $\tilde{\tau}_{ZF}(= \tau_{ZF}/(R/v_{ti}))$ was obtained as $\chi_i/\chi_i^{GB} = A_1\mathcal{L}^{\alpha}/(A_2 + \tilde{\tau}_{ZF}/\mathcal{L}^{1/2})$, where χ_i^{GB} is the gyro-Bohm diffusivity, $\tilde{\gamma} = \gamma/(v_{ti}/R)$ and $\tilde{k}_y = k_y\rho_{ti}$. The numerical coefficients are given in [3]. The characteristic length of the ion temperature gradient is considered to be the important parameter for the ITG instability. As the function of L_{T_i}, the parameter $\mathcal{L}$ is modeled

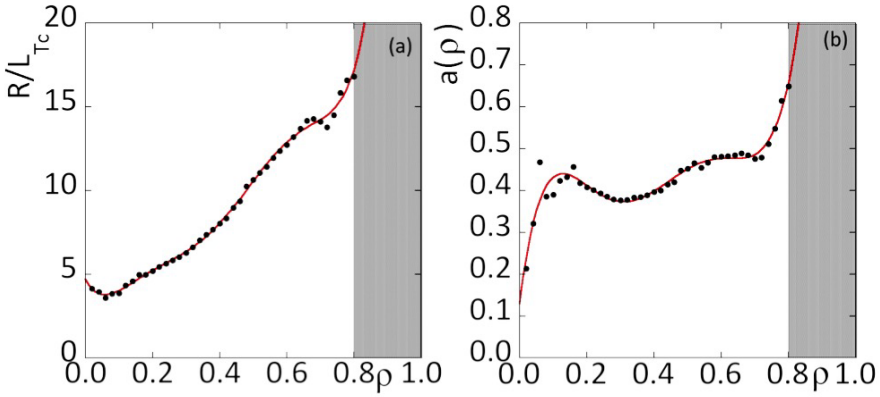

Figure 1: The radial dependence of (a) R/L_{T_c} and (b) $a(\rho)$ is shown with filled circles for #109081 in LHD.

by

$$\mathcal{L} = a(\rho)\left(\frac{R}{L_{T_i}} - \frac{R}{L_{T_c}}\right), \tag{1}$$

where L_{T_c} is the normalized critical ion temperature gradient for the ITG instability. To examine the critical ion temperature gradient for the ITG mode, the dependence of $\mathcal{L}$ on R/L_{T_i} is examined [10] with all plasma parameters fixed except the ion temperature gradient. The density and ion temperature profiles are obtained from the experimental results at $t = 2.233$s in the high-T_i LHD discharge #88343. The critical ion temperature gradient for the ITG mode, R/L_{T_c} and the slope $a(\rho)$ in terms of R/L_{T_i} are obtained. The fitting polynomials of R/L_{T_c} and $a(\rho)$ are used as $R/L_{T_c} = 4.0929 - 3.7681\rho + 19.712\rho^2 + 11.087\rho^3 - 14.272\rho^4$ and $a(\rho) = 0.38661 - 0.070919\rho + 0.2571\rho^2 + 0.95949\rho^3 - 0.92978\rho^4$. The comparison between the right hand side $(a(\rho)\,(R/L_{T_i} - R/L_{T_c}))$ and the left hand side $(\mathcal{L})$ in equation (1) is examined with the root mean square of $((a(\rho)\,(R/L_{T_i} - R/L_{T_c}))/\mathcal{L} - 1)$ given by $\sigma = 0.13$. The zonal flow decay time $\tilde{\tau}_{ZF}$ [5] is examined. The fitting function for the zonal flow decay time: $\tilde{\tau}_{ZF}(fit) = 0.98565 - 0.65943\rho + 2.4471\rho^2 + 3.2337\rho^3 - 2.8382\rho^4$ is used throughout the transport simulation. When we use the same modeling for the mixing length estimate and the zonal flow decay time at $t = 4.2$s for #109081 in LHD, the fitting polynomials of (a) the normalized ion temperature gradient R/L_{T_c} and (b) $a(\rho)$ are obtained as $R/L_{T_c} = 4.712 - 38.644\rho + 512.56\rho^2 - 2481\rho^3 + 5991.3\rho^4 - 6810.3\rho^5 + 2911.3\rho^6$ and $a(\rho) = 0.13049 + 6.3631\rho - 45.33\rho^2 + 134.8\rho^3 - 177.95\rho^4 + 90.153\rho^5 - 4.6622\rho^6$ in figure 1. The fitting function for $\tilde{\tau}_{ZF}$: $\tilde{\tau}_{ZF}(fit) = 0.34823 + 6.817\rho - 15.452\rho^2 + 15.972\rho^3 - 6.4126\rho^4$ is shown for the case of #109081 in LHD. To obtain the value of the turbulent ion heat diffusivity at each time step in the transport code, the value of the modeled turbulent ion heat diffusivity is calculated, where the term $a(\rho)(R/L_{T_i} - R/L_{T_c})$ is substituted for $\mathcal{L}$ and the fitting function $\tilde{\tau}_{ZF}(fit)$ is used for $\tilde{\tau}_{ZF}$.

Now, the transport dynamics is examined using the modeled turbulent ion heat diffusivity, when the TASK3D is performed. The radial profiles of the density and the electron temperature are fixed. The dynamics of the radial T_i profile is simulated by solving the diffusion equation. The profile of the radial electric field E_r is derived from the ambipolar condition at the initial plasma state. In #88343, three solutions of the ambipolar radial electric field are found in the radial region $0.265 \leq \rho \leq 0.785$. The profile of the radial electric field is dynamically fixed. The positive E_r is chosen. We study the simulation result of the T_i profile. The simulation results for the radial T_i profile show a good agreement with the experimental results. For modeling $\mathcal{L}$ in terms

of L_{T_i}, three runs at the different values of L_{T_i} are needed at a radial point before the dynamical transport simulation. It takes about twenty minutes per one time of the program run. If the value of $\mathcal{L}$ is calculated at each time step in the TASK3D, about one hundred thousand times of the program run are necessary. Therefore, the transport simulation of an extremely low computational cost can be achieved due to the additional modeling of the turbulent ion heat diffusivity based on the gyrokinetic simulation. In #109081, one negative radial electric field is shown from the ambipolar condition and is dynamically fixed. At the initial state, the ITG mode is stable in the region $0.0 \leq \rho \leq 0.8$. The simulation results using the diffusion equation for the ion temperature shows the higher value than the experimental results in the core region. At the plasma center, the value of T_i of the simulation result is 4.2keV, which is higher than the value of T_i: 3.2keV for the experimental results in LHD. The ITG mode becomes unstable in the region $0.18 \leq \rho \leq 0.42$ at the stationary state of the simulation results. However, the neoclassical transport is dominant compared with the turbulent transport driven by the ITG instability. In the case of #109081, the density profile is slightly peaky. The value of L_n becomes much smaller than the case in #88343, where the density profile is flattened. At $\rho = 0.5$, the values of $\eta_i (= L_n/L_{T_i})$ are -12.0 and 1.37 for #88343 and #109081 in LHD, respectively. In this study, we perform the gyrokinetic simulation with the adiabatic electrons. It is not enough for showing the T_i profile close to the experimental one only by the ITG stability analysis using the adiabatic electrons, especially for #109081 case. The gyrokinetic simulation with the kinetic electrons shows the larger ion heat flux than that by solving the gyrokinetic equation with the adiabatic electrons [11].

To reduce the simulation cost, how to apply the transport model based on a gyrokinetic simulation to a dynamical transport code is shown within the accuracy of the gyrokinetic simulation. The GKV-X code is performed for the additional modeling in terms of the ion temperature gradient scale length instead of the linear growth rate term for the ITG mode. The formula of the zonal flow decay time in the reduced model is derived at the given magnetic field structure. The simulation results by applying the additional modeled turbulent ion heat diffusivity to the dynamical transport code are shown. The promising technique of a low computational cost for adapting the gyrokinetic turbulent transport model to a transport code is proposed within allowable errors. The dynamical transport simulation of the #109081 in LHD clarifies the importance of the gyrokinetic simulation with the kinetic electrons. The construction of the reduced model for the heat diffusivity is needed by the electromagnetic gyrokinetic simulation with kinetic electrons. This is left for future study.

The authors are grateful to the LHD Experimental Group for making the experimental data available. This work was partly supported by JSPS KAKENHI Grant Number 23561002, the NIFS Collaboration Research program (Plasma Simulator), NIFS14KNST062 and the Collaborative Research Program of Research Institute for Applied Mechanics, Kyushu University, 27FP-11.

[1] Garbet X, Idomura Y, Villard L and Watanabe T -H 2010 *Nucl. Fusion* **50** 0433002
[2] Nunami M, Watanabe T -H, Sugama H and Tanaka K 2012 *Phys. Plasmas* **19** 042504
[3] Nunami M, Watanabe T -H and Sugama H 2013 *Phys. Plasmas* **20** 092307
[4] Sugama H and Watanabe T -H 2006 *Phys. Plasmas* **13** 012501
[5] Ferrando-Margalet S, Sugama H and Watanabe T -H 2007 *Phys. Plasmas* **14** 122505
[6] Yokoyama M, et al., 2012 *Plasma Fusion Res.* **7** 2403011
[7] Toda S, et al., 2014 *Journal of Physics: Conference Series* **561** 012020
[8] Tanaka K, et al. 2010 *Plasma Fusion Res.* **5** S2053
[9] Murakami S, et al., 2015 *Plasma Phys. Control. Fusion* **57** 054009
[10] Nunami M, Watanabe T -H, Sugama H and Tanaka K 2011 *Plasma Fusion Res.* **6** 001
[11] Ishizawa A, et al., 2015 *Nucl. Fusion* **55** 043024

13th Burning Plasma Simulation Initiative (BPSI) Meeting

Sensitivity and prediction of plasma profile in turbulent transport of helical plasmas

M. Nunami, M. Nakata, S. Toda, and H. Sugama

National Institute for Fusion Science, Toki 509-5292, Japan

Sensitivity to plasma temperature profile in turbulent transport of helical plasmas is discussed by the local flux-tube gyrokinetic simulations. Temperature profiles are reproduced from the experimental observation within experimental error bars which can be regarded as the standard deviation, and the allowable ranges of the ion temperature gradient within the errors can be estimated. According to the allowable ion temperature gradient, the permissible ranges of the ion heat diffusivity are expected. Furthermore, if the heat diffusivities are fixed with the flux-matching method, the radial profiles of the temperature gradients can be predicted.

1 Introduction

Turbulent transport has been considered to be one of the most critical issues in the magnetically confined plasmas researches. The gyrokinetic approaches are powerful to analyze the transport phenomena, which are considered to be driven by the drift-wave plasma turbulence. To design fusion reactors, especially, it is necessary to predict the transport fluxes, the plasma temperature and density profiles. The turbulent transport fluxes are quite sensitive to the profiles of the plasma temperature and density. Here, sensitivities of the transport fluxes to the plasma profiles are discussed within the experimental error ranges of the temperature profiles in helical plasmas. The allowable range of the temperature gradients is obtained from re-generated radial functions for ion temperature profiles, which is obtained by random sampling from the redistributed temperature data within experimental error bars which can be regarded as the standard deviations of the distributions.

2 Temperature gradient profiles within experimental errors

Radial profiles of plasma temperatures observed in the LHD experiments have the measurement error bars at each radial position. The error bars are regarded as the width of the standard deviation of the measurement data. Therefore, we can reproduce the temperature data by the normal distributions with the standard deviations which correspond to the experimental error

author's e-mail: nunami.masanori@nifs.ac.jp

bars. If the normal distributions for the plasma temperatures are reproduced at each radial position, we can give the ion temperature profiles by fitting the randomly sampling points from the reproduced data with the function,

$$T_{\rm i}(\rho) = \sum_{n=0}^{k} a_n \psi^n(\rho) = \sum_{n=0}^{k} b_n \rho^{2n}, \tag{1}$$

where the labeling index of the flux surfaces, $\rho \equiv \sqrt{\psi/\psi_{\rm a}}$, is a dimensionless quantity. Here ψ represents the toroidal magnetic flux, $\psi_{\rm a}$ is defined at the last closed surface, a_n and b_n are fitting coefficients. If the fitting functions for the ion temperature are obtained, the profile of the radial gradient of the temperature with a certain allowable ranges according to the experimental errors as shown in Fig. 1.

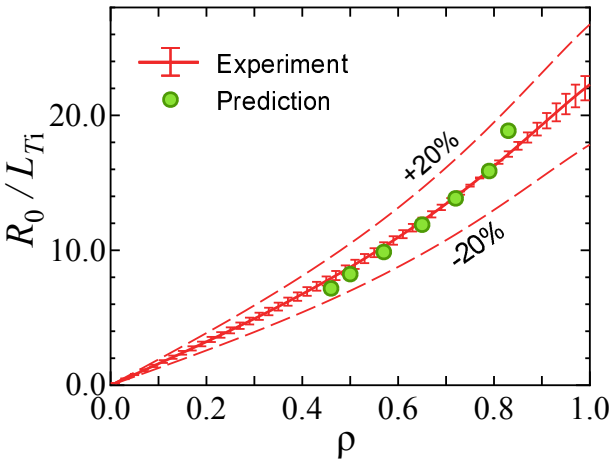

Fig. 1 Radial profile of the gradients of the ion temperature with the allowable ranges according to the experimental errors (red solid curves), and the predictions of the temperature gradients by the flux-matching method.

3 Permissible range of the transport coefficients

We perform the gyrokinetic analyses for the ITG turbulent transport by GKV codes[1, 2, 3] within the allowable range of the temperature gradients obtained in previous section. Figure 2 shows the ion heat diffusivities obtained by the ITG turbulence simulations and the LHD experiment. In outer radial region except for $\rho > 0.8$, the simulations within the experimental errors of the ion temperature can cover the experimental diffusivities, since the experimental errors enhance the ranges of the simulation results. In the core region, on the other hand, the simulation results have larger ambiguity rather than outer region, due to the fact that the experimental errors are larger in the core region. Up-shifts of the critical gradients from linear critical values are also observed and critical gradients go away from experimental values for more outer radial

region. In the outer radial region, there exists large density gradients which may cause the TEM instability, while the density profile in core region is almost flat.
On the other hand, if the heat diffusivities are fixed to match the experimental observations of the transport fluxes, the radial profiles of the temperature gradients can be predicted by so-called flux-matching method[4]. In fig. 1, we show the predictions of the ion temperature gradients, where the predictions agreed with the experimentally allowable ranges of the temperature gradients. Using the method, we may predict not only the temperature but also the density profiles against the error bars of the experimental density profile including the different instability sources such as the TEM.

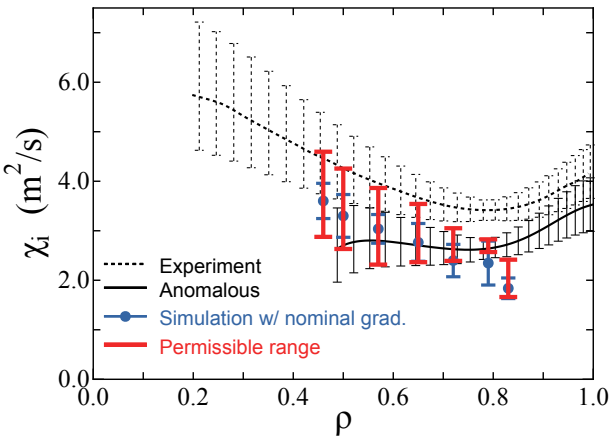

Fig. 2 Ion heat diffusivities obtained by the experiment (solid curve) and the gyrokinetic simulations (blue symbols) with nominal temperature gradients. The simulations within the error bars of temperature profile enhance the ranges (red error bars).

Acknowledgment

This work is supported in part by the RIAM collaborative Research Program (27FP-12), the Japanese Ministry of Education, Culture, Sports, Science, and Technology, Grant (26820398), NIFS collaborative Research Programs (KNTT031 and KNST080), and by use of Helios system at International Fusion Energy Research Center (Project code: VLDGK_ST and GKTBMDL).

[1] T.-H. Watanabe and H. Sugama, Nucl. Fusion **46**, 24 (2006).
[2] M. Nunami, T.-H. Watanabe, and H. Sugama, Plasma Fusion Res. **5**, 016 (2010).
[3] A. Ishizawa, *et al.*, 25th IAEA Fusion Energy Conference, TH/P6-40 (2014).
[4] T. Görler, *et al.*, Phys. Plasmas **21**, 122307 (2014).

Multi-species ITG-TEM turbulence simulations in ITER D-T-He plasma

Motoki NAKATA[1], Mitsuru HONDA[2], and Masanori NUNAMI[1]

National Institute for Fusion Science[1], Japan Atomic Energy Agency[2]

Multi-species ITG-TEM driven turbulent transport of D-T ions and He-ash in the burning plasmas is explored by electromagnetic gyrokinetic Vlasov simulations with realistic ITER-shape equilibria. Gyrokinetic-simulation-based quantitative evaluation of a steady burning condition is realized by comprehensive nonlinear scans, and the strong impacts of the D-T fuel ratio and He-ash on turbulent energy and particle fluxes are clarified. New findings in this study, which are crucial for the burning plasma performance, are (i) imbalanced D-T particle transport strongly influenced by He-ash accumulation, and (ii) identification of a profile regime in which the burning condition with He-ash exhaust and fuel inward-pinch is satisfied.

1 Introduction

The first-principle based gyrokinetic simulation is widely recognized as a promising way to predict turbulent transport in fusion plasmas, and nowadays the validation studies against existing experiments become more active[1–3], where reasonable agreement in the ion and electron heat fluxes between gyrokinetic simulations and experimental measurements has been confirmed. Burning plasmas in ITER and DEMO are always composed of multiple ion species such as fuel isotopes(D and T) and He-ash produced by the fusion reaction, and more complex turbulent transport processes are expected in comparison to the single-ion plasmas. Since simultaneous measurements of the kinetic profiles for all species are limited even in experiments, systematic studies on the particle and heat transport are indispensable to predict the confinement performance and to optimize the impurity exhausts and D/T fueling.

In this study, the ITG-TEM driven turbulent transport in realistic ITER D-T-He plasmas is investigated by a gyrokinetic Vlasov simulation GKV[4,5] with multiple ions and fully kinetic electrons including their inter-species collisions[6,7], where a good prediction capability has been confirmed against the actual JT-60U tokamak L-mode experiment[3]. In addition to the D-T fuel ratio dependence of the turbulent transport levels, we explore, for the first time, an optimum profile regime, which satisfies the steady burning condition[8] with efficient He-ash exhaust and fuel inward-pinch, from the gyrokinetic-simulation point of view.

2 Impacts of D-T ratio and He-ash on turbulent transport

Nonlinear gyrokinetic Vlasov simulations with D, T, He, and real-mass kinetic electrons are performed for an ITG-TEM unstable plasma with realistic ITER-shape[5], where the normalized temperature and density gradient lengths at $\rho = 0.5$ are set as $R_{\rm ax}/L_{T_{\rm i}} = 6$, $R_{\rm ax}/L_{T_{\rm e}} = 8$, and $R_{\rm ax}/L_n = 2$, respectively. The GKV simulations reveal different saturation levels and spatial structures of the turbulent fluctuations in D-T ions and He-ash [cf. Fig. 1(c)], and each transport level is evaluated by the time average in the quasi-steady phases of the ITG-TEM turbulence. Figures 1(a) and 1(b) show the impact of the D-T fuel ratio $n_{\rm T}/(n_{\rm T} + n_{\rm D})$ on the turbulent energy and particle transport levels of D and T in the case with and without He-ash, where the ion fluxes are normalized by the electron one. One finds that the D-T energy fluxes $Q_{\rm D,T}/Q_{\rm e}$ are reduced by the He-ash accumulation, but the overall tendency of the linear D-T ratio dependence is unchanged [Fig. 1(a)], e.g., $Q_{\rm D} \simeq Q_{\rm T}$ at the almost 50%-50% D-T ratio, regardless of the He-ash accumulation. On the other hand, in the particle fluxes $\Gamma_{\rm D,T}/\Gamma_{\rm e}$, imbalanced D-T transport due to the nonlinear D-T ratio dependence is revealed [Fig. 1(b)], where $\Gamma_{\rm D} \neq \Gamma_{\rm T}$ even at 50%-50% D-T ratio. Moreover, the He-ash accumulation leads to not only the reduction in the particle flux levels, but also stronger imbalance of the D-T particle transport.

3 GK-simulation-based evaluation of burning condition

In addition to the D-T ratio dependence of the turbulent transport, the present multi-ion species gyrokinetic simulations with He-ash can provide the quantitative evaluation of the steady burning condition which is never addressed by the single-ion approaches. For sustainable fusion reactions with the efficient He-ash exhaust(outward flux) and fuel pinch(inward flux), a steady burning condition is given by $\Gamma_{\rm He} > 0$, $\Gamma_{\rm D,T} < 0$, and $\eta_{\rm i} T_{\rm i} \Gamma_{\rm He} > Q_{\rm i}/\alpha^*$ (or equivalently $\tau_{\rm He} < \alpha^* \tau_{\rm E}$), where $\alpha^* \sim 7 - 15$ is a constant depending on the divertor and wall conditions[8]. To this end, the density gradient($R_{\rm ax}/L_n$) scans of the steady turbulent energy and particle transport levels are performed. As shown in Fig. 2(a), it is clearly identified that there exists a profile regime of $R_{\rm ax}/L_n \leq 1.27$(hatched region) in which the above steady burning condition with $\alpha^* = 7$ is satisfied. The spectral analysis of the turbulent particle fluxes of He-ash and Tritium reveals that, in contrast to the weak $R_{\rm ax}/L_n$ dependence of the outward He-ash flux, the components of the inward Tritium flux increase for the lower $R_{\rm ax}/L_n$, indicating significant off-diagonal effects ($\propto R_{\rm ax}/L_{T_{\rm i}}$) on the particle transport.

4 Summary

In this study, multi-species ITG-TEM driven turbulent transport of D-T ions and He-ash in the burning plasmas is explored by electromagnetic gyrokinetic Vlasov simulations with realistic ITER-shape equilibria. Gyrokinetic-simulation-based quantitative evaluation of a steady burning condition is realized by comprehensive nonlinear scans, and the strong

impacts of the D-T fuel ratio and He-ash on turbulent energy and particle fluxes are clarified. These findings on the He-ash impact and on the profile dependence for the steady burning condition can contribute to deeper understanding of the multi-species transport processes in tokamak and helical burning plasmas, and encourage the quantitative predictions and optimization for forthcoming ITER and DEMO.

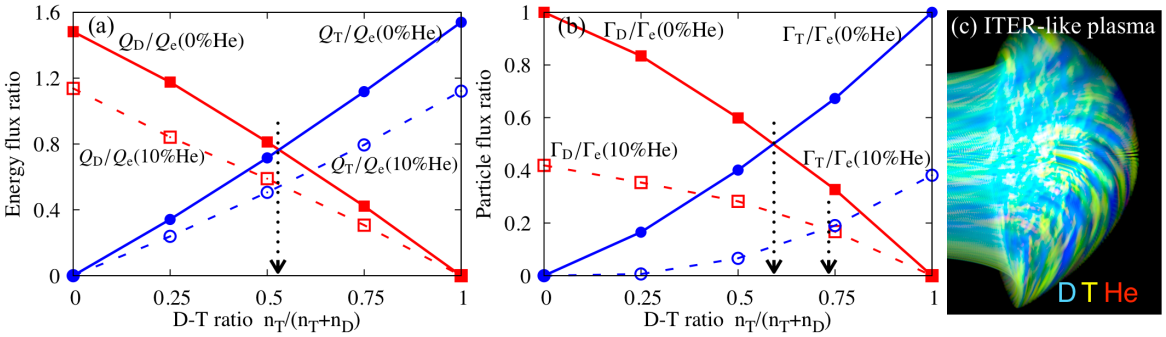

Figure 1: D-T ratio dependencies of (a) energy and (b) particle fluxes for D and T normalized by the electron flux, where the cases with 0%(solid lines) and 10%(dashed lines) He-ash are plotted. Imbalanced turbulent fluxes significantly appear in the D-T particle transport, rather than the energy transport. (c)Turbulent fluctuations of D(blue), T(yellow), and He(red) in the multi-species ITG-TEM turbulence.

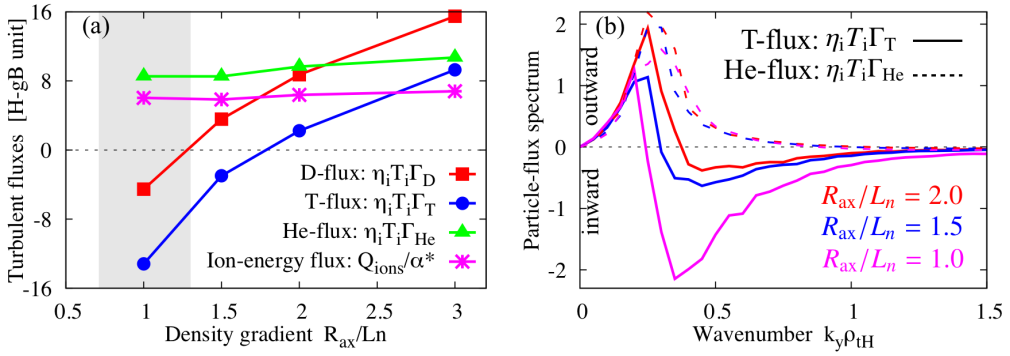

Figure 2: (a) Density-gradient scan of turbulent particle and ion energy fluxes, where the steady burning condition with $\alpha^* = 7$ is satisfied in $R_{ax}/L_n \leq 1.27$(hatched region). (b) Wavenumber spectra of Tritium and He-ash fluxes at several density gradients, where the inward-flux components appear in Tritium.

Reference

[1] T. L. Rhodes, C. Holland *et al.*, Nucl. Fusion **51** 063022 (2011)
[2] T. Golrer, A. E. White *et al.*, Phys. Plasmas **21** 122307 (2014)
[3] M. Nakata, M. Honda *et al.*, Proc. on the IAEA-FEC2014, THP7-38 (2014)
[4] T. -H. Watanabe and H. Sugama, Nucl. Fusion **46** 24 (2015)
[5] M. Nakata, A. Matsuyama *et al.*, Plasma Fusion Res. **9** 1403029 (2014)
[6] M. Nakata, M. Nunami *et al.*, Comput. Phys. Commun., **197** 61 (2015)
[7] M. Nunami, M. Nakata *et al.*, Plasma Fusion Res. **10** 1403058 (2015)
[8] D. Reiter, G. H. Wolf *et al.*, Nucl. Fusion **30** 2141 (1990)

トロイダルプラズマにおける乱流と計測に関する

シミュレーション研究

Simulation study of turbulence and diagnostic in toroidal plasmas

N. Kasuya, K. Kawadu [1], M. Nunami [2] and M. Yagi [3]
Research Institute for Applied Mechanics, Kyushu University, Kasuga, Fukuoka 816-8580, Japan
[1] Interdisciplinary Graduate School of Engineering Sciences, Kyushu University, Kasuga, Fukuoka 816-8580, Japan
[2] National Institute for Fusion Science, Toki, Gifu 509-5292, Japan
[3] Japan Atomic Energy Agency, Obuchi, Rokkasho-mura, Aomori 039-3212, Japan
E-mail: kasuya@riam.kyushu-u.ac.jp

Resent turbulence simulations in three-dimensional (3-D) magnetically confined plasmas show the various aspects of plasma turbulence [1]. We have been carrying out numerical diagnostics using 3-D simulation data of helical plasmas. Here we present the turbulence analysis results (i) from simplified geometry for detailed nonlinear mechanism of heat transport, and (ii) from real 3-D geometry for comparison with experimental observations. Competition of various temporal and spatial scales involved in the model, turbulent structures revealed in the transient response, and their features through the observation are shown from the numerical diagnostics.

Many turbulence codes have been developed for the calculation in experimental magnetic configurations. For the helical plasmas, using the GKV-X code, which is the gyrokinetic Vlasov code with 3-D equilibrium, quantitative comparisons with experiments have been carried out [2]. On the other hand, a reduced fluid code with simplified magnetic configuration [3] is also useful for the fundamental understandings. It is important to integrate the results from the various approaches. One of the ways for the integration is by analyzing the various simulation data with the routines to give same diagnostics. Turbulence Diagnostic Simulator (TDS) [4] is a combination of turbulence codes, measurement modules and analysis routines, to carry out numerical experiments of plasma turbulence, which can be utilized as the platform of the data analyses. The turbulence features revealed from the TDS are explained in this paper.

First, the fundamental mechanism with simplified configuration, which has a circular poloidal-cross-section, is described. Global nonlinear simulations of drift-interchange modes in helical plasmas are carried out using a reduced MHD model [3]. The averaging with the helical pitch is adopted, so the configuration can be treated as a quasi-2-D one with the helical magnetic curvature. The model is used as the fundamental one including the global and localized modes, nonlinear couplings with the Reynolds stress, and collisional transport processes. The nonlinear saturated states are sustained with an applied heat source, and the mode structures broadened in the radial direction and localized near their rational surfaces are both excited. These fluctuations have the self-correlation time of 30τ, though those of higher m modes are smaller than 10τ, where τ is the ion acoustic time and m is the poloidal mode number. A non-local effect has been studied in dynamical transport phenomena by the simulation of the heat source modulation [3]. The nonlinear process plays the key role in the

response, which takes a finite temporal duration ~ 30τ for the energy redistribution. By conditional averaging, the characteristic response can be extracted. Figure 1 shows the 2-D pattern of the heat flux to propagate the modulation from the core to the edge. A spiral stream line appears, rotating to the electron diamagnetic direction with the ballooning feature. This structure is not a linear mode structure, but a nonlinearly formed one, and is sustained for ~100τ that is longer than the turbulence decorrelation time. Concerning the electromagnetic aspect, the other time scale appears. There exists an oscillation with the period of ~ 160τ. The model equation reduced with the ordering in the simulation gives an Alfvénic oscillation of the m = 1 modes, whose nonlinear couplings are found to give the oscillation of the mean components. In addition, flattening by the magnetic curvature in the pressure evolution stabilizes the mode strongly. In this way, the reduced model can reveal the competition of various time-scales, when the MHD modes with a rather long wave-length play the main role in the saturation.

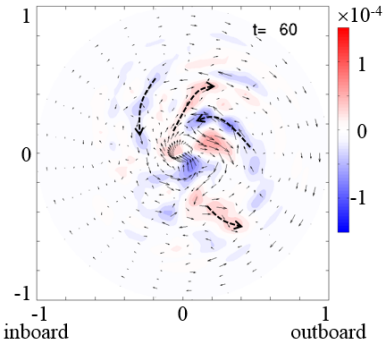

Fig.1: Conditional averaged 2-D pattern of heat flux in the poloidal cross-section of the torus plasm

Next, the case with the 3-D equilibrium and shorter wave-length perturbations is explained. Flux-tube simulations of Ion-Temperature-Gradient modes in the LHD configuration have been carried out with the GKV-X code. Quantitative comparison of the thermal diffusivity coefficient has shown the good agreement with experiments [2], and other turbulent characteristics, such as the perturbation spectrum, should be compared for the validation. We develop an analysis routine for the GKV-X data taking into account of the line of sight of the experimental diagnostics. The code uses the magnetic surface coordinate, so the interpolation is necessary for evaluating the physical quantities in the real space. The spatial resolutions are limited by those of the simulation, δr ~ 0.4 [mm] and $\delta\phi$ ~ 50 [mm]. For the 2-D spectrum analysis of density perturbation, 2-D profiles are obtained (Fig. 2). Efficiency of the method to resolve the local spectrum is tested. Assuming $k_{//} = 0$, the typical k direction (k_y / k_x) can be set, corresponding to the magnetic field direction. The magnetic field direction changes with the variation of the magnetic field in the vertical direction, which can use for the reconstruction in helical plasmas. The extracted component is dominant in the certain vertical position, but the contributions from the other positions are not negligible, due to non-zero $k_{//}$, so can use the estimation of the experimental error bars.

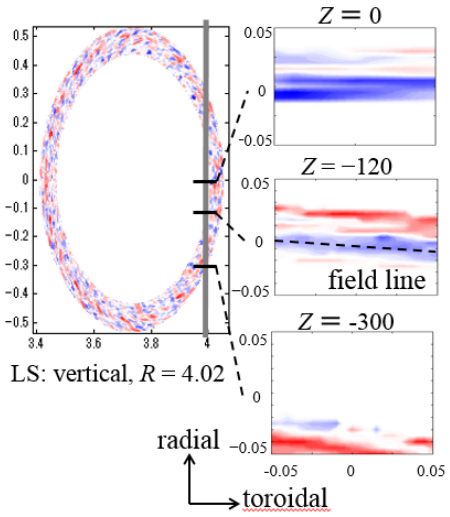

Fig. 2: Poloidal cross-section of perturbations and its local patterns at different vertical positions along the line of sight.

In this way, the numerical diagnostics have been carried out in the 3-D torus magnetic configurations. Variety of the numerical diagnostics from several view-points can give physical understanding and quantitative comparison of turbulent plasmas.

Acknowledgements
Authors acknowledge discussions with Professor K. Itoh, Professor S.-I. Itoh, Professor S. Inagaki, Professor H. Sugama and Dr. M. Sasaki. This work is supported by the Grant-in-Aid for Young Scientists (24760703), for Scientific Research (23244113) of JSPS, by the collaboration program of NIFS (NIFS15KNST082, NIFS15KNTS040, NIFS13KOCT001) and of RIAM of Kyushu University. Some numerical simulations were carried out on the Plasma Simulator at National Institute for Fusion Science and the Helios Super Computer System at Computational Simulation Center of International Fusion Energy Research Center.

References
[1] X. Garbet, *et al.*, Nucl. Fusion **50** (2010) 043002.
[2] M. Nunami, *et al*., Phys. Plasmas **19** (2012) 042504.
[3] N. Kasuya, *et al.*, Phys. Plasmas **21** (2014) 110701.
[4] N. Kasuya, *et al.*, Plasma Fusion Res. **8** (2013) 2403070.

Development of the multi-fluid transport code on the tokamak flux coordinates

M. Honda[1], A. Fukuyama[2]

[1] *Japan Atomic Energy Agency, Naka, Japan*

[2] *Graduate School of Engineering, Kyoto University, Kyoto, Japan*

Introduction

We have developed a one-dimensional fluid-type transport code TASK/TX [1] in the cylindrical coordinates. The code is essentially based on a self-consistent two-fluid model, which consists of two-fluid equations (conservation of mass, momentum and energy) plus Maxwell's equations. It also involves the equations for beam ions and neutrals. It differs from conventional diffusive transport codes mainly in that: the quasi-neutrality condition $n_e = \sum_i Z_i n_i$ need not be imposed and the ambipolar flux condition $\sum_a \Gamma_a = 0$ is intrinsically satisfied; the flux-gradient relationship is not used for particle transport; the neoclassical features are self-consistently reproduced. Here we derive the governing equations of TASK/TX on the axisymmetric flux coordinates (ρ, θ, ζ) and then numerically implement them.

Maxwell's equations

On the axisymmetric flux coordinates, the magnetic field is expressed as $\boldsymbol{B} = \nabla\zeta \times \nabla\psi + I\nabla\zeta$, where $I(\psi) = RB_t$. Maxwell's equations consist of Gauss's law (Poisson's equation), Faraday's law and Ampère's law. From Faraday's law $\boldsymbol{E} = -\nabla\Phi - \dot{\boldsymbol{A}}$, it is found that the covariant components of the electric fields are strongly tied to (the temporal change in) the magnetic fluxes: $E_\theta = \boldsymbol{E} \cdot \sqrt{g}\nabla\zeta \times \nabla\rho = -\dot{\psi}_t, E_\zeta = g_{\zeta\zeta}\boldsymbol{E} \cdot \nabla\zeta = \dot{\psi}(= RE_t)$. Ampère's law relates (the spatial gradient of) the magnetic flux to the current. Taking the scalar product of Ampère's law with $\nabla\zeta$ and the subsequent flux-surface average (FSA) yield (cf. FSA Grad-Shafranov equation)

$$\frac{1}{c^2}\frac{\partial\dot{\psi}}{\partial t} = \frac{1}{V'\langle R^{-2}\rangle}\frac{\partial}{\partial\rho}\left[V'\left\langle\frac{|\nabla\rho|^2}{R^2}\right\rangle\frac{\partial\psi}{\partial\rho}\right] - \mu_0\frac{\langle j^\zeta\rangle}{\langle R^{-2}\rangle}, \quad \frac{\partial\psi}{\partial t} \equiv \dot{\psi}, \tag{1}$$

the latter of which is not only the definition of $\dot{\psi}$ but also one of the governing equations that constitutes Maxwell's equations. This is because it is just alternative form of Faraday's law. Taking the scalar product of Ampère's law with $\boldsymbol{B}$ and then subtracting (1) give the equations for the toroidal flux in the form:

$$\frac{1}{c^2}\frac{\partial\dot{\psi}_t}{\partial t} = V'\left\langle\frac{|\nabla\rho|^2}{R^2}\right\rangle\frac{\partial}{\partial\rho}\left[\frac{1}{V'\langle R^{-2}\rangle}\frac{\partial\psi_t}{\partial\rho}\right] + \mu_0\frac{\langle Bj_\parallel\rangle - I\langle j^\zeta\rangle}{\langle B^\theta\rangle}, \quad \frac{\partial\psi_t}{\partial t} \equiv \dot{\psi}_t. \tag{2}$$

When neglecting the displacement current term that is negligibly small, we readily find that the right-hand sides of (1) and (2) reproduce the expressions of the toroidal and parallel currents. Finally, the Coulomb gauge allows us to simply write FSA Gauss's law as follows:

$$\frac{1}{V'}\frac{\partial}{\partial\rho}\left[V'\langle|\nabla\rho|^2\rangle\frac{\partial\Phi}{\partial\rho}\right] = -\frac{1}{\epsilon_0}\sum_a e_a n_a. \tag{3}$$

Continuity equations

A flux-surface-averaged continuity equation is simply given by

$$\frac{1}{V'}\frac{\partial}{\partial t}(V'n_a)\bigg|_\rho + \frac{1}{V'}\frac{\partial}{\partial\rho}[V'n_a\langle(\boldsymbol{u}_a-\boldsymbol{u}_g)\cdot\nabla\rho\rangle] = S_{\mathrm{n}a}. \tag{4}$$

TASK/TX is distinguished from other transport codes in that $n_a\langle(\boldsymbol{u}_a-\boldsymbol{u}_g)\cdot\nabla\rho\rangle$ is not approximated by the convection-diffusion relationship, but is treated as a dependent variable: The grid velocity $\boldsymbol{u}_g$ and the flux $n_a\langle\boldsymbol{u}_a\cdot\nabla\rho\rangle$ are both self-consistently calculated in the system.

Momentum equations

The parallel motion of plasma species regulates neoclassical properties in axisymmetric systems. The lowest order of the viscous term is the neoclassical viscosity. The viscous term and the friction term can be calculated according to the moment approach [2]. Therefore, defining $\langle B\hat{q}_{a\|}\rangle = 2\langle Bq_{a\|}\rangle/(5p_a)$, the following equations should be solved:

$$\begin{aligned} m_a n_a\frac{\partial\langle Bu_{a\|}\rangle}{\partial t} =& -\hat{\mu}_1^a(\langle Bu_{a\|}\rangle - BV_{1a}) - \hat{\mu}_2^a(\langle B\hat{q}_{a\|}\rangle - BV_{2a}) + \sum_b \ell_{11}^{\mathrm{ab}}\langle Bu_{a\|}\rangle - \sum_b \ell_{12}^{\mathrm{ab}}\langle Bu_{a\|}\rangle \\ &+ e_a n_a\langle BE_\|\rangle, \end{aligned} \tag{5}$$

$$\frac{5}{2}m_a n_a\frac{\partial\langle B\hat{q}_{a\|}\rangle}{\partial t} = -\hat{\mu}_2^a(\langle Bu_{a\|}\rangle - BV_{1a}) - \hat{\mu}_3^a(\langle B\hat{q}_{a\|}\rangle - BV_{2a}) - \sum_b \ell_{21}^{\mathrm{ab}}\langle Bu_{a\|}\rangle + \sum_b \ell_{22}^{\mathrm{ab}}\langle B\hat{q}_{b\|}\rangle. \tag{6}$$

The toroidal momentum equation is important for TASK/TX because it includes the $\boldsymbol{v}\cdot\nabla\rho$ term that provokes a particle flux as well as a $\boldsymbol{j}\times\boldsymbol{B}$ torque once losses of beam ions produce the non-ambipolar flux. In conventional transport codes the particle transport coefficients evaluated by external modules are directly substituted in the particle transport equation, whereas in TASK/TX coupling of the equations self-consistently brings about particle transport through the continuity equation. While the first-order viscous stress term vanishes due to the CGL form, the second-order term can be expressed as a combination of a convective momentum flux, a.k.a. inward pinch, and a diffusive one plus a residual stress. We have to add a turbulent force F_a^{QL} that drives a turbulence-induced quasilinear particle flux. The toroidal momentum equation is

finally given by, where $\langle \mathcal{L}_a \rangle \equiv m_a n_a \langle R u_{a\zeta} \rangle$,

$$\frac{1}{V'}\frac{\partial}{\partial t}(V'\langle \mathcal{L}_a \rangle) = -\frac{1}{V'}\frac{\partial}{\partial \rho}V'\Bigg[\langle |\nabla\rho| \rangle \nu_{a\zeta}\langle \mathcal{L}_a \rangle + (u_a^\rho - u_g^\rho)\langle \mathcal{L}_a \rangle - \langle |\nabla\rho|^2 \rangle \chi_{a\zeta} m_a n_a \frac{\partial \langle R u_{a\zeta} \rangle}{\partial \rho} + \langle \Pi_a^{\rm res} \rangle\Bigg] + \sum_b \ell_{11}^{\rm ab}\langle R u_{b\zeta} \rangle - \sum_b \ell_{12}^{\rm ab}\frac{I}{\langle B^2 \rangle}\langle B \hat{q}_{b\parallel} \rangle + e_a n_a \langle R E_\zeta \rangle + e_a \frac{\partial \psi}{\partial \rho} n_a u_a^\rho. \quad (7)$$

The radial momentum equation or the radial force balance equation is essentially equivalent to the first-order flow within the flux surface. The leading order in δ is $O(1)$ for pressure and Lorentz force terms, and the other terms are practically ineffective. Thus, we obtain

$$0 = -\frac{1}{m_a}\frac{\partial p_a}{\partial \psi}(\langle B^2 \rangle \langle R^2 \rangle - I^2) - \frac{e_a}{m_a} n_a \frac{\partial \Phi}{\partial \psi}(\langle B^2 \rangle \langle R^2 \rangle - I^2) + \frac{e_a}{m_a} n_a I \langle B u_{a\parallel} \rangle - \frac{e_a}{m_a} n_a \langle B^2 \rangle \langle R u_{a\zeta} \rangle. \quad (8)$$

Numerical results

For the sake of simplicity, the large aspect ratio plasma with circular cross section is assumed. JT-60U-like plasma parameters are given in the following simulation. Figure 1 shows the radial profiles of (left) the difference in the charge density and the resultant E_r, indicating that automatically the quasi-neutrality is well satisfied and the ambipolar flux condition is satisfied as well. A break of the local charge neutrality in the core region, $(n_{\rm e} - n_{\rm i})/n_{\rm e}$, is of the order of 10^{-7}, which is always neglected in conventional transport codes, but this tiny discrepancy is indispensable to give rise to the radial electric field E_r through Eq. (3). The right figure shows the comparison of the parallel current profiles estimated by TASK/TX and three neoclassical transport model/modules. The breakdown of the current in TASK/TX cannot be known, but we find that the parallel current calculated by TASK/TX well agrees with that by other models.

This work was supported by JSPS KAKENHI (No. 25820442).

References

[1] M. Honda and A. Fukuyama, J. Comput. Phys. **227**, 2808 (2008).

[2] S. P. Hirshman and D. J. Sigmar, Nucl. Fusion **21**, (1981) 1079.

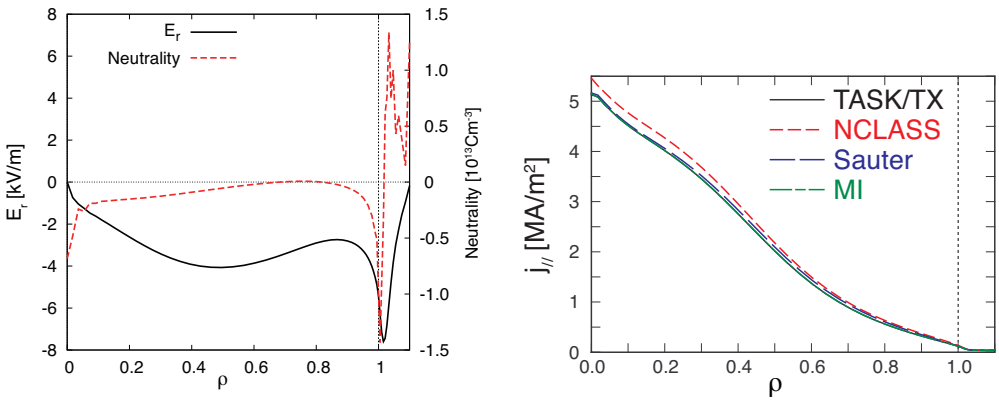

Figure 1: Radial profiles of (left) E_r and quasi-neutrality and (right) the parallel current.

Bifurcation of the interchange mode growth rate and rotation frequency due to the perpendicular heat conductivity

T. Nicolas[1], K. Ichiguchi[1,2], Y. Todo[1,2], M. Sato[1], Y. Suzuki[1,2], and A. Ishizawa[1,2]

[1] *National Institute for Fusion Science, 322-6 Oroshi-cho, Toki 509-5292, Japan*
[2] *The Graduate University of Advanced Study, Sokendai, Toki 509-5292, Japan*

The linear stability against interchange modes of heliotrons like the Large Helical Device has not been fully understood yet. The interchange mode is the dominant instability in nearly current-free 3D configurations. Recently, experiments in the so-called inward-shifted configuration have shown the machine can be operated safely up to $\langle\beta\rangle \sim 5\%$ without major MHD event [1]. Here $\langle\beta\rangle$ is the volume averaged ratio between kinetic and magnetic pressure. The rotation of the mode, which seems to play a role in the stability [2], is also not understood. Namely, the modes are observed to rotate in the electron direction [3], whereas extended MHD theory without heat conductivity but including electron and ion diamagnetic effects predicts rotation in the ion direction for Mercier unstable modes and almost no rotation for Mercier stable modes [4].

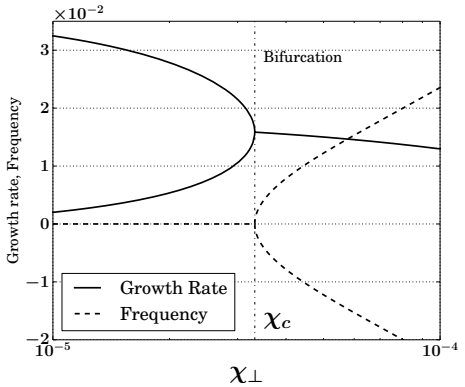

Figure 1: Frequency and growth rate of the first two most unstable modes

In this contribution, we present a new effect on the linear Mercier unstable interchange growth rate caused by the perpendicular heat conductivity $\chi_\perp$. When the heat conductivity is introduced in a 3-field reduced model of Strauss type equations [5], it is found that a second mode with an interchange parity and no sign change in the potential wave function appears, in addition to the usual most unstable interchange mode. The second mode is more stable, so its growth rate is lower. As can be seen in Fig 1, for small values of the heat conductivity, the two modes have zero frequency and converge toward each other when $\chi_\perp$ is increased. When $\chi_\perp$ is equal to a critical value χ_c, the growth rates of the two most unstable modes become equal. For $\chi_\perp > \chi_c$, the two modes have same growth rate and opposite frequency, as shown in Fig. 1. Therefore there is a degeneracy, since two modes have the same growth rate, but opposite frequencies. If the plasma is in this regime, then the observation of the linear phase of the interchange mode corresponds to standing waves. The direction of rotation of the mode cannot be identified.

This degeneracy is removed by the diamagnetic effects. In the domain $\chi_\perp > \chi_c$, the diamagnetic flows have a very different effect compared to what happens for ideal modes. For ideal modes, the diamagnetic effects are such that the growth rate and frequency of

Corresponding author: Timothee Nicolas timothee.nicolas@nifs.ac.jp

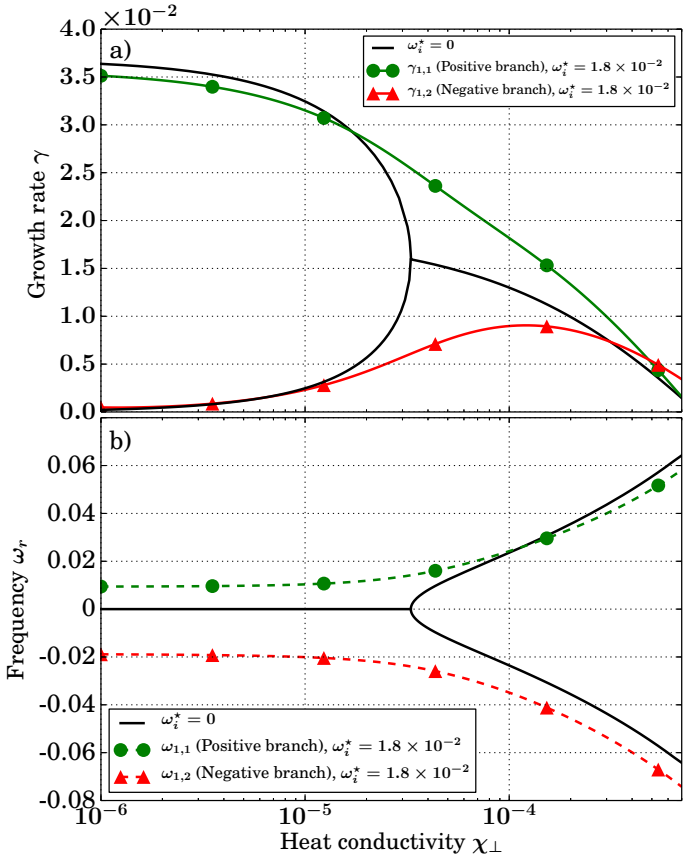

Figure 2: Frequency and growth rate of the first two most unstable modes with diamagnetic effects $\omega_I^\star = 1.8 \times 10^{-2}$ and no viscosity

the interchange mode are given [6] by

$$\begin{cases} \gamma = \gamma_I \sqrt{1 - \dfrac{\omega_i^\star}{2\gamma_I}} \\ \omega = \dfrac{1}{2}\omega_i^\star \end{cases} , \tag{1}$$

where $\omega_i^\star$ and γ_I are the ion diamagnetic frequency and the ideal growth rate respectively. This law is approximately valid for small values of the heat conductivity, resistivity and viscosity. However, in the domain $\chi_\perp > \chi_c$, this law is not valid anymore. There are two cases. If there is no viscosity, then the most unstable mode is destabilized and the second most unstable mode is stabilized. The frequency of the most unstable mode is in the ion direction, so the mode rotates in the ion direction. This situation is shown in Fig. 2. In the second case, if there is a viscosity large enough to affect the ideal growth rate, then the most unstable mode is stabilized whereas the most stable mode, rotating in the electron direction, is destabilized. As a result, the mode rotation, which is still given

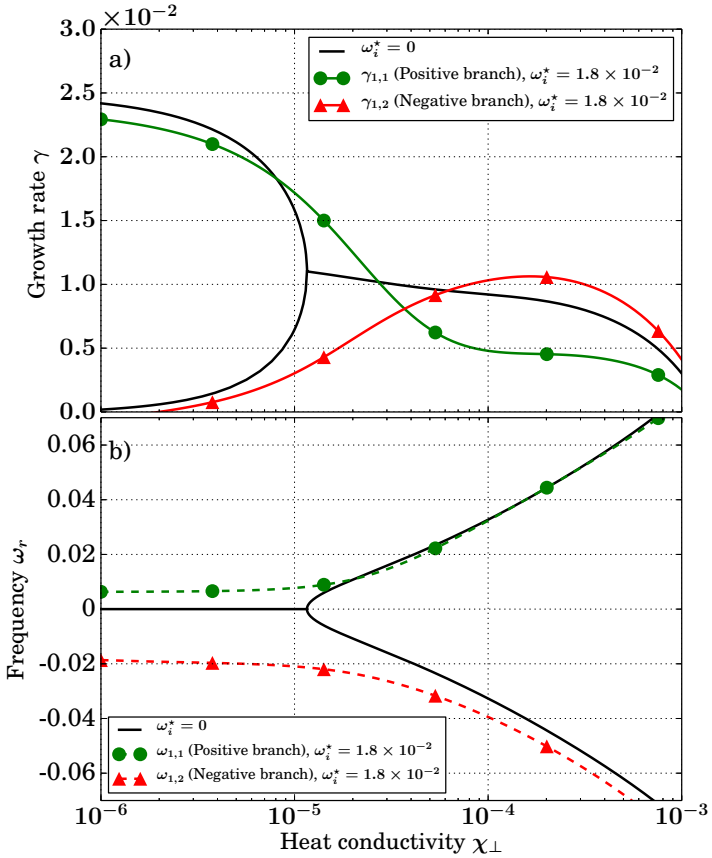

Figure 3: Frequency and growth rate of the first two most unstable modes with diamagnetic effects $\omega_I^\star = 1.8 \times 10^{-2}$ and viscosity $\nu = 10^{-5}$.

by the dominant mode, is in the electron direction, as shown in Fig. 3.

This effect, which sheds a new light on the stability of the interchange mode in stellarators, is also found analytically and confirmed with 3D non-linear MHD simulations utilizing the MIPS code [8, 9]. In the MIPS simulations, the linear phase of an ideally unstable interchange mode is simulated in presence of some resistivity, viscosity and heat conductivity. For large values of β, the relative effect of dissipation is small and a result similar to the ideal case is found. For smaller values of β, closer to marginal stability but still in the ideally unstable domain, it is found that the diamagnetic effects are destabilizing for small values of $\omega_i^\star$, and that the mode rotates in the electron direction, rather than in the ion direction.

These results are detailed in references [8] and [9].

References

[1] H. Yamada *et al.* Nucl. Fusion **51(9)**, 4021 (2011).

[2] Y. Takemura, *et al.* Nucl. Fusion **52(10)**, 102001 (2012).

[3] Y. Takemura, *et al.* Plasma and Fusion Research **8(0)**, 1402123 (2013).

[4] S. Gupta, *et al.* Phys. Plasmas **9(8)**, 3395 (2002).

[5] H. Strauss. Plasma Physics **22(7)**, 733 (1980).

[6] J. Connor, *et al.* Nucl. Fusion **24(8)**, 1023 (1984).

[7] Y. Todo, *et al.* Plasma and Fusion Research **5**, S2062 (2010).

[8] T. Nicolas *et al.* Nucl. Fusion **56(2)**, 026008 (2015).

[9] T. Nicolas, *et al.* Plasma and Fusion Research **(10)** (2015).

Fokker-Planck Simulation for Runaway Electron Generation including the Hot-tail Effect

H. NUGA[1], A. MATSUYAMA[2], M. YAGI[2], A. FUKUYAMA[1]

[1]Department of Nuclear Engineering, Kyoto University
[2]Japan Atomic Energy Agency

Introduction In large size tokamak, such as ITER, disruptions have a potential to generate the runaway electron current which can reach to a few mega-amperes. Because in ITER, mitigated disruptions by means of the massive gas injection (MGI) tends to yield the shorter thermal quench time than in unmitigated disruptions, so-called hot-tail effect[1, 2] might enhance the "primary" runaway electron (RE) generation rate, which requires full kinetic calculation of the RE generation process.

The aim of this paper is to compare the RE generation, especially RE current density profile, including and excluding the hot-tail effect in ITER. For this purpose, the Fokker-Planck code, named TASK/FP[3], is applied to simulations of the evolution of the relativistic electron momentum distribution function, the RE current, and the induced electric field in a self-consistent manner. The code treats the electron distribution function in two-dimensional momentum space for sub-relativistic region (less than 0.5 MeV). In the present calculation, though the treatment of relativistic REs is simplified, the thermal and sub-relativistic electron distribution function is analyzed with a good resolution, being useful for detailed calculation of the primary RE generation rate.

The RE generation in a high-current tokamak like ITER is expected to be dominated by the "secondary" generation. Nevertheless, our simulation shows that the hot-tail formation plays an important role in determining the RE current profile after the current quench. Since even a small increment of the seed current density is amplified by the avalanche effect, the secondary RE current density profile is modified by the hot-tail effect.

Models In our present research, we have developed a Fokker-Planck simulation code TASK/FP in order to calculate the time evolution of the relativistic momentum distribution function and that of induced toroidal electric field self-consistently. It solves the Fokker-Planck equation:

$$\frac{\partial f}{\partial t} = -\nabla \cdot \boldsymbol{S}_{\boldsymbol{C},\boldsymbol{E}} = -\nabla \cdot \left(\overleftrightarrow{\boldsymbol{D}}_C \cdot \nabla f + \boldsymbol{F}_{C,E} f, \right) \tag{1}$$

where ∇ is a derivative operator in momentum space and f is a relativistic electron momentum distribution function. In this paper, the weak relativistic isotropic background collision term[4] with relativistic Maxwellian is adopted for $\overleftrightarrow{\boldsymbol{D}}_C$ and $\boldsymbol{F}_C$.

The induced electric field E obeys following equations:

$$\frac{dn_{rp}}{dt} = \int \nabla \cdot \boldsymbol{S}_{C,E} d\boldsymbol{p} \tag{2}$$

$$\frac{\mathrm{d}n_{rs}}{\mathrm{d}t} = n_r \frac{\bar{E} - 1}{\tau_r \ln \Lambda} \sqrt{\frac{\pi\varphi}{3(Z_{eff} + 5)}} \left(1 - \bar{E} + \frac{4\pi(Z_{eff} + 1)^2}{3\varphi(Z_e ff + 5)(\bar{E}^2 + 4/\varphi^2 - 1)} \right)^{-1/2} \equiv S_s(n_r, \bar{E}), \tag{3}$$

$$\frac{1}{r}\frac{\partial}{\partial r}\left(r\frac{\partial E}{\partial r}\right) = \mu_0 \frac{\partial}{\partial t} j \tag{4}$$

$$j = \sigma_{sp} + ecn_r \tag{5}$$

where σ_{sp} is a Spitzer conductivity, n_{rp} and n_{rs} are the primary and secondary RE densities, $\bar{E} \equiv E/E_C$, and the critical electric field $E_C = n_e q_e^3 \ln\Lambda / 4\pi\epsilon_0^2 m_e c^2$, respectively. The total RE density n_r is evaluated from the sum of the primary (n_{rp}) and secondary (n_{rs}) REs. The generation rate of the primary RE, which is generated by Dreicer mechanism, is defined in eq. (2) as electrons go out from the momentum calculation domain: $0 < p < p_{max}$ and $p_{max}^2/m \sim 1$MeV. On the other hand, the generation rate of the secondary RE, which is generated by avalanche mechanism[5], is expressed as the function of n_r and $\bar{E} = E/E_C$ in eq. (3), where $\varphi = 1 - 1.46\varepsilon^{1/2} + 1.72\varepsilon$, $\varepsilon = r/R$ and $\tau_r = 4\pi\epsilon_0^2 m^2 c^3 / n_e q^4 \ln\Lambda$. Equation (4) expresses the electric field diffusion and this equation is closed by the Ohm's low (eq. (5)). Here, it is assumed that the current density consists of two components: the bulk current , $\sigma_{sp}E$, and the RE current, ecn_r. Here all of REs are assumed to travel with the velocity of light. The conductivity, σ_{sp}, and the collision coefficients ,$\overleftrightarrow{\boldsymbol{D}}_C$ and $\boldsymbol{F}_C$, require the background plasma temperature, therefore, the evolution of the plasma temperature is given as a function of time. Since the behavior of the plasma during thermal quench is too complex to describe accurately in RE generation time scale, here, the decay of the plasma temperature is modeled with the time constant of the thermal quench, τ_q:

$$T(t,\rho) = (T_0(\rho) - T_f(\rho)) \exp\left(-t/\tau_q\right) + T_f(\rho), \tag{6}$$

$$T_0(\rho) = (T_0(0) - T_0(1))(1-\rho^2)^2 + T_0(1), \tag{7}$$

$$T_f(\rho) = T_f(0)(1 - 0.9\rho^2), \tag{8}$$

where ρ denotes the normalized minor radius, T_0 and T_f are the initial and post-quench temperature, and τ_q is the time constant of the thermal quench time, respectively. Electrons and ions are assumed to have the same temperature.

Results In order to investigate the effect of the hot-tail, comparisons have been made for the results including and excluding the hot-tail effect. The results excluding the effect are obtained by the simulation which use the theoretical primary RE generation rate model[6] instead of eq. (2). Under the condition of the steady electric field and constant plasma temperature, the values of the primary RE generation rate calculated by these two models have good agreement.

We employed the ITER like plasma parameters, such as major radius $R = 6.2$m, minor radius $a = 2.0$m, initial plasma current $I_p = 15$MA, initial temperature $T_0(0) = 22.7$keV, $T_0(1) = 2.27$keV post-quench temperature $T_f(0) = 10$eV, and electron density $n_e(0) = 1 \times 10^{20}\mathrm{m}^{-3}$. The effective charge is assumed to be $Z_{eff} = 1$.

Figure 1 shows the relation of RE current including and excluding the hot-tail effect to the thermal quench time τ_q. Red and green curves denote the total and primary RE currents and solid and dotted

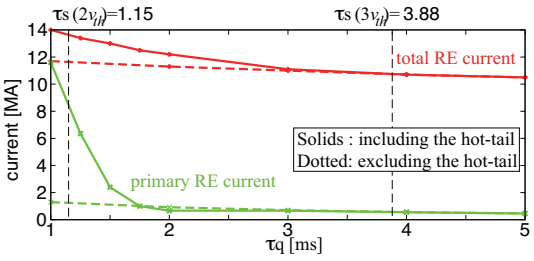

Figure 1: Generated primary and total RE currents against the thermal quench time.

curves denote RE currents including and excluding the hot-tail effect. Dashed vertical lines show the e-e slowing down time, $\tau_s^{ee}(v) = 2\pi\epsilon_0^2 m^2 v^3 / n_e q^4 \ln\Lambda$, calculated with the velocity $2v_{th}$ and $3v_{th}$, where v_{th} is the thermal velocity for the pre-quench temperature. From this figure, it is found that if the thermal quench time is shorter than $\tau_s^{ee}(2-3v_{th})$, the hot-tail effect enhances the total RE generation.

Figure 2 shows the primary and secondary RE current density profiles for $\tau_q = 1.5$ms and 4.0ms. For $\tau_q = 4.0$ms, which is slower than $\tau_s^{ee}(3v_{th})$, profiles between including and excluding the hot-tail effect have good agreement. In the contrary, for $\tau_q = 1.5$ms, the hot-tail effect changes RE current density profiles. The effect enhances the primary RE current density in the whole region. On the other hand, the secondary RE current density decreases in inner region ($\rho < 0.4$) and increases in outer region ($\rho > 0.4$). The decrease of the secondary RE in inner region comes from the reason that the increment of the primary RE current in inner region reduces the electric field. The increase of the secondary RE in outer region comes from the fact that the seed REs in the region increase slightly owing to the hot-tail effect. The increment of the seed RE does not affect the electric field because it is negligible in the view of the poloidal flux. As a consequence, the hot-tail effect make the RE current density profile broader even in the secondary RE dominant case.

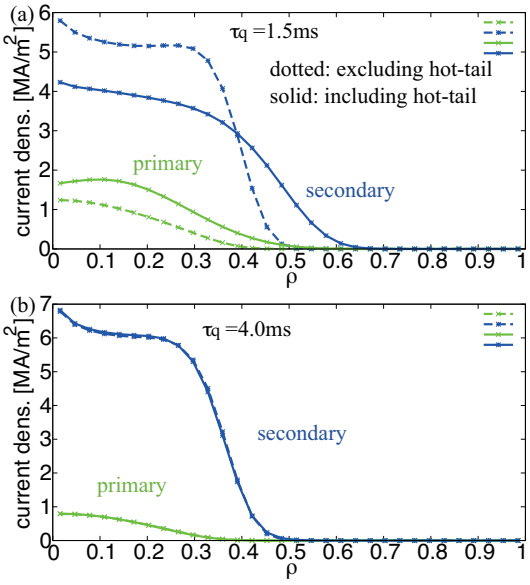

Figure 2: Primary and secondary RE current density profile for (a) $\tau_q = 1.5$ms and (b) 4.0ms.

Summary The present work has investigated the contribution of the hot-tail effect to the RE generation in ITER. Despite the fact that the RE generation is dominated by the secondary current in a high-current tokamak like ITER, our results shows that the RE current density profile is modified by the hot-tail effect. Since the small increment of the primary RE current is amplified by the avalanche effect, the final RE profile changes associated with the hot-tail generation.

[1] H. M. Smith and E. Verwichte, Phys. Plasmas, **15**, 072502, (2008).
[2] T. Fehér, *et. al.*, Plasma Phys. Control. Fusion, **53**, 035014, (2011).
[3] H. Nuga, A. Matsuyama, *et at.*, Plasma and Fusion Research, **10**, 1203006, (2015).
[4] C. F. F. Karney, Computer Physics Report, **4**, 183, (1986).
[5] M. N. Rosenbluth and S. V. Putvinski, Nuclear Fusion, **37**, 1355, (1997).
[6] J. W. Conner and R. J. Hastie, Nuclear Fusion, **15**, 415, (1975).

統合コード TASK による炉心プラズマ立ち上げシミュレーション
Burning plasma start-up simulation by the TASK code

永井一輝，福山淳，奴賀秀男
Kazuki Nagai, Atsushi Fukuyama, Hideo Nuga

京都大学大学院工学研究科
Graduate School of Engineering, Kyoto University

The start up of burning plasma has to be carried out within a limited external heating power. Therefore, it is important to analyze the behavior of fast fuel ions quantitatively and self-consistently. To simulate the start up of ITER burning plasma, a tool to analyze the time evolution of momentum distribution functions of fuel ions has been developed by using the core plasma integrated code TASK. In this report, we introduce the Legendre expansion in calculating the fusion reaction rate in order to reduce the computation time.

1 Introduction

In order to describe the behavior of burning plasmas, it is required to calculate the enhancement of the fusion reaction rate by the fast fuel ions produced by neutral beam injection or ion-cyclotron wave heating. High resolution in momentum space is required for correctly analyzing the wide energy range from 1keV to 3.5MeV. In order to improve the momentum resolution and the computational performance, TASK/FP is parallelized with respect to the minor radius, the momentum and the particle species. Since the quadruple integral over $p_a, p_b, \theta_a, \theta_b$ in the calculation of the fusion reaction rate requires a long computation time and a large memory, the reduction of necessary computational resource is required.

2 Calculation of fusion reaction rate

In order to calculate the fusion reaction rate, it is necesarry to integrate over the momentum space. For species a and b, we employ the momentum $\boldsymbol{p}_a$ and $\boldsymbol{p}_b$, the magnitude of momentum p_a and p_b, the pitch angle θ_a and θ_b, the momentum distribution function $f_a(p_a, \theta_a)$ and $f_b(p_b, \theta_b)$, the fusion reaction cross section σ_T and the particle relative velocity v'. The fusion reaction rate R is calculated as

$$\begin{aligned} R &= \iint f_a(\boldsymbol{p}_a) f_b(\boldsymbol{p}_b) \sigma_T v' \mathrm{d}\boldsymbol{p}_a \mathrm{d}\boldsymbol{p}_b \\ &= 4\pi^2 \iiiint f_a(p_a, \theta_a) f_b(p_b, \theta_b) \langle \sigma_T v' \rangle (p_a, p_b, \theta_a, \theta_b) p_a^2 p_b^2 \sin\theta_a \sin\theta_b \mathrm{d}p_a \mathrm{d}p_b \mathrm{d}\theta_a \mathrm{d}\theta_b, \end{aligned} \quad (1)$$

where $\langle \sigma_T v' \rangle (p_a, p_b, \theta_a, \theta_b)$ is $\sigma_T v'$ averaged over the gyro phase ϕ_a and ϕ_b. The calculation of (1) takes a long computation time due to the quadruple integration. In order to reduce the computation time, the momentum distribution function and $\langle \sigma_T v' \rangle$ were expanded using the Legendre polynomials $P_l(\cos\theta)$ such as

$$f(p, \theta) = \sum_{l=0}^{\infty} f_l(p) P_l(\cos\theta) \quad (2)$$

and

$$\langle \sigma_T(E) v' \rangle (p_a, p_b, \theta_a, \theta_b) = \sum_{l'=0}^{\infty} \sum_{k'=0}^{\infty} \langle \sigma_T(E) v' \rangle_{l'k'} (p_a, p_b) P_{l'}(\cos\theta_a) P_{k'}(\cos\theta_b) \quad (3)$$

where

$$f_l(p) = \frac{2l+1}{2} \int f(p,\theta) P_l(\cos\theta) \sin\theta \mathrm{d}\theta \tag{4}$$

and

$$\begin{aligned} &\langle \sigma_T(E) v' \rangle_{l'k'}(p_a, p_b) \\ &= \frac{2l'+1}{2} \frac{2k'+1}{2} \iint \langle \sigma_T(E) v' \rangle (p_a, p_b, \theta_a, \theta_b) P_{l'}(\cos\theta_a) P_{k'}(\cos\theta_b) \sin\theta_a \sin\theta_b \mathrm{d}\theta_a \mathrm{d}\theta_b. \end{aligned} \tag{5}$$

Using the orthogonality of the Legendre polynomials, the final form of fusion reaction rate is expressed as

$$R = 4\pi^2 \sum_l \sum_k \frac{2}{2l+1} \frac{2}{2k+1} \iint f_{al}(p_a) f_{bk}(p_b) \langle \sigma_T v' \rangle_{lk}(p_a, p_b) p_a^2 p_b^2 \mathrm{d}p_a \mathrm{d}p_b. \tag{6}$$

By reducing the number of Legendre polynomial, compared with number of pitch angle mesh, we can reduce the computational resource required.

3 Source and sink in the fusion reaction

The fusion products are assumed to be generated with the fusion reaction rate as isotropic in velocity space and mono-energy neglecting the kinetic energy of fuel ion. On the other hand, the sink term $S_a(p_a, \theta_a)$ of fuel ions a is given by

$$S_a(p_a, \theta_a) = -2\pi \iint \langle \sigma_T(E) v' \rangle (p_a, \theta_a, p_b, \theta_b) f_a(p_a, \theta_a) f_b(p_b, \theta_b) p_b^2 \sin\theta_b \mathrm{d}p_b \mathrm{d}\theta_b. \tag{7}$$

Using the Legendre polynomials, it can be expressed as

$$S_a(p_a, \theta_a) = -2\pi \sum_l P_l(\cos\theta_a) f_a(p_a, \cos\theta_a) \sum_k \left(\frac{2}{2k+1} \right) \int p_b^2 \langle \sigma_T(E) v' \rangle_{l,k}(p_a, p_b) f_k(p_b) \mathrm{d}p_b. \tag{8}$$

Since the double integral over p_b and θ_b is reduced to one-dimensional p_b integral, this calculation also requires less computational resource.

4 Benchmark test

We have compared the calculation of the fusion reaction rate with the original quadruple integral model and the present Legendre expansion model. Two patterns of benchmark test were carried out. One test was with the Maxwellian distribution function and the other includes neutral beam injection.

Table 1: The comparison of computation time

	Without Legendre expansion			With Legendre expansion		
NTHMAX	32	64	128	32	64	128
initial setup time[s]	0.790	2.870	11.660	0.750	2.800	10.720
time evolution : time[s]	12.200	25.510	120.550	10.590	19.680	62.170
DD fusion reaction rate[$\times 10^{-5}$]	6.0892	6.0855	6.0846	6.0941	6.0867	6.0849

In the test with Maxwellian distribution function, the initial parameters at the center are electron density $1.0 \times 10^{20}\mathrm{m}^{-3}$, deuterium ion density $0.5 \times 10^{20}\mathrm{m}^{-3}$, tritium ion density $0.5 \times 10^{20}\mathrm{m}^{-3}$ and temperature 20keV. Table 1 shows computation time without and with

Legendre expansion. NTHMAX is number of the pitch angle division. According to Table 1, when NTHMAX is large, the effect of speedup in calculation is observed.

Next, 1MeV deuterium NBI with beam power of 20MW is assumed. The initial parameters at the center are electron density $1.0\times10^{20}\mathrm{m}^{-3}$, deuterium ion density $0.45\times10^{20}\mathrm{m}^{-3}$, tritium ion density $0.45\times10^{20}\mathrm{m}^{-3}$, α particle density $0.05\times10^{20}\mathrm{m}^{-3}$ and temperature 20keV. Fig.1 shows the example of momentum distribution function with NBI. Table 2 shows computational

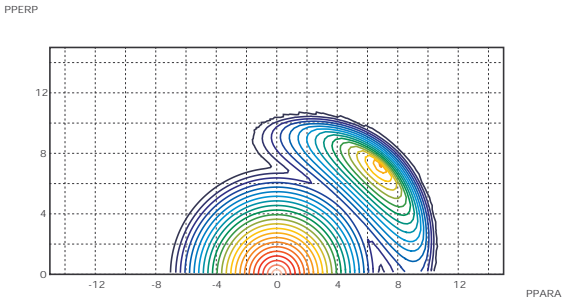

Fig. 1: Momentum distribution function

time without Legendre expansion, with Legendre expansion (maximum order of Legendre expansion L is 0) and with Legendre expansion (maximum order of Legendre expansion L is 4). According to Table 2, the computational time using Legendre expansion becomes less than half of the time without Legendre expansion for NTHMAX= 64. DT fusion reaction rate is calculated with sufficient accuracy.

Table 2: The comparison of calculation speed with the NBI

	Without Legendre expansion	With Legendre expansion (L=0)	With Legendre expansion (L=4)
initial setup time [s]	8.660	8.290	12.440
time evolution: time [s]	138.910	52.530	53.090
DT fusion reaction rate [$\times10^{-3}$]	8.5858	8.5875	8.5875

Therefore, by using the Legendre expansion, the fusion reaction rate is calculated much faster.

5 Summary and remaining issue

In order to analyze the time evolution in burning plasma start-up, it is required to describe time-evolution starting from around 2keV to around 20keV in temperature in the presence of additional heating (NBI, ICRF) and fusion reaction. In this situation, the kinetic transport analysis with the momentum distribution functions requires high resolution in momentum space in order to describe collisional relaxation between electrons and ions and between bulk and tail accurately. For such a large scale analysis, it is important to improve the computational performance of calculating the fusion reaction rate in addition to the non-linear collisional terms. In this study, we have shown that the calculation of source and sink terms in fusion reaction rate can be accelerated by the Legendre expansion.

The remaining issue is to use the TASK/FP analysis for the startup of ITER burning plasma and to compare with those of the analysis using 1D diffusive transport code TASK/TR.

Hydrogen Isotope trapped in tungsten vacancy

Kazuhito Ohsawa[1], Yuji Hatano[2], Masatake Yamaguchi[3]

[1]Research Institute for Applied Mechanics, Kyushu University
[2]Hydrogen Isotope Research Center, University of Toyama
[3]Center for Computational Science and e-system, Japan Atomic Energy Agency

1. Introduction

Divertor armor tiles installed in fusion reactors are exposed to the most intense plasma particle irradiation. So, it is planning that the divertor armor tiles are covered by tungsten (W) or its alloys because they are excellent properties as plasma facing materials (PFMs). For example, they have low hydrogen (H) solubility, high thermal conductivity, and high melting point. However, it is concerned that a large amount of H isotopes, deuterium (D) and tritium (T), are retained in the W materials in the irradiation circumstance. In particular, tritium retention of the PFMs is very serious safety concerns because T is a radioisotope whose physical half-life is 12 years.

Usually, H isotopes are not retained in bulk W because H dissolution in W is considerable endothermic reaction. However, it is expected that vacancy type lattice defects are nucleated by the plasma particle irradiation and H isotopes can be accommodated in the defects. In the present work, we focus on the H isotopes trapped in W mono-vacancy. The binding energy between H isotopes and W mono-vacancy is estimated by first-principle calculations on the basis of density functional theory. The zero point energy of H isotope depends on the mass number. The binding energy of lighter H isotope to a mono-vacancy is larger than that of heavier one by taking into account the zero point energy. We calculate the amount of vacancy-hydrogen (V-H) cluster to perform a quantitative analysis to estimate H isotopes trapped in the V-H clusters in terms of a thermodynamic model assuming thermal equilibrium.

2. Methodology

First-principle calculations are performed using Vienna ab initio simulation package (VASP). Binding energy e_k^a of hydrogen isotope ${}^a\mathrm{H}$ to a W mono-vacancy where a indicates mass number of hydrogen isotope (a=1,2,3) is defined , as follows.

$$e_k^a = \mathrm{E}\left[\mathrm{W}_{n-1}\mathrm{V}\right] - \mathrm{E}\left[\mathrm{W}_{n-1}\mathrm{V}\,{}^a\mathrm{H}_k\right] - \mathrm{Z}[{}^a\mathrm{H}^{\mathrm{V}}{}_k] - k\left(\mathrm{E}\left[\mathrm{W}_n\right] - \mathrm{E}\left[\mathrm{W}_n\,{}^a\mathrm{H}^{\mathrm{T}}\right] - \mathrm{Z}[{}^a\mathrm{H}^{\mathrm{T}}]\right) \quad (1)$$

The function E is the cohesive energy of the supercell and Z is zero point energy of hydrogen isotopes ${}^a\mathrm{H}$. V represents a W mono-vacancy. For example, $\mathrm{W}_{n-1}\mathrm{V}^a\mathrm{H}_k$ indicates a supercell composed of n-1 W, a vacancy V, and k ^{a}H. $\mathrm{Z}[{}^a\mathrm{H}^{\mathrm{V}}{}_k]$ is the total zero point energy of k ^{a}H trapped in the vacancy. $\mathrm{W}_n{}^a\mathrm{H}^{\mathrm{T}}$ means a solute ^{a}H in bulk W at T site and $\mathrm{Z}[{}^a\mathrm{H}^{\mathrm{T}}]$ is the zero point energy of the ${}^a\mathrm{H}^{\mathrm{T}}$. We use a large simulation cell, $6\times6\times6$ bcc lattice i.e. n=432 to calculate vibrational entropy, as mentioned later.

V-H cluster concentrations are calculated in an equilibrium thermodynamic model. Helmholtz free energy is

$$F = U - TS \qquad (2)$$

The internal energy is expressed as

$$U = Ne_v - \sum_{ij} n_{ij} e_{ij} \ , \qquad (3)$$

where e_v is empty vacancy formation energy. n_{ij} is the number of V-H clusters composed of two types of hydrogen isotopes, $V^aH_i{}^bH_j$. The binding energy e_{ij} is assumed to be a weighted average, where e_k^a and e_k^b are defined in eq. (1).

$$e_{ij} = \left(ie_{i+j}^a + je_{i+j}^b\right)/\left(i+j\right) \qquad (4)$$

N is the total number of the V-H clusters. Entropy is composed of two terms, configurational and vibrational entropy.

$$S = S^{con} + S^{vib} \qquad (5)$$

The configurational entropy is derived from Boltzmann equation.

$$S^{con} = k_B \ln \Omega \, , \qquad (6)$$

where Ω is the number of possible arrangement of V-H clusters and solute H isotopes distributed over the T site in bcc W lattice. The vibrational entropy is described in the lattice vibration ratio in high temperature approximation

$$S^{vib} = k_B \sum_k n_k \ln P_k \qquad P_k = \prod_i \nu_i / \nu'_{ki} \ , \qquad (7)$$

where ν_i and ν'_{ki} are vibration mode of perfect lattice and i-th nearest neighbor atom in the vicinity of V-H cluster VH_k..

We investigate H isotope trapping in two kinds of model. (Model I) The total number of vacancies, N, in bulk W is assumed to be constant. Therefore, the vacancies are introduced by plasma particle collision. (Model II) The vacancy formation energy is considerably reduced by H presence, i.e. superabundant vacancy formation induced by H isotopes is taken into account. The number of each V-H cluster n_{ij} is determined by minimization of the free energy in eq. (2) in the thermodynamic model.

3. Results

Figure 1 indicates binding energies of H isotopes e_k^a to a W vacancy in eq. (1). The formation energy for an empty vacancy e_v is estimated to be 3.028 eV. As mentioned before, binding energy of lighter H isotopes is larger than that of heavier one. According to Fig.1, vacancy formation energy is quite reduced by hydrogen trapping. If the number of H atoms is more than three, the V-H cluster formation energy become negative, that is, the V-H clusters are spontaneously nucleated in the present thermodynamic model.

Figure 2 shows the total amount of H isotopes trapped in W vacancies in the case of model I, where the total number of vacancies is assumed to be constant. As an example, the vacancy concentration, i.e., number ratio of vacancy and W atom, is assumed to be 1×10^{-5}. Each H isotope initially induced in the bulk W is 5×10^{-4}.

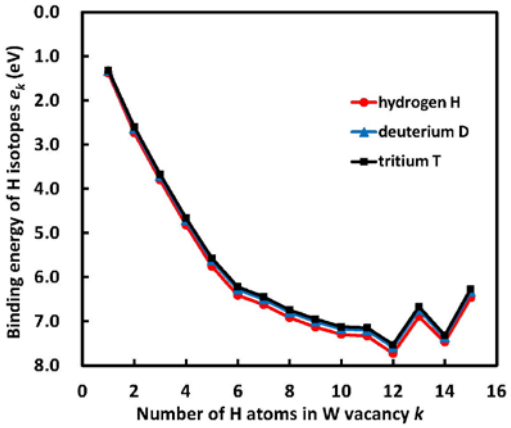

Fig. 1: Binding energy of H isotopes (H, D, T) to a W mono-vacancy.

Figure 3 indicates the concentrations of V-H cluster as a function of bulk H concentration and temperature in the case of model II. In the limit of low H concentration, the V-H cluster concentration at a given temperature is usual thermal vacancy one. However, the V-H clusters rapidly increase when the bulk H concentration exceeds a threshold value. It is possible to be accommodated more than six H atoms in a W vacancy. However, the majority of V-H cluster is VH_6 in a wide range of temperature and bulk H concentration.

4. Discussion

Figure 2 suggests that the amount of lighter H isotope trapped in W vacancies is more than that of heavier one, which reflects the binding energy difference, as shown in Fig. 1. This effect will be useful to remove or reduce tritium retained in the FPMs installed in fusion reactors.

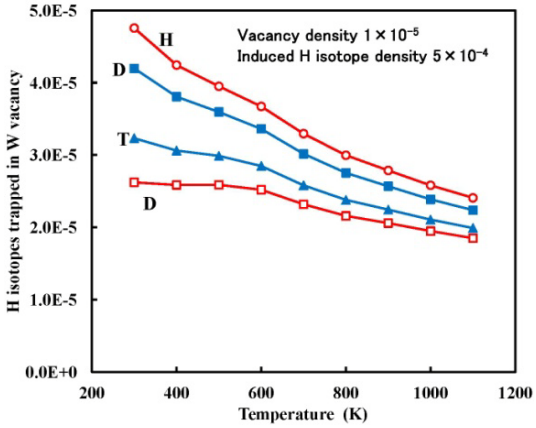

Fig. 2: Total amount of H isotopes trapped in W vacancies in finite temperature. Red and blue lines correspond to H-D and D-T combination, respectively.

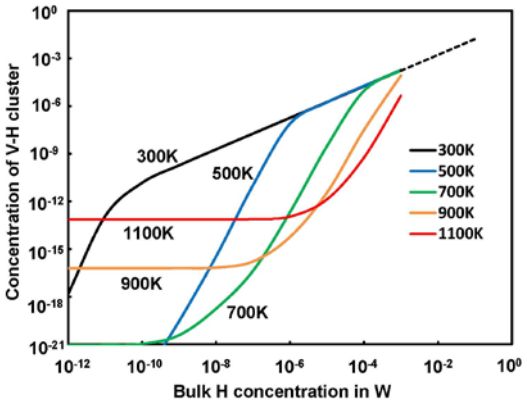

Fig. 3: Dependence of V-H cluster concentration on bulk H concentration in finite temperatures.

References

K. Ohsawa, F. Nakamori, Y. Hatano, M. Yamaguchi, J. Nucl. Mat. **458** (2015) 187.

Eigenmode analysis of geodesic acoustic modes driven by fast ions in the limit of high safety factor

M. Sasaki[1,2], N. Kasuya[1,2], K. Hallatschek[2,3], K. Itoh[2,4], Y. Kosuga[2,5], M. Lesur[6] and S.-I. Itoh[1,2]

[1]*Research Institute for Applied Mechanics, Kyushu University, Kasuga 816-8580, Japan*
[2]*Research Center for Plasma Turbulence, Kyushu University, Kasuga 816-8580, Japan*
[3]*Centre for Interdisciplinary Plasma Science, Max-Planck Institut fur Plasmaphysik, EURATOM-IPP Association, D-85748 Garching, Germany*
[4]*National Institute for Fusion Science, Toki 509-5292, Japan*
[5]*Institute for Advanced Study, Kyushu University, Fukuoka 812-8581, Japan*
[6]*Lorraine University, Institut Jean Lamour 54-506, France*

Here we report a new mechanism of excitation of geodesic acoustic modes (GAMs) in the presence of fast ions in the limit of high safety factor. Resonance to the magnetic drift of fast ions gives an unstable branch of GAMs driven by fast ions. One of the prominent characteristics of the mode is its spatial structure, which has a steep poloidal gradient. The associated large wavenumber can cause effective ion heating mediated by the energy transfer from the GAMs.

Importance of geodesic acoustic modes driven by energetic particles (EPs), E-GAMs, [1] has been recognized in the study of magnetic confined plasmas. A gyrokinetic simulation has shown that the E-GAMs couple with turbulence so that it may be possible to control turbulent transport by EPs [2]. GAMs transfer their energy to bulk ions through dissipation such as Landau damping, and the energy channeling from EPs to bulk ions via GAMs has been proposed as GAM channeling [3]. Actually, E-GAM have been observed in experiments [4], and several branches of GAMs have been found [5]. Identification of each branch of E-GAMs is required.

In this study, the eigenmode analysis of E-GAMs is performed based on the gyrokinetic equation in the limit of high safety factor. We show there are several branches of GAMs in the presence of EPs. In accordance with the energy of EPs, the resonance between particles motion and the GAMs changes so that a new branch appears. Here, we report a new branch of E-GAM.

The plasma configuration under consideration is a high aspect ratio tokamak with a circular cross section. The linearized gyrokinetic equation for the non-adiabatic response of the ion velocity distribution to a GAM oscillation is solved in the limit of high safety factor. The response function of the EPs has two kinds of resonances; (i): the resonance due to the transit frequency, and that due to the drift frequency. In the limit of high safety factor, the resonance due to the drift frequency becomes dominant, and a new branch with a frequency close to the drift frequency of the fast ions appears. In this case, the poloidal side band coupling is strong. The poloidal mode expansion cannot be used, so that the eigenfunction is treated as a function of the poloidal angle. The poloidal eigenfunction of the unstable branch, which is related to the electrostatic potential fluctuation, is shown in Fig. 1. The real part of the eigenfunction has bumps where the resonance of the magnetic drift with the wave is strong. The imaginary part of the eigenfunction becomes important near the resonance positions, indicating the particles and associated energy transfer. The effective wavenumber parallel to the magnetic field, which is evaluated from the poloidal angle derivative, increases due to the bumps, and the effect of ion heating through Landau damping becomes large.

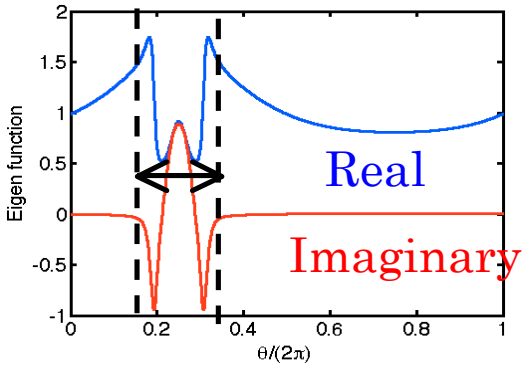

Fig.1. Poloidal eigenfunction of the new branch

[1] G. Y. Fu, Phys. Rev. Lett., 101, 185002 (2008).
[2] D. Zarzoso, et. al., Phys. Rev. Lett., 110, 125002 (2013).
[3] M. Sasaki, et. al., Plasma Phys. Control. Fusion, 53, 085017 (2011).
[4] R. Nazikian, et. al., Phys. Rev. Lett., 101, 185001 (2008).
[5] T. Ido, et. al., IAEA Fusion Energy Conference, PD/P8-16 (2012).

Analysis of triplet term in parallel momentum flux

Y. Kosuga[1,2], S.-I. Itoh[2,3], P.H. Diamond[4], K. Itoh[5,3]

[1] Institute for Advanced Study, Kyushu University, Fukuoka, Japan
[2] Research Institute for Applied Mechanics, Kyushu University, Fukuoka, Japan
[3] Research Center for Plasma Turbulence, Kyushu University, Fukuoka, Japan
[4] University of California, San Diego, USA
[5] National Institute for Fusion Science, Gifu, Japan

Transport of the momentum along the magnetic field (or shortly, parallel momentum transport) is an important issue for magnetic fusion. In fusion plasmas, these parallel flows (or approximately toroidal flows) can stabilize harmful MHD instability and control transport by contributing to the $E \times B$ shear. While parallel flows are externally driven by NBI, recent research has revealed the intrinsic property of magnetized plasmas to drive parallel flows intrinsically[1,2]. Namely, parallel flows are generated in the absence of appearant momentum source, such as in RF heated plasmas. In these cases, it is often thought that the flows are driven by turbulence. Direct measurement of parallel momentum flux has been performed, and the role of turbulence in driving flows have been confirmed[3].

A recent development of the problem of parallel momentum transport is the observation of the triplet correlation in the total momentum flux. The total momentum flux is given by

$$\Pi_{xz} = \langle n \rangle \langle \tilde{v}_x \tilde{v}_z \rangle + \langle v_z \rangle \langle \tilde{v}_x \tilde{n} \rangle + \langle \tilde{n} \tilde{v}_x \tilde{v}_z \rangle \tag{1}$$

Here, x is the radial direction and z denotes the direction of the magnetic field. The first term is Reynolds stress, the second term is convective term, and the last term is the nonlinear flux. Recent measurement on the linear device PANTA confirm the contribution from the triplet term[4]. The triplet term can be a major part of the total momentum flux, as reported from the TORPEX experiment[5]. Then it is an important issue to analyze this term and clarify the parameter dependence, in order to asses it impact on different plasmas.

From modeling perspective, the triplet flux requires the closure calculation. In a recent work[6], the triplet was calculated for the case of strong turbulence, where blobs are a major player in the turbulent fluctuation. On the other hand, turbulence often contains waves, as indicated by the sharp peaks in the frequency spectrum. In this case, we need to address the role of waves in driving the triplet flux[7]. In this case, the necessary phase is for producing the triplet flux is set by the wave resonance, rather than by the nonlinear decorrelation. As a result, since drift waves are dispersive, we would expect that the class of triads that satisfy the frequency resonance condition is very limited. We can identify triads that contribute to the nonlinear flux dominantly. We later discuss this in more detail.

In order to calculate the triplet flux, we use Hasegawa-Mima equation with parallel flow coupling. Within the model, we focus on the wave momentum density,

$$\langle \tilde{q} \tilde{v}_\parallel \rangle \sim k_\parallel (1 + k_\perp^2) |\hat{\phi}_{\mathbf{k}}|^2 / \omega_{\mathbf{k}} \equiv P_{\mathbf{k}\parallel} \tag{2}$$

Here we used normalized quantities. The space is normalized by ρ_s, the time is normalized by ω_{ci}, and the potential is normalized by e/T_e. $q = (1 - \nabla_\perp^2 \phi)$. Note that $\mathcal{E}_{\mathbf{k}} =$

$(1+k_\perp^2)|\hat{\phi}_{\mathbf{k}}|^2$ is the energy density of drift waves. So $P_{\mathbf{k}\parallel} = \mathcal{E}_{\mathbf{k}}/(\omega_{\mathbf{k}}/k_\parallel)$ is a momentum density in the parallel direction. This may be understood from the particle mechanics, where momentum p is obtained by dividing energy by velocity, $p = E/v$. Note that the sign of the $P_{\mathbf{k}\parallel}$ is set by the symmetry breaking in the parallel direction of drift waves. This can be provided from several processes, including the intensity gradient, radial electric field shear, etc.

The wave momentum density can be spatially transported. One way is due to the wave propagation. In this case, the flux is given by $v_{gr}P_{\mathbf{k}\parallel}$, where v_{gr} is the group velocity of drift waves. Typically $v_{gr} > 0$ for drift waves, due to the out-going wave boundary condition. The flux of wave momentum by the drift wave propagation exert residual stress and drive parallel flows.

In addition to the linear propagation, the momentum density can be spatially scattered by turbulence and can spread. This effect may be captured by the nonlinear, triplet contribution $\langle \tilde{v}_x \tilde{q} \tilde{v}_\parallel \rangle$. A closure calculation is necessary to calculate this term. By employing the two scale direct interaction approximation, we can calculate the nonlinear flux as:

$$\langle \tilde{v}_x \tilde{q} \tilde{v}_\parallel \rangle = \sum_{\mathbf{k_1}} (-D_{\mathbf{k_1}} \partial_x P_{\mathbf{k_1}\parallel} + V_{\mathbf{k_1}} P_{\mathbf{k_1}\parallel}) \tag{3}$$

Here $D_{\mathbf{k_1}}$ is the scale dependent diffusivity and $V_{\mathbf{k_1}}$ is the scale dependent convective velocity. They are defined as

$$D_{\mathbf{k_1}} = \sum_{\mathbf{k_2}} \theta_{\mathbf{k_1},\mathbf{k_2}} |\hat{\phi}_{\mathbf{k_2}}|^2 F_1(\mathbf{k_1}, \mathbf{k_2}) \tag{4}$$

$$V_{\mathbf{k_1}} = \sum_{\mathbf{k_2}} \theta_{\mathbf{k_1},\mathbf{k_2}} \partial_x |\hat{\phi}_{\mathbf{k_2}}|^2 F_2(\mathbf{k_1}, \mathbf{k_2}) \tag{5}$$

Here $\theta_{\mathbf{k_1},\mathbf{k_2}} \cong \pi\delta(\omega_{\mathbf{k_1}+\mathbf{k_2}} - \omega_{\mathbf{k_1}} - \omega_{\mathbf{k_2}})$ is the triad interaction time. F_1 and F_2 are coupling coefficients between $\mathbf{k}_1$ and $\mathbf{k}_2$. As an estimate, if we use gyro-Bohm like diffusivity and the convective velocity, we find that

$$\langle \tilde{v}_x \tilde{q} \tilde{v}_\parallel \rangle \sim -v_* \frac{\rho_s}{L_I} k_\parallel N_{\mathbf{k}} \tag{6}$$

Here L_I is the intensity gradient and the sign convention is such that when the fluctuation intensity increases toward the edge ($L_I > 0$) the flux is toward the core.

From the approximated form, we find that the flux becomes important around region with steep intensity gradient. For example, the nonlinear flux is important in the region with transport barriers, since across the barrier the fluctuation intensity varies dramatically. So the triplet flux is important to understand the generation of flows in such regions.

We acknowledge useful discussion with Drs. S. Inagaki, T. Kobayashi, L. Wang, and Z. Guo. This work was supported by Grants-in-Aid for Scientific Research of JSPF of Japan (23244113, 15H02155, 15K17799), Kyushu University Interdisciplinary Programs in Education and Projects in Research Development (TT26705).

References

[1] P.H. Diamond, et al., Nucl. Fusion **53** 104019 (2013)

[2] K. Ida and J.E. Rice, et al., Nucl. Fusion **54** 045001 (2014)

[3] Y. Xu, et al., Nucl. Fusion **53** 072001 (2013)

[4] S. Inagaki, et al., submitted to Sci. Rep. (2016)

[5] B. Labit, et al., Phys. Plasmas **18** 032308 (2011)

[6] L. Wang, et al., Phys. Plasmas **22** 052302 (2015)

[7] Y. Kosuga, et al., in preparation (2016)

Transport analysis of impurity LHD peripheral regions during neon gas-puff

Gakushi Kawamura, Masahiro Kobayashi, Shuyu Dai, Kiyofumi Mukai,
Ryuichi Sano, Shwetang N. Pandya[1], Byron Peterson, Yuhe Feng[2],
and the LHD Experiment Group

National Institute for Fusion Science, 322-6 Oroshi-cho Toki, Gifu 509-5292, Japan
[1] Institute for Plasma Research, India
[2] Max-Planck-Institut für Plasmaphysik, Greifswald Germany

Transport analysis of neon seeded by gas puff was carried out. LHD discharge #117478 was simulated by EMC3-EIRENE code and radial distribution of plasma measured by Thomson scattering was reproduced. The results suggest that neon accumulates more than carbon because it has deeper penetration of neutral particles and accesses to the region where thermal force is dominant. The transport of neon ions along a magnetic field line was strongly affected by the force balance between friction and thermal force. The friction force determined by the plasma flow speed can be enhanced by locally strong of magnetic flux density similar to a magnetic nozzle. The simulation suggests that helical ripple can enhance impurity screening.

Heat load on divertor plates is one of critical issues in a fusion device and a future reactor. Methods of power reduction such and advanced divertor concepts, impurity seeding, detachment are proposed and actively studied. Impurity gas puff is one of possible methods and has been investigated experimentally in LHD [1]. Direct measurement of impurity transport in the plasma is difficult and thus transport modeling with a simulation code is necessary to understand it. We have developed transport model of plasma, impurity and neutral particles in the peripheral plasma by using EMC3-EIRENE [2,3] and applied to LHD [4-6]. The code solves fluid equation with Monte-Carlo technique and has the capability of resolving perpendicular transport across a magnetic field line in 3D space. We modeled a 1/20 toroidal block of the LHD plasma, which consists of plasma and vacuum regions and they cover every cross section of the vacuum vessel. The plasma mesh system of EMC3 covers the peripheral plasma which has long connection length, roughly >10m. The core region is excluded from the simulation and modeled as boundary conditions at the last closed flux surface (LCFS). The magnetic axis is located at R_{ax}=3.6m and the vacuum field, i.e., zero beta value, is employed to make the calculation mesh.

We analyzed a LHD discharge with neon gas puff by EMC3-EIRENE. Input parameters were based on the discharge #117478 (17th cycle, 2013) and determined to reproduce radial distribution of plasma (see Fig. 1): input power P_{in}=11.6MW, electron density at core-SOL boundary $n_e=3.3\times10^{19}/m^3$, perpendicular transport coefficients $D=D_{imp}=1.0$ m^2/s and $\chi_e=\chi_i=0.4$ m^2/s. The duration time of the gas puff is approximately 100ms and small increase of electron density, 10~20%, and large increase of radiation, approximately twice, were observed. The plasma become steady state after short transition time and the enhanced radiation continued until the end of the discharge. That fact indicates that some amount of neon gas was confined in

the device and recycled through ionization and surface recombination in steady state. Therefore we modeled the neon as no gas puff but surface source on the divertor plates and no wall loss in EMC3-EIRENE code. The amount of neon is determined to have the same amount of total radiation as that measured by bolometer, 2.5MW. We simulate carbon and neon, which have 0.24MW and 1.4MW radiation, respectively, and the remaining 0.86 MW radiation is from hydrogen.

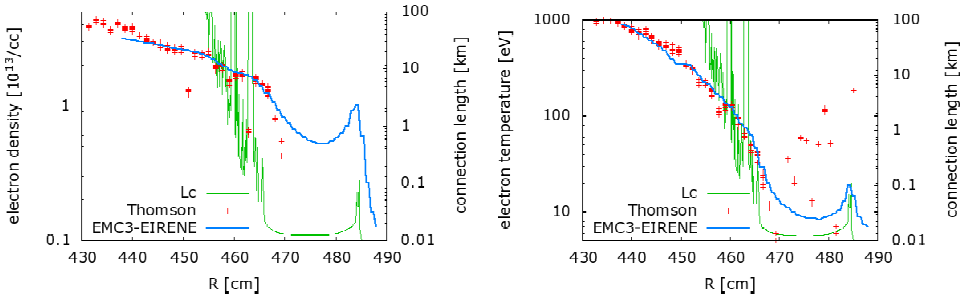

Fig. 1: Comparison of electron density and temperature between Thomson scattering (red dots) and EMC3-EIRENE (blue lines). The green lines represent the distribution of connection length.

We compared distribution of density and radiation of carbon and neon and found that much neon accumulate in the ergodic region than carbon, see Fig. 2(a). The physical reason of it can be understood from neutral transport and force acting on ions. Neon has higher ionization energy and deeper penetration into the plasma. The penetration limit is drawn in Fig 2 (a) as white lines. Carbon has high density outside the limit, e.g. left side of the white line, and neon has mainly inside the limit. This limit is determined by the distribution of electron temperature. Figure 2(b) shows distribution of force balance on impurity ions. Positive value (red) means friction force dominant and negative value (blue) means thermal force dominant. Friction force pushes ions toward downstream and thermal force is opposite. Two black lines are the penetration limit of neutral particles. Neon has deeper penetration and can access to the thermal force dominant region and therefore neon is transported toward upstream more easily than carbon. That is the reason of larger accumulation in the ergodic region.

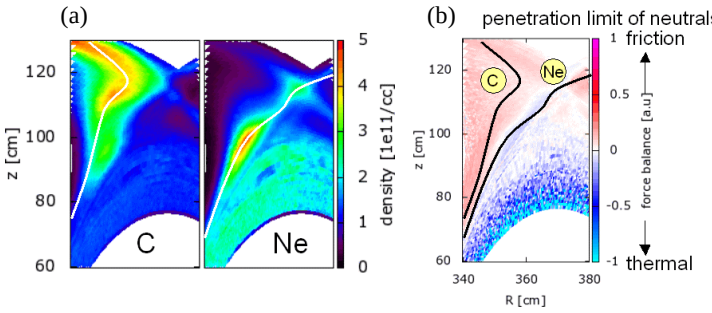

Fig. 2: distributions of (a) C and Ne density and (b) force balance on impurity ions. The white and black lines in the both figures represent penetration limit of neutral impurity particles.

Helical plasma has complicated structure of magnetic field lines and impurity transport is also complicated in space. Figure 3 shows density distribution of neon ions along a magnetic field line. The field tracing was carried out from the density peak in Fig. 2(a) toward the both directions, e.g. positive and negative. Thermal force is dominant in field line except near the

divertor plates, where fast plasma flow exists because of collisional presheath. The neon ionized in the divertor plasma experiences successive ionization to higher states and transported toward the upstream. In the middle of the field line, flow speed of impurity becomes zero and causes a large peak. Ions flow from the both side and escape from the field line due to perpendicular transport. Another field line has large area where friction force is dominant. Such area plays a role of barrier of impurity transport, see Fig. 4. The plasma flow speed is essential factor for friction force and affected by distribution of magnetic flux density. Helical plasma has periodical change of the magnetic flux density, e.g. helical ripple. We confirm that the ripple plays a role of magnetic nozzle and causes locally enhanced flow speed. That causes locally large friction force and pushes impurity ions toward the downstream. It can contribute to impurity screening.

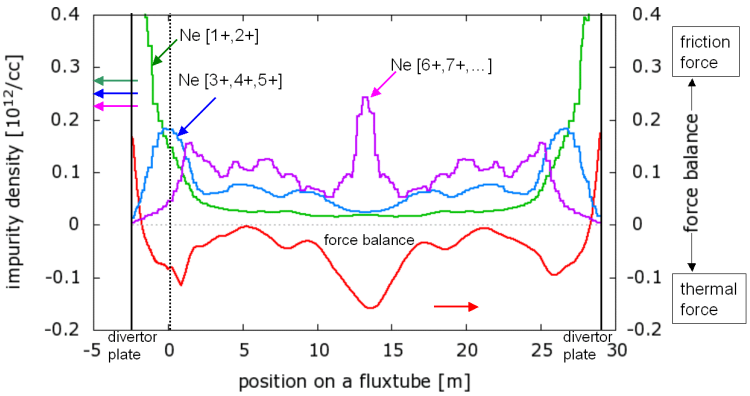

Fig. 3: distributions of neon density with three charge-state groups (green, blue and magenta lines) and force balance (red line) along a magnetic field line.

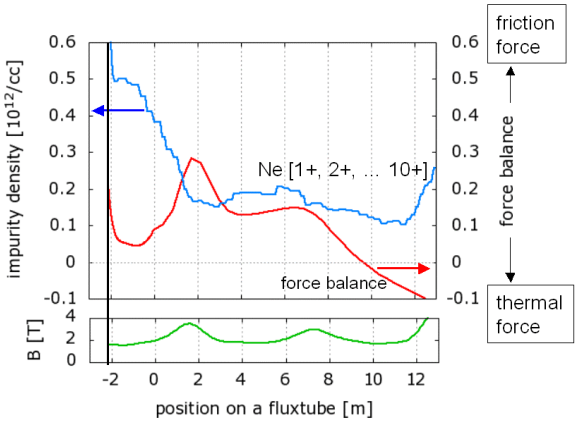

Fig. 4: distributions of neon density of all charge states (blue line), force balance (red line) and magnetic flux density (green line). The distribution of magnetic flux density and force balance has a strong correlation.

References

[1] K. Mukai et al., Nucl. Fusion 55 (2015) 083016
[2] Y. Feng et al., Contrib. Plasma Phys. 44 (2004) 57.
[3] D. Reiter et al., Nucl. Fusion 47 (2005) 172.
[4] G. Kawamura, et al., Contrib. Plasma Phys. 54 (2014) 437.
[5] M. Kobayashi, et al., Fusion Sci. Technol. 58 (2010) 220.
[6] M. Kobayashi et al., Nucl. Fusion 53 (2013) 033011.

Bohm Criterion and Virtual Divertor Model for SOL-Divertor Simulation

T. Takizuka[1], S. Togo[2], S. Azuma[3], A. Fukuyama[3]

[1] Graduate School of Engineering, Osaka University
[2] Graduate School of Frontier Sciences, University of Tokyo
[3] Graduate School of Engineering, Kyoto University

Bohm criterion, $V_f \geq C_s$ (V_f: plasma flow speed at the sheath entrance, C_s: sound speed), has been derived from the sheath formation condition. When the Bohm criterion is analyzed for two-ion-species plasma, two branches of the criterion are derived. Numerical experiments with PARASOL, however, give always the upper branch but never the lower branch. Introducing a linear stability analysis, it is found that the upper branch is stable but the lower branch unstable. Also found that the Bohm criterion is not directly related with the sheath formation condition. Generalized fluid model with anisotropic ion temperature for SOL-divertor simulation does not require a down-stream boundary condition on V_f at the divertor plate. For this sake, a virtual divertor model has been developed. Simulations with a new code demonstrate that V_f at the divertor plate exceeds C_s automatically without using the boundary condition of Bohm criterion.

1. Introduction

Bohm criterion is well known as a boundary condition for the plasma flow speed V_f at the sheath entrance in front of a plasma facing material. A simple criterion, $V_f \geq C_s$ (C_s: sound speed), is given from a condition that the solution to Poisson's equation for the sheath potential is not an oscillating profile but a monotonic profile [1]. From the plasma fluid equations, a linear response of the electron density n_e to the sheath potential ϕ is derived as $\delta n_e/n_0 = e\,\delta\phi/T_e \equiv \Phi$ and that of ion density n_i as $\delta n_i/n_0 = \Phi\{T_e/(m_i V_f^2 - \gamma_a T_i)\}$, where γ_a is the adiabatic index. The Poisson's equation is then described by $d^2\Phi/dx^2 = \kappa^2\Phi = (1/\lambda_D^2)\{1 - T_e/(m_i V_f^2 - \gamma_a T_i)\}\Phi$, where λ_D is the Debye length. For the monotonic profile of $\Phi \sim \exp(\kappa x)$ with $\kappa^2 \geq 0$, the condition $m_i V_f^2 \geq T_e + \gamma_a T_i$ is required. This elementary theory on the sheath formation has been believed as a base of the Bohm criterion.

Applying the above analytical method, the Bohm criterion for two-ion-species plasma was investigated [2]. The analysis gives two curves like a shifted hyperbola in a (V_1, V_2) diagram. On an upper branch, $V_1 > C_{s1}$ and $V_2 > C_{s2}$, while on a lower branch $V_1 < C_{s1}$ and $V_2 < C_{s2}$, where V_j and C_{sj} are the flow speed at the sheath entrance and a specific sound speed for species-j ion (j = 1, 2), respectively. Analytical results were compared with PARASOL simulation results [2]. The PARASOL simulation showed that V_1 and V_2 are always located near the upper branch. The study in Ref. [2] is briefly reviewed in the next section.

In order to solve the reason why the lower-branch solution is absent, we have introduced a linear stability analysis to the sheath theory. We found that the upper branch is stable but the lower branch unstable [3,4]. This is because the upper branch is realized but the lower branch does never appear in the PARASOL simulation. This stability analysis in Ref. [3,4] is shown in Section 3.

Recently we have developed a new code for SOL-divertor simulation with a generalized plasma fluid model taking account of anisotropic ion temperatures [5,6]. The momentum transport equation is described by a spatially 1st-order differential equation without the 2nd-order viscosity term. This equation does not especially require a boundary condition at the divertor plate. In order to simulate the existence of the divertor plate, we have introduced a virtual divertor (VD) model [5,6]. Simulation results with our new code demonstrated that the flow speed, V_f, at the divertor plate exceeds the sound speed, C_s, automatically. The criterion $V_f \geq C_s$ is required for the temporal-stability condition at the plasma boundary. When $V_f < C_s$, V_f is temporally increased up to C_s until the stability condition is satisfied. The topics of the VD model and Bohm criterion are presented in Section 4.

2. Bohm criterion for two-ion-species plasma

The Bohm criterion for two-ion-species plasma was investigated [2]. Basic equations in the analysis are; momentum balance equation, $\partial n_e T_e/\partial x = e\,\partial\phi/\partial x$, for electron, and equation of continuity, $\partial n_j V_j/\partial x = 0$, and momentum balance equation, $\partial/\partial x\,(n_j m_j V_j^2 + n_j T_j) = -e\,\partial\phi/\partial x$, for species-j ion. Linear responses of n_e, n_1 and n_2 to ϕ are derived as $\delta n_e/n_0 = \Phi$, $\delta n_1/n_0 = F_1\Phi \times \{T_e/(m_1V_1^2 - \gamma_a T_1)\}$ and $\delta n_2/n_0 = F_2\Phi\{T_e/(m_2V_2^2 - \gamma_a T_2)\}$, where $F_j = n_{0j}/n_0$ is the density fraction of species-j ion and $F_1 + F_2 = 1$. Poisson's equation is given by $d^2\Phi/dx^2 = \kappa^2\Phi = (1/\lambda_D^2)\{1 - T_e/(m_1V_1^2 - \gamma_a T_1) - T_e/(m_2V_2^2 - \gamma_a T_2)\}\Phi$. The monotonic sheath of $\Phi \sim \exp(\kappa x)$ can be formed when $\kappa^2 \geq 0$. This condition is rewritten as

$$(V_1^2 - C_{s1}^2)(V_2^2 - C_{s2}^2) \geq F_1F_2T_e^2/m_1m_2\,, \qquad (1)$$

where $C_{s1}^2 = (F_jT_e + \gamma_a T_j)/m_j$ is the specific sound speed for species-j ion. Condition (1) is satisfied inside blue regions in the (V_1, V_2) diagram shown in Fig. 1. On an upper branch, $V_1 > C_{s1}$ and $V_2 > C_{s2}$, while on a lower branch $V_1 < C_{s1}$ and $V_2 < C_{s2}$. This analytical result was compared with the 1D PARASOL simulation results for various mass ratio m_2/m_1, collisionality $L_{//}/l_{mfp}$ etc. Figure 2 shows results of a numerical experiment using PARASOL code [7]; m_2/m_1, = 4 and $L_{//}/l_{mfp} = 0.01$. The flow speeds, V_1 (red line) and V_2 (blue line) at the sheath entrance are measured. It was found from the PARASOL simulation that V_1 and V_2 are located near the upper branch as plotted in Fig. 3 by a cross (×),

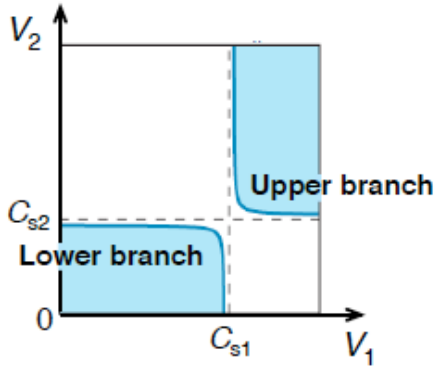

Fig. 1 Regions satisfying Condition (1) in (V_1, V_2) diagram for flow speeds at the sheath entrance for two-ion-species plasma.

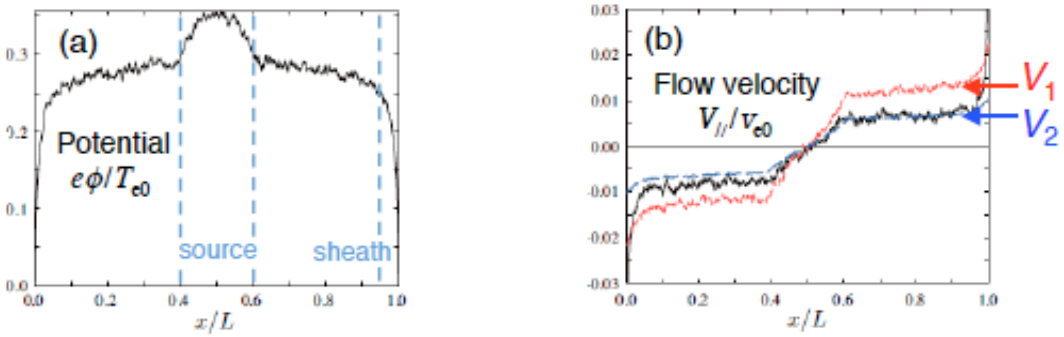

Fig. 2 Profiles of two-ion-species SOL plasma in a 1D PARASOL simulation, (a) potential ϕ and (b) flow velocity $V_{//}$ parallel to magnetic field. The hot-particle source is given in the central SOL region, and the sheath is formed in front of the divertor plate.

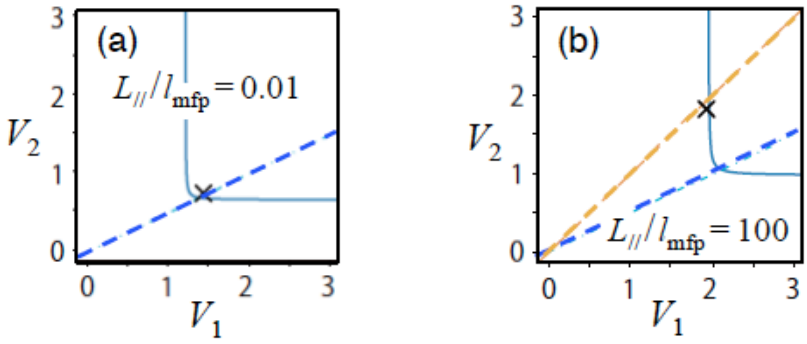

Fig. 3 Flow speeds at the sheath entrance, V_1 and V_2, measured in PARASOL simulations with m_2/m_1 = 4 for (a) rare-collision case and (b) collisional case. Simulation results (×) are located near the upper branch. Blue dashed line is $V_2 = (m_1/m_2)^{1/2}V_1$, and orange dashed line is $V_2 = V_1$.

and the lower-branch result was never realized. For the rare-collision case (a) $L_{//}/l_{mfp}$ =0.01, the (V_1, V_2) have a relation $m_1V_1^2 = m_2V_2^2$ as plotted by a blue dashed line. This is due to the same amount of energy gain from the electric field in the SOL plasma. On the other hand for the collisional case (b) $L_{//}/l_{mfp}$ = 100, (V_1, V_2) tend to have the same speed as plotted by an orange dashed line. This is simply due to the collisional relaxation between V_1 and V_2. In either case, (V_1, V_2) are located near the upper branch, $V_1 > C_{s1}$ and $V_2 > C_{s2}$. In the next section, we study the reason why the lower-branch solution is absent.

3. Stability analyses for the Bohm criterion [3,4]

We consider the time-dependent perturbation of the form $\Phi \sim \exp(\gamma t + \kappa x)$. Including the growth rate γ, linear responses of n_e, n_1 and n_2 to Φ are written similar to those for Section 2; $\delta n_e/n_0 = \Phi$, $\delta n_1/n_0 = F_1\Phi\{T_e/(m_1V_{1*}^2 - \gamma_a T_1)\}$ and $\delta n_2/n_0 = F_2\Phi\{T_e/(m_2V_{2*}^2 - \gamma_a T_2)\}$, where $V_{1*} = V_1 + \gamma/\kappa$ and $V_{2*} = V_2 + \gamma/\kappa$. The condition for the monotonic sheath formation is obtained similar to Condition (1):

$$(V_{1*}^2 - C_{s1}^2)(V_{2*}^2 - C_{s2}^2) \geq F_1F_2T_e^2/m_1m_2 . \qquad (2)$$

When (V_1, V_2) are located inside the upper blue region in Fig. 4 (a) (assuming $V > 0$ and $\kappa > 0$), Condition (2) can be satisfied not only for the null growth rate $\gamma = 0$ ((V_{1*}, V_{2*}) = (V_1, V_2) stay inside the upper blue region), but also the negative γ (shifting downward by (γ/κ, γ/κ), (V_{1*}, V_{2*}) stay inside the lower blue region). This means the upper solution of (V_1, V_2) is stable. On the contrary, for the case of (V_1, V_2) inside the lower blue region in Fig. 4 (b), Condition (2) is satisfied for the null growth rate $\gamma = 0$ ((V_{1*}, V_{2*}) = (V_1, V_2) stay inside the lower blue region), and also for the positive γ (shifting upward by (γ/κ, γ/κ), (V_{1*}, V_{2*}) stay inside the upper blue region). This means the lower solution of (V_1, V_2) is unstable. Accordingly the stable upper branch is realized but the unstable lower branch does never appear in the PARASOL simulation.

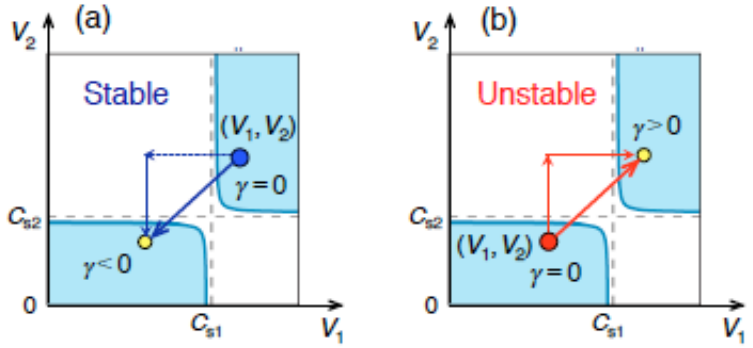

Fig. 4 Stable upper-branch solution (a) and unstable lower-branch solution (b) of (V_1, V_2).

We can understand that the Bohm criterion is a result of the stability condition of plasma fluids. Now we examine whether the Poisson's equation is essential or not for the Bohm criterion. For simplicity we treat a single-species-ion plasma. In the quasi-neutral plasma ($\lambda_D^2 \to 0$), a relation $\delta n_e = \delta n_i$ holds, and the following equation is obtained:

$$(\kappa V_f + \gamma)^2 - \kappa^2 C_s^2 = 0 , \qquad (3)$$

where $C_s^2 = (T_e + \gamma_a T_i)/m_i$. At the outlet of SOL plasma flow, the perturbation is increased monotonically towards the outlet, i.e., $\kappa V_f > 0$. For the stable perturbation ($\gamma \leq 0$), the Bohm criterion, $V_f^2 \geq C_s^2$, is required. Note that Eq. (3) is a dispersion relation for a sound wave with Doppler shift, $(\omega - kV_f))^2 = k^2C_s^2$, when ($\gamma$, κ) are replaced with ($-i\omega$, ik).

In this section, it is clarified that the Bohm criterion is fundamentally realized from the stability condition of the plasma fluid flowing out to the outlet. Also proved that the Bohm criterion is not directly connected with the sheath formation. This finding is a backbone of the SOL-divertor simulation with a virtual divertor model (see next section), which does not require the Bohm criterion as a boundary condition at the divertor plate.

4. Virtual divertor model and Bohm criterion

We have developed a new code for 1D SOL-divertor plasmas with a generalized fluid model taking account of anisotropic ion temperatures, $T_{i//}$ and $T_{i\perp}$ (parallel // and perpendicular ⊥ to the magnetic field) [5,6]. The parallel momentum transport equation is described by a spatially 1st-order differential equation without the 2nd-order viscosity term. This equation does not especially require a boundary condition at the divertor plate. In order to simulate the existence of the divertor plate, we have introduced a virtual divertor (VD) model [5,6]. The VD region is set beyond the divertor plate position (blue vertical line) as shown in Fig. 5 (a). Plasma fluid equations are solved continuously from the SOL-divertor region to this VD region, where artificial sinks for particle, momentum, and energy are added. By coupling the anisotropic-ion-temperature formulation and the VD model, simulation results demonstrated that the flow speed, V_f, at the divertor plate exceeds automatically the sound speed, C_s (or Mach number $M \equiv V_f/C_s \geq 1$). The criterion $M \geq 1$ is required for the temporal-stability condition of the monotonic-profile plasma formation at the plasma boundary. Strong sinks in the VD region generate the monotonic change in the plasma profile at the VD entrance. When $V_f < C_s$, V_f temporally grows up to C_s until the stability condition is satisfied as shown in Fig. 5 (b).

Using this new 1D code, we are studying various physics of SOL-divertor plasmas in tokamaks, such as the detached divertor physics [8]. Application of the new models to comprehensive divertor simulation codes is the future work.

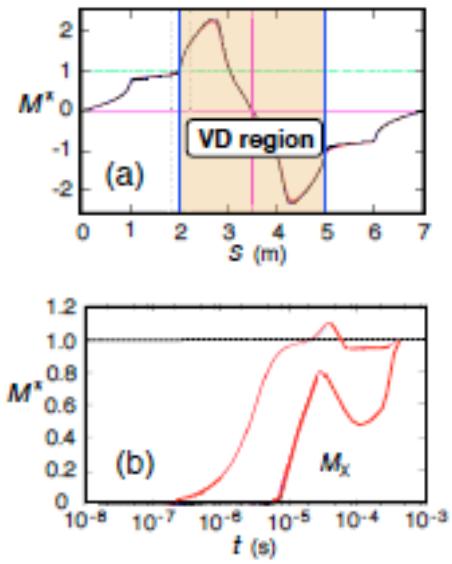

Fig. 5 (a) Profile of Mach number M in a SOL-divertor plasma parallel to magnetic field. (b) Evolution of M at divertor plate (s = 2m) and M_x at x-point (s = 1m).

Acknowledgements The authors thank Prof. Y. Ogawa (U. Tokyo), Dr. K. Ibano (Osaka U.), Dr. K. Hoshino (JAEA) and Dr. M. Nakamura (JAEA) for the collaboration on virtual divertor modeling. One of authors, TT, is grateful to Prof. Y. Ueda of Osaka University for his continuous encouragement.

References

[1] K.-U. Riemann, J. Phys. D: Appl. Phys. **24** (1991) 492.

[2] S. Azuma, A. Fukuyama, T. Takizuka, Contrib. Plasma Phys. **52** (2012) 512.

[3] S. Azuma, "Particle simulation of peripheral plasmas in tokamaks", Master thesis, Graduate School of Engineering, Kyoto University (2014).

[4] T. Takizuka, S. Togo, S. Azuma, A. Fukuyama, "Bohm criterion and virtual divertor model for SOL-divertor simulation", presented at 15th Int. Workshop on Plasma Edge Theory in Fusion Devices (PET-15) (9-11 Sep 2015, Nara, Japan).

[5] S. Togo, T. Takizuka, M. Nakamura, K. Hoshino, Y. Ogawa, J. Nucl. Mater. **463** (2015) 502.

[6] S. Togo, T. Takizuka, M. Nakamura, K. Hoshino, K. Ibano, T. L. Lang, Y. Ogawa, "Self-consistent treatment of the sheath boundary conditions by introducing anisotropic ion temperatures and virtual divertor model", to be published in J. Comput. Phys.

[7] T. Takizuka, Plasma Sci. Technol. **13** (2011) 316.

[8] S. Togo, T. Takizuka, M. Nakamura, K. Hoshino, K. Ibano, T.L. Lang, Y. Ogawa, "Simulation study of detached plasmas by using one-dimensional SOL-divertor fluid code with virtual divertor model", presented at PET-15; to be published in Contrib. Plasma Phys.

Numerical analysis of the effects of radial plasma diffusion on the detached divertor plasmas

Satoshi Togo, Tomonori Takizuka[a)], Makoto Nakamura[b)], Kazuo Hoshino[b)], Kenzo Ibano[a)], Yuichi Ogawa

Graduate School of Frontier Sciences, University of Tokyo, 5-1-5 Kashiwanoha, Kashiwa 277-8568, Japan
[a)]Graduate school of Engineering, Osaka University, 2-1 Yamadaoka, Suita 565-0871, Japan
[b)]Japan Atomic Energy Agency, 2-166 Omotedate, Obuchi-aza, O-aza, Rokkasho 039-3212, Japan

Radial plasma diffusion is considered to be important as a candidate to reduce the particle flux to the divertor plate in addition to the volume recombination. We investigated the effects of radial plasma diffusion on the detached divertor plasmas by using a one-dimensional (1D) scrape-off-layer (SOL)-divertor (DIV) plasma fluid model incorporating anisotropic ion temperature. A virtual divertor (VD) model is implemented in our code in order to reproduce the effects of divertor plate and sheath. The roll-over of the particle flux to the divertor plate becomes smoother with radial plasma diffusion.

1 Introduction

Development of accurate simulation models of scrape-off-layer (SOL)-divertor (DIV) plasma is crucial for the handling of the divertor heat load in the future tokamaks. SOL-DIV code packages such as SOLPS [1], SONIC [2, 3] and UEDGE [4] have been developed and widely used in designing the divertor and predicting the heat load. It is reported, however, that the simulation results of these code packages do not satisfactorily agree with the experimental results [5, 6].

Radial plasma diffusion is considered to be important as a candidate to reduce the particle flux to the divertor plate in addition to the volume recombination [7]. Moreover, it was shown by a Particle-in-Cell (PIC) code with binary collision model that supersonic flows could be driven by the effect of radial plasma diffusion which was considered to become strong in the partially detached divertor plasmas with short radial decay length and help the plasma transit from attached to detached regime more smoothly [8]. A one-dimensional (1D) SOL-DIV plasma fluid simulation code with inviscid approximation showed that supersonic flow was observed in the low DIV temperature conditions and that the particle flux to the divertor plate became lower than that predicted with two-point model with subsonic flow [9]. In a simulation with a code package, on the other hand, the Mach number at the sheath entrance $M_t = 1$ which was given as a boundary condition was changed into $M_t > 1$ in order to drive supersonic flow artificially. The particle flux, however, did not change largely [10]. We suspected that this difference was brought about by the existence of parallel viscosity term in the parallel momentum transport equation.

We investigated the effects of radial plasma diffusion on the detached divertor plasmas by using a 1D SOL-DIV plasma fluid model incorporating anisotropic ion temperature $T_{i,\parallel}$, $T_{i,\perp}$ [11–13]. Because the parallel viscosity term in the parallel momentum transport equation is an approximated form of the ion stress tensor $\pi_i \equiv 2n(T_{i,\parallel} - T_{i,\perp})/3$ in the assumption of $\pi_i << nT_i \equiv n(T_{i,\parallel} + 2T_{i,\perp})/3$, the sum of nT_i and π_i is replaced by $nT_{i,\parallel}$ and the parallel momentum transport equation becomes the first-order differential [15]. Therefore, the flow velocity is determined only by the upstream condition and the boundary condition for M_t is no longer necessary. Instead, we implemented a virtual divertor (VD) model in our code in order to reproduce the effects of divertor plate and sheath [11–14].

In this paper, the numerical model is explained in Sec. 2 and the results are shown in Sec. 3. In Sec.4, summary and future works are described.

2 Numerical Model

2.1 Plasma fluid model

The 1D fluid equations with anisotropic ion temperature $T_{i,\parallel}$, $T_{i,\perp}$ in the system of the homogeneous magnetic field are as follows [11–13];

$$\frac{\partial n}{\partial t} + \frac{\partial}{\partial s}(nV) = S, \tag{1}$$

$$\frac{\partial m_i nV}{\partial t} + \frac{\partial}{\partial s}\left(m_i nV^2 + nT_{i,\parallel} + nT_e\right) = M_m, \tag{2}$$

$$\begin{aligned}&\frac{\partial}{\partial t}\left(\frac{1}{2}m_i nV^2 + \frac{1}{2}nT_{i,\parallel}\right)\\ &+ \frac{\partial}{\partial s}\left(\frac{1}{2}m_i nV^3 + \frac{3}{2}nT_{i,\parallel}V + q_{i,\parallel}\right)\\ &= Q_{i,\parallel} + \frac{n(T_{i,\perp} - T_{i,\parallel})}{\tau_{rlx}} + \frac{m_e}{m_i}\frac{n(T_e - T_{i,\parallel})}{\tau_e}\\ &- V\frac{\partial nT_e}{\partial s},\end{aligned} \tag{3}$$

author's e-mail: togo@ppl.k.u-tokyo.ac.jp

$$\frac{\partial n T_{\mathrm{i},\perp}}{\partial t} + \frac{\partial}{\partial s}\left(n T_{\mathrm{i},\perp} V + q_{\mathrm{i},\perp}\right) = Q_{\mathrm{i},\perp} - \frac{n\left(T_{\mathrm{i},\perp} - T_{\mathrm{i},\parallel}\right)}{\tau_{\mathrm{rlx}}} + \frac{2m_{\mathrm{e}}}{m_{\mathrm{i}}}\frac{n\left(T_{\mathrm{e}} - T_{\mathrm{i},\perp}\right)}{\tau_{\mathrm{e}}}, \tag{4}$$

$$\frac{\partial}{\partial t}\left(\frac{3}{2}nT_{\mathrm{e}}\right) + \frac{\partial}{\partial s}\left(\frac{5}{2}nT_{\mathrm{e}}V + q_{\mathrm{e}}\right) = Q_{\mathrm{e}} + \frac{3m_{\mathrm{e}}}{m_{\mathrm{i}}}\frac{n\left(T_{\mathrm{i}} - T_{\mathrm{e}}\right)}{\tau_{\mathrm{e}}} + V\frac{\partial n T_{\mathrm{e}}}{\partial s}. \tag{5}$$

Here, we assume that the inner/outer SOL-divertor system is symmetry. The definitions of the notations are the same as those in Refs. [11–13]. Here, we set the heat flux limiters to be $\alpha_{\mathrm{i},\parallel} = \alpha_{\mathrm{i},\perp} = 0.5$ and $\alpha_{\mathrm{e}} = 0.2$. The relaxation time of ion temperature is assumed to be $\tau_{\mathrm{rlx}} = 2.5\tau_{\mathrm{i}}$ [16, 17]. The sound speed is defined as $c_{\mathrm{s}} = \sqrt{\left(T_{\mathrm{e}} + T_{\mathrm{i},\parallel}\right)/m_{\mathrm{i}}}$. The boundary conditions for the heat fluxes of ion and electron are prescribed as follows;

$$\frac{1}{2}m_{\mathrm{i}}nV^3 + \frac{5}{2}nT_{\mathrm{i}}V + q_{\mathrm{i}} = \gamma_{\mathrm{i}}nT_{\mathrm{i}}V, \tag{6}$$

$$\frac{5}{2}nT_{\mathrm{e}}V + q_{\mathrm{e}} = \gamma_{\mathrm{e}}nT_{\mathrm{e}}V, \tag{7}$$

where $q_{\mathrm{i}} = q_{\mathrm{i},\parallel} + q_{\mathrm{i},\perp}$, and γ_{i} and γ_{e} are the sheath heat transmission factors for ion and electron, respectively.

2.2 Neutral fluid model

Neutrals are divided into recycling neutrals generated on outer and inner divertor plate and diffusion ones generated in the plasma whose densities are denoted by $n^{\mathrm{out}}_{\mathrm{n,recy}}$, $n^{\mathrm{inn}}_{\mathrm{n,recy}}$ and $n_{\mathrm{n,diff}}$, respectively. This model is similar to the first-flight corrected diffusion (FFCD) model in Ref. [18]. The equations are as follows [12];

$$\frac{\partial n^{\mathrm{out}}_{\mathrm{n,recy}}}{\partial t} + \frac{\partial}{\partial x}\left(n^{\mathrm{out}}_{\mathrm{n,recy}}V^{\mathrm{out}}_{\mathrm{n,recy}}\right) = S^{\mathrm{out}}_{\mathrm{n,recy}}, \tag{8}$$

$$\frac{\partial n^{\mathrm{inn}}_{\mathrm{n,recy}}}{\partial t} + \frac{\partial}{\partial x}\left(n^{\mathrm{inn}}_{\mathrm{n,recy}}V^{\mathrm{inn}}_{\mathrm{n,recy}}\right) = S^{\mathrm{inn}}_{\mathrm{n,recy}}, \tag{9}$$

$$\frac{\partial n_{\mathrm{n,diff}}}{\partial t} + \frac{\partial}{\partial x}\left(-D_{\mathrm{n}}\frac{\partial n_{\mathrm{n,diff}}}{\partial x}\right) = S_{\mathrm{n,diff}}. \tag{10}$$

Here, the coordinate x is in the poloidal direction and $x = s\sin\theta$. We set the pitch angle to be $\theta = 6^\circ$. The velocities of the recycling neutrals $V^{\mathrm{out}}_{\mathrm{n,recy}}\left(= -V^{\mathrm{inn}}_{\mathrm{n,recy}}\right)$ and the diffusivity of the diffusion neutrals D_{n} are the same as Ref. [12]. Assuming that the diffusion neutrals impinging the divertor plates do not reflect and become recycling neutrals, we impose the following boundary condition at the divertor plate [12];

$$-D_{\mathrm{n}}\frac{\partial n_{\mathrm{n,diff}}}{\partial x} = C_{\mathrm{n}}n_{\mathrm{n,diff}}v_0. \tag{11}$$

Here, the coefficient C_{n} is given from kinetic considerations.

2.3 Source terms

The source terms for the plasma and neutrals are as follows;

$$S = S^{\mathrm{core}} + n_{\mathrm{n}}\nu_{\mathrm{iz}} - n\nu_{\mathrm{rc}} + S^{\perp} + S^{\mathrm{VD}}, \tag{12}$$

$$M_{\mathrm{m}} = m_{\mathrm{i}}n^{\mathrm{out}}_{\mathrm{n,recy}}V^{\mathrm{out}}_{\mathrm{n,recy}}\sin\theta\left(\nu_{\mathrm{iz}} + \nu_{\mathrm{cx}}\right) + m_{\mathrm{i}}n^{\mathrm{inn}}_{\mathrm{n,recy}}V^{\mathrm{inn}}_{\mathrm{n,recy}}\sin\theta\left(\nu_{\mathrm{iz}} + \nu_{\mathrm{cx}}\right) - m_{\mathrm{i}}V\left(n_{\mathrm{n}}\nu_{\mathrm{cx}} + n\nu_{\mathrm{rc}}\right) + M^{\perp}_{\mathrm{m}} + M^{\mathrm{VD}}_{\mathrm{m}}, \tag{13}$$

$$Q_{\mathrm{i},\parallel} = Q^{\mathrm{core}}_{\mathrm{i},\parallel} + \frac{2}{3}m_{\mathrm{i}}n_{\mathrm{n,recy}}V^2_{\mathrm{n,recy}}\left(\nu_{\mathrm{iz}} + \nu_{\mathrm{cx}}\right) + \frac{1}{2}n_{\mathrm{n,diff}}T_{\mathrm{i}}\left(\nu_{\mathrm{iz}} + \nu_{\mathrm{cx}}\right) + Q^{\perp}_{\mathrm{i},\parallel} - \left(\frac{1}{2}m_{\mathrm{i}}V^2 + \frac{1}{2}T_{\mathrm{i},\parallel}\right)\left(n_{\mathrm{n}}\nu_{\mathrm{cx}} + n\nu_{\mathrm{rc}}\right) + Q^{\mathrm{VD}}_{\mathrm{i},\parallel}, \tag{14}$$

$$Q_{\mathrm{i},\perp} = Q^{\mathrm{core}}_{\mathrm{i},\perp} + \left(\frac{4}{3}m_{\mathrm{i}}n_{\mathrm{n,recy}}V^2_{\mathrm{n,recy}} + n_{\mathrm{n,diff}}T_{\mathrm{i}}\right)\left(\nu_{\mathrm{iz}} + \nu_{\mathrm{cx}}\right) - T_{\mathrm{i},\perp}\left(n_{\mathrm{n}}\nu_{\mathrm{cx}} + n\nu_{\mathrm{rc}}\right) + Q^{\perp}_{\mathrm{i},\perp} + Q^{\mathrm{VD}}_{\mathrm{i},\perp}, \tag{15}$$

$$Q_{\mathrm{e}} = Q^{\mathrm{core}}_{\mathrm{e}} - \epsilon_{\mathrm{iz}}n_{\mathrm{n}}\nu_{\mathrm{iz}} - \frac{3}{2}nT_{\mathrm{e}}\nu_{\mathrm{rc}} - L_z r_{\mathrm{imp}}n^2 + Q^{\perp}_{\mathrm{e}} + Q^{\mathrm{VD}}_{\mathrm{e}}, \tag{16}$$

$$S^{\mathrm{out}}_{\mathrm{n,recy}} = -n^{\mathrm{out}}_{\mathrm{n,recy}}\left(\nu_{\mathrm{cx}} + \nu_{\mathrm{iz}} + \nu_{\mathrm{L,recy}}\right) + S^{\mathrm{out,VD}}_{\mathrm{n,recy}}, \tag{17}$$

$$S^{\mathrm{inn}}_{\mathrm{n,recy}} = -n^{\mathrm{inn}}_{\mathrm{n,recy}}\left(\nu_{\mathrm{cx}} + \nu_{\mathrm{iz}} + \nu_{\mathrm{L,recy}}\right) + S^{\mathrm{inn,VD}}_{\mathrm{n,recy}}, \tag{18}$$

$$S_{\mathrm{n,diff}} = -n_{\mathrm{n,diff}}\left(\nu_{\mathrm{iz}} + \nu_{\mathrm{L,diff}}\right) + n_{\mathrm{n,recy}}\nu_{\mathrm{cx}} + n\nu_{\mathrm{cx}} + S^{\mathrm{inn,VD}}_{\mathrm{n,recy}}. \tag{19}$$

Here, the superscript "$\perp$" represents the sinks due to radial plasma diffusion which are explained in the next section. We introduce the simple radiative cooling model with radiation rate of carbon L_z [19]. The impurity ratio to the plasma density is denoted by r_{imp}. The definitions of other notations are the same as Ref. [12]. For the energy loss due to ionization and excitation, $\epsilon_{\mathrm{iz}} = 30$ eV was used.

2.4 Radial plasma diffusion

Similar to the particle and heat fluxes from the core plasma, we treat the effect of radial plasma diffusion with sink terms in DIV as follows;

$$S^{\perp} = -\frac{n}{\tau^{\perp}}, \tag{20}$$

$$M^{\perp}_{\mathrm{m}} = -\frac{m_{\mathrm{i}}nV}{\tau^{\perp}}, \tag{21}$$

$$Q^{\perp}_{\mathrm{i},\parallel} = -\frac{1}{\tau^{\perp}}\left(\frac{1}{2}m_{\mathrm{i}}nV^2 + g^{\perp}_{\mathrm{i},\parallel}\frac{1}{2}nT_{\mathrm{i},\parallel}\right), \tag{22}$$

$$Q^{\perp}_{\mathrm{i},\perp} = -\frac{g^{\perp}_{\mathrm{i},\perp}nT_{\mathrm{i},\perp}}{\tau^{\perp}}, \tag{23}$$

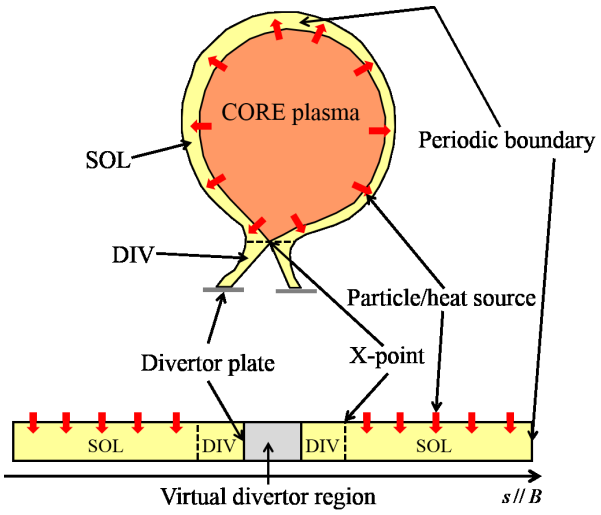

Fig. 1 Schematic of the SOL-DIV 1D system with a VD model.

$$Q_{\rm e}^{\perp} = -\frac{1}{\tau^{\perp}}\left(g_{\rm e}^{\perp}\frac{3}{2}nT_{\rm e}\right), \tag{24}$$

where the time constant of the radial plasma diffusion is estimated in terms of the input radial decay length d_1 and particle diffusion coefficient $D_\perp$ as follows;

$$\tau^{\perp} = \frac{d_1^2}{D_\perp}. \tag{25}$$

The effect of non-zero radial heat diffusion coefficients, $\chi_{\rm i,\perp}$ and $\chi_{\rm e,\perp}$, can be considered by setting the values of the coefficients $g^{\perp}$ to be larger than 1. In this paper, we used $g_{\rm i,\parallel}^{\perp} = g_{\rm i,\perp}^{\perp} = g_{\rm e}^{\perp} = 3$ assuming that $\chi_{\rm i,\perp} = \chi_{\rm e,\perp} = 2D_\perp$. In this study, we used $D_\perp = 0.5\ {\rm m}^2/{\rm s}$.

2.5 Virtual divertor model

Instead of imposing boundary conditions, such as $M_{\rm t} = 1$, sheath heat transmission factors for plasma and recycling flux for neutrals, we use a virtual divertor (VD) model [11–14]. We introduce an artificial region (VD region) beyond the sheath entrance, as shown in Fig. 1, and set artificial sinks for plasma particle, momentum, energy, diffusion neutrals and an artificial source for recycling neutrals there as follows;

$$S^{\rm VD} = -\frac{n}{\tau^{\rm VD}}, \tag{26}$$

$$M_{\rm m}^{\rm VD} = -\frac{m_{\rm i}nV}{\tau^{\rm VD}} + \frac{\partial}{\partial s}\left(m_{\rm i}nD_{\rm m}^{\rm VD}\frac{\partial V}{\partial s}\right), \tag{27}$$

$$Q_{\rm i,\parallel}^{\rm VD} = -\frac{1}{\tau^{\rm VD}}\left(\frac{1}{2}m_{\rm i}nV^2 + g_{\rm i,\parallel}^{\rm VD}\frac{1}{2}nT_{\rm i,\parallel}\right), \tag{28}$$

$$Q_{\rm i,\perp}^{\rm VD} = -\frac{g_{\rm i,\perp}^{\rm VD}nT_{\rm i,\perp}}{\tau^{\rm VD}}, \tag{29}$$

$$Q_{\rm e}^{\rm VD} = -\frac{1}{\tau^{\rm VD}}\left(g_{\rm e}^{\rm VD}\frac{3}{2}nT_{\rm e}\right), \tag{30}$$

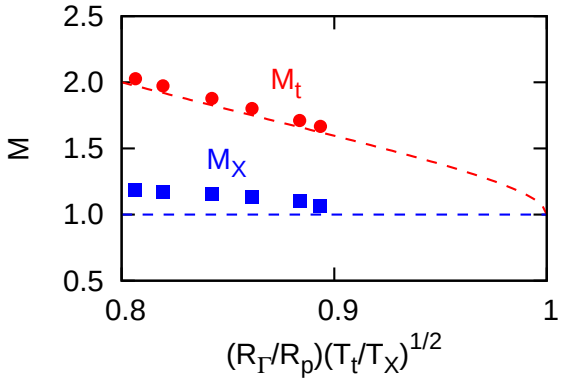

Fig. 2 Mach number at the sheath entrance $M_{\rm t}$ (circles) and at the X-point $M_{\rm X}$ (squares) as functions of C. The theoretical values are shown by the dashed lines.

$$S_{\rm n,recy}^{\rm out,VD} = \eta\frac{n}{\tau^{\rm VD}}H(-V) + \eta_{\rm n}\frac{n_{\rm n,diff}}{\tau_{\rm n}^{\rm VD}}H\left(\frac{\partial n_{\rm n,diff}}{\partial x}\right), \tag{31}$$

$$S_{\rm n,recy}^{\rm inn,VD} = \eta\frac{n}{\tau^{\rm VD}}H(V) + \eta_{\rm n}\frac{n_{\rm n,diff}}{\tau_{\rm n}^{\rm VD}}H\left(-\frac{\partial n_{\rm n,diff}}{\partial x}\right), \tag{32}$$

$$S_{\rm n,diff}^{\rm VD} = -\frac{n_{\rm n,diff}}{\tau_{\rm n}^{\rm VD}}. \tag{33}$$

Here, the definitions of the notations are the same as Ref. [12]. We used $\tau^{\rm VD} = 5\ \mu{\rm s}$ and $\tau_{\rm n}^{\rm VD} = 1\ \mu{\rm s}$. The energy sink coefficients were set to be $g_{\rm i,\parallel}^{\rm VD} = 3$, $g_{\rm i,\perp}^{\rm VD} = 1.2$ and $g_{\rm e}^{\rm VD} = 2.5$. Strictly speaking, we need to control the values of $\tau_{\rm n}^{\rm VD}$ and $g^{\rm VD}$ in order to satisfy the boundary conditions, Eqs. (6), (7) and (11). Nevertheless, we used fixed values for them in this study because the ranges of output values of $\gamma_{\rm i}$, $\gamma_{\rm e}$ and $C_{\rm n}$ were sufficiently narrow. The recycling rates were $\eta = \eta_{\rm n} = 1$.

3 Results

3.1 Supersonic flows in no-neutral conditions

First, we conducted simulations for different values of $d_1/d_{\rm DIV}$ in no-neutral conditions in order to study the supersonic flows. Figure 2 shows the Mach number at the sheath entrance $M_{\rm t}$ and at the X-point $M_{\rm X}$ as functions of C which is defined by the following equation;

$$C \equiv \frac{R_\Gamma}{R_p}\sqrt{\frac{T_{\rm t}}{T_{\rm X}}}. \tag{34}$$

Here, R_Γ and R_p represent the particle and momentum flux amplification factors, respectively, and $T \equiv T_{\rm i,\parallel} + T_{\rm e}$. The theoretical values shown by the dashed lines are obtained in the same way as Refs. [8, 13]. By setting finite values of $d_1/d_{\rm DIV}$, supersonic flows are driven and they agree well with the theoretical values.

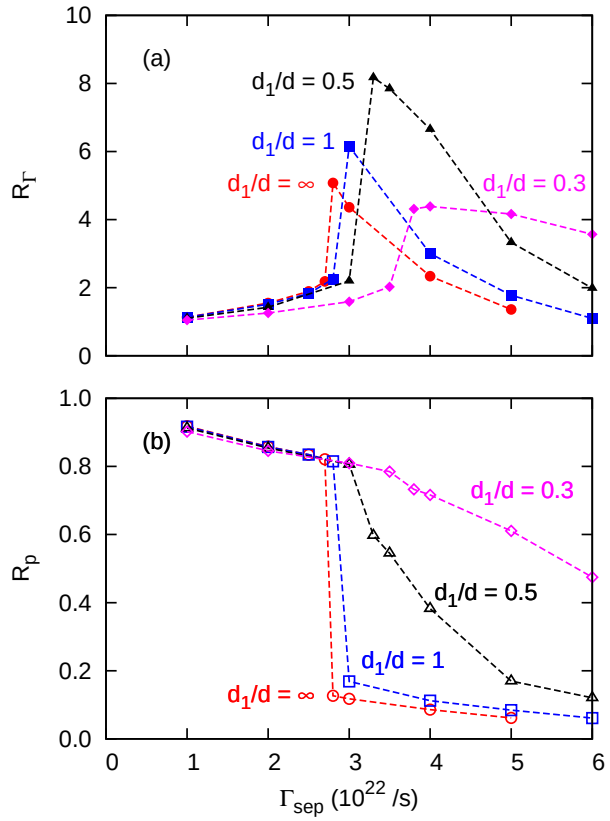

Fig. 3 Particle and momentum flux amplification factors R as functions of $\Gamma_{\rm sep}$ for $d_1/d_{\rm DIV} = \infty$, 1, 0.5 and 0.3.

3.2 Effect of radial plasma diffusion on detached plasmas

We investigated the effect of the radial plasma diffusion on the relations between the flux amplification factors R and the particle flux from the core plasma $\Gamma_{\rm sep}$. Here, the geometrical parameters are the same as Ref. [12] and the heat flux from the core plasma is set to be $P_{\rm sep} = 4$ MW. The impurity ratio is $r_{\rm imp} = 1$ %. The result is shown in Fig. 3. When $d_1/d_{\rm DIV} = 0.5$, R_Γ starts to decrease (roll-over) with smoothly decreasing R_p, which is qualitatively similar to the experimental observations. In these simulations, supersonic flows are not observed.

4 Summary and Future Works

Radial plasma diffusion is considered to be important as a candidate to reduce the particle flux to the divertor plate in addition to the volume recombination. We investigated the effects of radial plasma diffusion on the detached divertor plasmas by using a 1D SOL-DIV plasma fluid model incorporating anisotropic ion temperature [11–13]. A VD model is implemented in our code in order to reproduce the effects of divertor plate and sheath [14]. The supersonic flows are driven by the effect of the radial plasma diffusion which agrees well with the theoretical values. The roll-over of the particle flux to the divertor plate becomes smoother with radial plasma diffusion.

For the present study, the homogeneous magnetic field and the symmetric inner/outer SOL-DIV systems are assumed for simplicity. In order to simulate the inhomogeneous magnetic field and the asymmetric SOL-DIV systems, the effects of the mirror force and the plasma current should be considered. For the transient simulations, we need to control the values of $g^{\rm VD}$ and $\tau_{\rm n}^{\rm VD}$ in order to satisfy the prescribed boundary conditions. These are our future works.

References

[1] R. Schneider *et al.*, Contrib. Plasma Phys. **46** (2006) 3.
[2] H. Kawashima *et al.*, Plasma Fusion Res. **1** (2006) 031.
[3] K. Shimizu *et al.*, Nucl. Fusion **49** (2009) 065028.
[4] T. D. Rognlien *et al.*, J. Nucl. Mater. **196-198** (1992) 347.
[5] A. V. Chankin *et al.*, J. Nucl. Mater. **390-391** (2009) 319.
[6] M. Wischmeier *et al.*, J. Nucl. Mater. **415** (2011) S523.
[7] K. Hoshino *et al.*, J. Nucl. Mater. **463** (2015) 573.
[8] T. Takizuka *et al.*, J. Nucl. Mater. **290-293** (2001) 753.
[9] O. Marchuk and M. Z. Tokar, Contrib. Plasma Phys. **48** (2008) 164.
[10] K. Hoshino *et al.*, Plasma Fusion Res. Ser. **9** (2010) 592.
[11] S. Togo *et al.*, J. Nucl. Mater. **463** (2015) 502.
[12] S. Togo *et al.*, Contrib. Plasma Phys. *to be published.*
[13] S. Togo *et al.*, J. Comput. Phys. **310** (2016) 109.
[14] T. Takizuka *et al.*, 13th Burning Plasma Simulation Initiative (BPSI) Meeting (2016).
[15] R. V. Bravenec *et al.*, Phys. Fluids **25** (1982) 608.
[16] E. Zawaideh *et al.*, Phys. Fluids **29** (1986) 463.
[17] W. Fundamenski, Plasma Phys. Control. Fusion **47** (2005) R163.
[18] A. K. Prinja *et al.*, J. Nucl. Mater. **196-198** (1992) 340.
[19] D. E. Post, J. Nucl. Mater. **220-222** (1995) 143.

Predictive simulation of fusion plasma by data assimilation

Takahisa Ozeki
Fusion Research and Development Directorate
Japan Atomic Energy Agency

Introduction and motivation: Experiments for fusion energy have been carried out in many tokamak facilities in the world, and experimental data related to the fusion plasma is accumulated by these facilities. In ITER remote experimentation center (REC) based on the broader approach (BA) activity of the joint program of Japan and Europe (EU), the storage system is being prepared as one of the important function, which can store/access the huge amount of fusion relevant experiment data. For the efficient use of the experiment data, the introduction of statistics is expected, such as Bayesian analysis for the data analysis to determination of the unknown parameter of Modified Rutherford Equation for the stabilization of NTM, etc., and Big data analyses using analysis engine, visualization, data collection/mining, work flow, etc. For the simulation, data assimilation to the simulation can be expected, that is the prediction of the fusion plasma by the theoretical simulation with experiment data. Here, predictive simulation of fusion plasma by the data assimilation is discussed.

In DEMO reactor, where possible diagnostics are very limited, the simulation is strongly expected for the guide of the operation. The integrated simulation of the fusion plasma is useful tool for the guide of the plasma operation by the integration of the plasma model. In addition to the development of the plasma mode for the integration, the efficient use of the real experimental data with the simulation is useful method to navigate the DEMO operation. The assimilation of the experiment data can be obtained by adapting the experimentally observed data on numerical simulation of the fusion plasma. Other methods are to set the optimal initial conditions by assimilation of past data or to embed and to adapt the observed value data to the physical model of the simulation. It has already been performed in the field of Meteorology, such as weather forecasts[1-2)], but its application in the nuclear fusion field has not been enough yet.

Methods of data assimilation: The simple methods of the data assimilation on the simulation are the direct insertion that is to replace simulation results by observed data or the Nudging that is to slightly bring simulation results to observed values. These methods are simple but need many observed data point, otherwise the assimilation is not enough for accuracy. For more accurate assimilation, methods of the Optimal Interpolation and 3-dimensional variational method are proposed as the 3-dimensional data assimilation, where the generalized form can be obtained by using the Bayes' theorem. For the method including the past data, the 4-dimensional data assimilation can be applied, such as Sequential data assimilation of Kalman filter or Ensemble Kalman filter, and 4-dimensional variational method. These methods can be understand as the minimization method of the difference of the value between the simulation data and the observed data

Formulation for the data assimilation: The linear system is discussed here as the first step. The discretized numerical simulation model can be described by $x_t=F_t\, x_{t-1}$ to estimate the state of x_n . The system model and the observed model can be written as follows respectively:

$$x_t = F_t x_{t-1} + v_t \quad , \quad y_t = H_t x_t + w_t$$

where, x_t is variable vector of the system model at the time t , y_t is variable vector of the observed model at the time t , v_t is uncertainty by the modelling and the boundary condition x_0,

w_t is observed noise. Dimension of x_t is larger than that of y_t. Therefore, Ht is written like as, In this case, the dimension of the observed point, y_t, is three that is smaller than the dimension

$$H = \begin{pmatrix} 1 & 0 & 0 & \cdot & \cdot & 0 \\ 0 & 1 & 0 & \cdot & \cdot & 0 \\ 0 & 0 & 1 & \cdot & \cdot & 0 \end{pmatrix}$$

of the simulation data, x_t.

The most plausible estimated value, $x_{t,\,est}$ can be obtained in the case of maximizing $p(x_t \mid y_t)$, which is written as

$$p(x_t \mid y_t) = \frac{p(y_t \mid x_t)p(x_t)}{\int p(y_t \mid x_t)p(x_t)\,dx_t} \quad ,$$

the conditional probability that can be obtained using the Bayes' theorem. Here, $p(x_t)$ is the probability of "x_t at the point of no observation would be around this value". $p\,(x_t)$ and $p(y_t \mid x_t)$ are assumed to follow a multi-dimensional (k order) normal distribution, such as follows:

$$p(x_t) = \frac{1}{\sqrt{(2\pi)^k \mid V \mid}} \exp\left(-\frac{1}{2}(x_t - x_{t,b})^T V^{-1}(x_t - x_{t,b})\right)$$

$$p(y_t \mid x_t) = \frac{1}{\sqrt{(2\pi)^k \mid R \mid}} \exp\left(-\frac{1}{2}(y_t - H_t x_t)^T R^{-1}(y_t - H_t x_t)\right)$$

using V, R is the variance-covariance matrix (positive value symmetric matrix). $X_{t,b}$ is the mean vector. From Bayes' theorem, for minimizing the following function

$$\frac{1}{2}(x_t - x_{t,b})^T V^{-1}(x_t - x_{t,b}) + \frac{1}{2}(y_t - H_t x_t)^T R^{-1}(y_t - H_t x_t) \quad ,$$

x_t becomes the most plausible estimated value , $x_{t,\,\mathrm{est}}$, as follows:

$$\bar{x}_{t,est} = x_{t,b} + VH_t^T(H_t V H_t^T + R)^{-1}(y_t - H_t x_{t,b})$$

This means maximizing the probability of $p(x_t \mid y_t)$. For the sequential data assimilation using Kalman filter, the conditional probability $p(x_t \mid y_t)$ is obtained by using the average data and the variance-covariance matrix of x_{t-1} on previous step. Values of the next step, $t|t\text{-}1$, are obtained from value of the previous step, $t\text{-}1$. The averaged value of $p(x_t)$, $x_{t|t-1}$ and variance-covariance matrix $V_{t|t-1}$ are obtained from the system model as follows:

$$x_{t|t-1} = F_t x_{t-1|t-1} \quad , \quad V_{t|t-1} = F_t V_{t-1|t-1} F_t^T + Q_t$$

The filtered value of $x_{t|t-1}$ and $p(x_t \mid y_t)$ are obtained by the filtering of . $x_{t|t-1}$ and $V_{t|t-1}$.

$$x_{t|t} = x_{t|t-1} + V_{t|t-1}H_t^T(H_t V_{t|t-1} H_t^T + R_t)^{-1}(y_t - H_t x_{t|t-1})$$

$$V_{t|t} = \left[I - V_{t|t-1}H_t^T(H_t V_{t|t-1} H_t^T + R_t)^{-1} H_t\right] V_{t|t-1}$$

Implementation of Kalman filter to the fusion plasma: The heat and particle transport of the fusion plasma using the well known transport equation of the ion and electron is proposed as the implementation of the data assimilation simulation.

$$\frac{3}{2}\frac{\partial}{\partial t}(n_e T_e) = -\frac{1}{r}\frac{\partial}{\partial r}(rQ_e) + P_{OH} + P_{heat}^e + P_{eq} - P_{rad} + P_n^e$$

$$\frac{3}{2}\frac{\partial}{\partial t}(n_i T_i) = -\frac{1}{r}\frac{\partial}{\partial r}(rQ_i) + P_{heat}^i - P_{eq} - P_{cx} + P_n^i$$

here, $Q_e = -n_e x_e \frac{\partial T_e}{\partial r} + \frac{3}{2}T_e\Gamma_e$, $Q_i = -n_i x_i \frac{\partial T_i}{\partial r} + \frac{3}{2}T_i\Gamma_i$ and $\Gamma_i = \Gamma_e = -D\frac{\partial n_i}{\partial r} - n_i V_{in}$

At the first step, it is assumed that these transport equations can be linearized as the system model,

$$x_t = F_t x_{t-1} + v_t \ .$$

From the form of the equation, $\frac{3}{2} n \frac{\partial x}{\partial t} = -\frac{1}{r}\frac{\partial}{\partial r}(rQ) + \cdots\cdots$, it can be imagine that x_t can be the electron temperature, *Te*, or the ion temperature, *T*i, at the data on the plasma minor radius. v_t of the system model is produced by the uncertainty due to the transport model, such as χe , χi. Variance-covariance matrix V of x_t for the various uncertainty of N is

$$V_{t|t-1} = \frac{1}{N-1}\sum_{i=1}^{N}\left(x_{t|t-1}^{(i)} - \hat{x}_{t|t-1}\right)\left(x_{t|t-1}^{(i)} - \hat{x}_{t|t-1}\right)^{T} \ .$$

Here, the average value $\hat{x}_{t|t-1}$ are $\hat{x}_{t|t-1} = \frac{1}{N}\sum_{i=1}^{N} x_{t|t-1}^{(i)}$ For the observed data, y_t, the diagnostic data from Thomson scattering, ECE, etc. can be applied. The observation noise can be obtained from the error and noise of the diagnostic system.

For the non-linear system model, Ensemble Kalman filter can be applied, where the system model will be $x_t = f_t(x_{t-1}, v_t)$. The procedure of the calculation is same manner in that of the Kalman filter. The system noise of N can be obtained $\left\{v_t^{(i)}\right\}_{i=1}^{N}$. The estimated value $x_{t|t-1}$ is calculated for each i as $x_{t|t-1}^{(i)} = f_t^{(i)}\left(x_{t-1|t-1}^{(i)}, v_t^{(i)}\right)$. The observed noise is made from the diagnostic data for each i as $\left\{w_t^{(i)}\right\}_{i=1}^{N}$. Using the variance-covariance matrix V and R, $x_{t|t-1}$ will be filtered, namely modified.

$$x_{t|t}^{(i)} = x_{t|t-1}^{(i)} + K_t\left(y_t - H_t x_{t|t-1}^{(i)}\right)$$

Here, K_t is Kalman gain. These steps will proceed for each i in parallel, namely these processes are ensemble.

In Summary, the possibility of the implementation of the data assimilation to the simulation of the fusion plasma is discussed. Considering the difficulty with the treatment of the observed data, it seems to be easiest way of the application to the transport equations, however it is still not clear in the validity of the assumption on application to the Kalman filter, the handle the system noise, and so on. It is necessary to investigate of the other filtering models and to proceed the implementation to the actual fusion plasma model.

Acknowledgement:
I would like to thank for the discussion with Drs. O. Naito and S. Ide of JAEA.

References
1) K.Nakamura, G.Ueno, T.Higuch, Tokei-Suri, Vol.53, 2, 211-229 (2005)
2) K.Yumimoto, Nagare Vol. 28, 37-44 (2009)

Development of PHZ pinch model with plasma rotation effects on particle orbit

T. Fujita, Y. Shimizu

Graduate School of Engineering, Nagoya University
Furo-cho, Chikusa-ku, Nagoya 464-8603, Japan

The inward pinch model for high-Z impurity ions in a toroidally rotating plasma, the PHZ pinch model, has been improved to take account of the velocity pitch angle distribution and effects of the centrifugal force and the Coriolis force. It was found that the PHZ pinch velocity is large for particles with larger orbit width. The PHZ pinch velocity averaged over the pitch angle becomes large with increase in the plasma rotation as in the original model.

1. Introduction

Related to the observation that accumulation of tungsten (W) was enhanced with increase in the counter toroidal rotation in JT-60U H-mode plasmas [1], two pinch models (PHZ pinch and E_r pinch) for high Z impurity ions caused by the toroidal rotation and the radial electric field were proposed [2]. The PHZ pinch is caused by change in the ion charge number Z along its drift orbit. The E_r pinch is caused by collision in the deformed drift orbit due to the radial electric field E_r. These two pinch models have been introduced into TOTAL and the results of the JT-60U experiments were simulated. Since the assumption employed for development of the E_r pinch velocity formula was not satisfied, only the PHZ pinch was evaluated. Dependence of W accumulation on the plasma rotation was seen, but was weaker than the experimental observation [3].

In the original PHZ pinch model, the situation that the toroidal rotation speed of impurity ions, which is equal to that of plasma (bulk ions), is much larger than their thermal speed is assumed and then only passing particles with velocity constant during its orbit circulation is considered. In the experiment, however, concentration of high Z impurity on the low-field-side (LFS) was observed in rotating plasmas [4]. In the frame rotating with the same speed as the plasma, the origin of this phenomenon can be regarded as the centrifugal force acting on the particles. In this article, we report on the formulation for adding this effect on the original PHZ model and show some initial results obtained by the new formula.

2. PHZ for arbitrary pitch angles

In the original PHZ model, the following assumptions were made.

(i) The particles have monotonic energy and its velocity component perpendicular to the magnetic field $v_\perp$ is negligibly small compared to its velocity component parallel to the magnetic field $v_\parallel$. So, conservation of magnetic moment μ does not cause any decrease in $v_\parallel$ on the high-field side (HFS) and hence no trapped particles exist.

(ii) The change in the particle energy caused by its radial drift with presence of the radial electric field E_r is not taken into account while change in the poloidal velocity due to the ExB drift is taken into account.

Concentration of heavy ions on the LFS indicates existence of trapped heavy ions. So we calculate particle guiding center orbit with arbitrary pitch angles, namely including both passing and trapped particles, and evaluate the PHZ pinch velocity generated in the orbit

It is assumed that the W ions rotate with the same speed as the bulk plasma (bulk ions). So, their speed in the rotating frame is only due to thermal motions and is isotropic. So, first we extend the PHZ model for arbitrary particle pitch angles, before including plasma rotation effects, namely the centrifugal force and the Coriolis force.

A new code for calculating the PHZ pinch was produced. We plan to introduce it into TOTAL code in future. The guiding center orbit is numerically calculated with the 4th order Runge-Kutta method in a circular cross-section equilibrium for a particle with monotonic energy and with an arbitrary pitch angle. In this article, $\xi = v_\parallel / v$ is used for the pitch angle parameter. First, we calculate the orbit with constant charge Z of ions. Then, we calculate variation of Z along the orbit, which is caused by the temperature variation along the drift orbit and evaluate the PHZ pinch velocity V_{PHZ} by integrating v_r during orbit circulation. This is basically the same procedure as employed in the

original PHZ model, though it is now evaluated numerically while it was evaluated analytically in the original model [2].

$$V_{PHZ} = \frac{1}{T}\int_0^T v_r dt$$

$$v_r = \frac{m_Z}{ZeR_0B_0}\left(v_\parallel^2 + \frac{1}{2}v_\perp^2\right)\sin\theta$$

Here T is the period for completing the closed orbit in the poloidal cross-section, m_Z and Z are the mass and charge number of impurity ions, R_0 is the plasma major radius, B_0 is the magnetic field at $R = R_0$, and θ is the poloidal angle.

We calculated the orbit in the laboratory frame, namely without the centrifugal force or the Coriolis force, but with arbitrary ξ, and then calculated V_{PHZ}. We compared V_{PHZ} for the particle with $\xi = 1$ and verified good agreement with the original model [5]. Next the orbits and the PHZ pinch velocity for arbitrary pitch angle particles were calculated. An example of the result is shown in Fig. 1. Figure 1 (a) shows the half width of the orbit $\Delta = (r_{max} - r_{min})/2$, where r_{max} and r_{min} are the maximum and minimum values of the minor radius in the orbit circulation. Here the boundary between trapped and passing particles is given by $|\xi| = 0.61$. The Δ is larger for trapped particles except for deeply trapped ones, or near the point $\xi = 0$, than for passing particles. The V_{PHZ} is large for the particles with large orbit width, such as barely trapped ones, as shown in Fig. 1 (b). The PHZ pinch velocity for particles with a pitch angle distribution would be evaluated by averaging V_{PHZ} given in Fig. 1 (b) with weight proportional to its velocity distribution function, which is denoted by $\langle V_{PHZ}\rangle$ here. The $\langle V_{PHZ}\rangle$ becomes larger with increase in the particle velocity or energy.

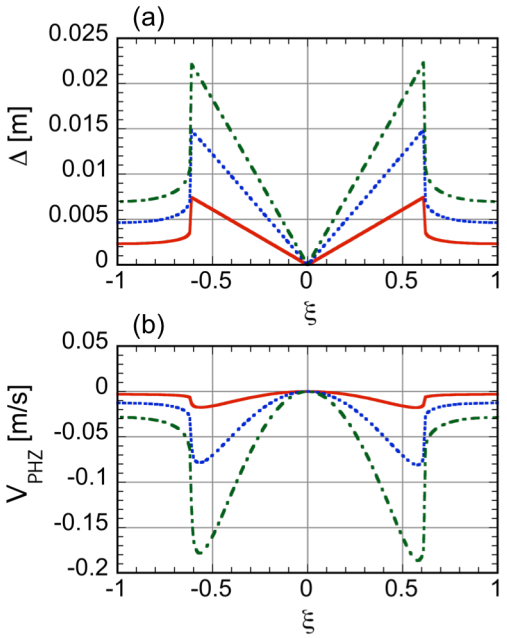

Fig. 1 (a) The half width of the guiding center orbit Δ and (b) the PHZ pinch velocity V_{PHZ} as a function of the pitch angle parameter ξ for three values of particle velocity, 0.5×10^5 m/s (red solid line), 1×10^5 m/s (blue dotted line) and 1.5×10^5 m/s (green dot-dash line).

3. Centrifugal force and Coriolis force effect on PHZ

The equation of motion for the guiding centers in the rotating frame is given in [6,7]. Here the rotation speed of the frame is taken to be the same as the plasma (bulk ion) rotation speed, assuming that the rotation speed of the impurity ions is the same as that of bulk ions. Furthermore, it is assumed that $E_r = 0$ in the rotating frame. Note that this assumption does not mean that $E_r = 0$ in the laboratory frame. The E_r in the laboratory frame E_r^{lab} and in the rotation frame E_r^{rot} are related by

$$E_r^{lab} = E_r^{rot} + RB_\theta\Omega$$

where Ω is the angular frequency of the rotation. Then, $E_r^{lab} > 0$ in co-rotating plasma and $E_r^{lab} < 0$ in counter-rotating plasma when $E_r^{rot} = 0$. This is usually the case in the tokamak experiment.

With presence of the centrifugal force, the sum of the potential energy derived by the centrifugal force and the kinetic energy is conserved [7]:

$$\mathcal{E} = \frac{1}{2}m_Z(v^2 - R^2\Omega_*^2), \quad (1)$$

$$\Omega_* = \Omega\left[1 - \frac{Zm_iT_e}{m_Z(T_i + T_e)}\right]^{1/2},$$

where m_i denotes the mass of bulk ion. The Ω_* is the effective rotation angular frequency, or modification of Ω considering the electric field along the major radius direction generated by non-uniform density distribution of bulk ions on the flux surface due to the centrifugal force.

The drift velocity is given by as follows, taking into account effects of the centrifugal force and the Coriolis force [6]:

$$v_d = \frac{m}{ZeR_0B_0}\left[\left(v_\parallel{}^2 + \frac{v_\perp{}^2}{2}\right) + \Omega_*{}^2R^2 + 2v_\parallel\Omega R\right]. \quad (2)$$

The velocity parallel to the magnetic field is determined by conservation of $\mathcal{E}$ in eq. (1) in addition to the conservation of magnetic moment μ.

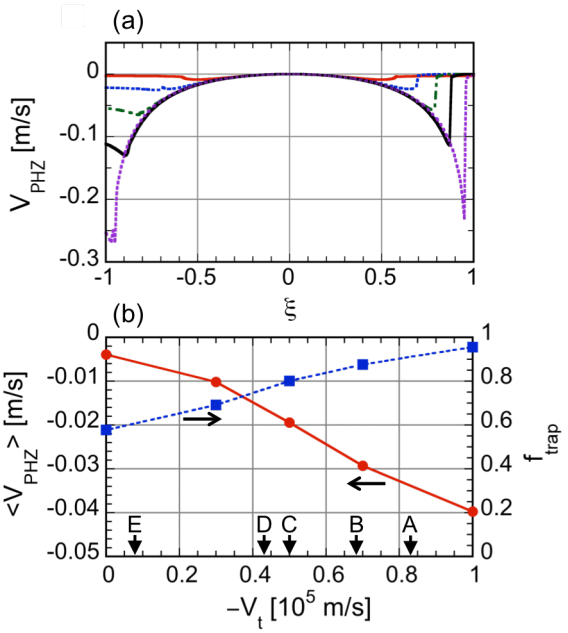

Fig. 2. (a) The PHZ pinch velocity V_{PHZ} as a function of pitch angle parameter ξ, for toroidal plasma rotation velocities of 0 m/s (red solid line), -0.3×10^5 m/s, -0.5×10^5 m/s, -0.7×10^5 m/s and -1×10^5 m/s (purple dotted line). (b) The PHZ pinch velocity averaged over the pitch angle $<V_{PHZ}>$ (red solid line) and the fraction of trapped particles f_{trap} (blue dotted line) as a function of the toroidal plasma rotation velocity. The symbols "A" to "E" denote the values observed in the JT-60U experiment and used in the simulation in [3].

The analysis was done for the W ions with the thermal speed (4.58×10^4 m/s) at $r/a = 0.76$ in JT-60U plasmas shown in [1]. The PHZ pinch velocity is shown in Fig. 2 (a) as a function of ξ for counter-rotating plasmas. The V_{PHZ} becomes larger with increase in the counter toroidal rotation speed. The fraction of trapped particles also becomes larger with increase in the counter toroidal rotation speed as shown by the dotted line in Fig. 2 (b), which is caused by the effect of the centrifugal force on $\mathcal{E}$ and then on $v_{\parallel}$ shown in eq. (1). The PHZ pinch velocity averaged over ξ becomes larger with increase in the counter toroidal rotation speed as shown in Fig. 2 (b). The $\langle V_{PHZ} \rangle$ changes by a factor of 5 within the range of the plasma rotation observed in the JT-60U experiments as shown by symbols A to E in Fig. 2 (b).

It should be noted that the equation of motion in the laboratory frame would also lead to the same results as those in this study where the equation of motion in the rotating frame is employed. The work done by the radial electric field on particles moving along the minor radius changes the kinetic energy of particles as done in eq. (1). The vertical drift velocity given by eq. (2) agrees with the usual drift velocity if the effect of the electric field along the major radius direction, generated by the non-uniform distribution of bulk ions on the flux surface due to the centrifugal force, is taken into account.

4. Summary

The PHZ pinch model has been improved by introducing the distribution of the velocity pitch angle and effects of the bulk plasma rotation on the particle orbit (the centrifugal force and the Coriolis force). It was found that the PHZ pinch velocity is large for particles with larger orbit width such as the barely trapped particles. The PHZ pinch velocity averaged over the pitch angle becomes larger with increase in the plasma rotation velocity as observed in the original PHZ model. We plan to extend the revised PHZ pinch model to include the radial electric field and then introduce it into the TOTAL code to simulate transport of the high Z impurity in rotating plasmas.

Acknowledgments

The authors are grateful to Drs. N. Hayashi, K. Hoshino, T. Nakano and M. Honda for fruitful discussion on the PHZ pinch model and on the JT-60U experiment data. This work was carried out under National Centralized Tokamak Collaboration Research Program in JAEA. This work was supported by JSPS KAKENHI Grand Number 25420895.

References

[1] T. Nakano, et al., J. Nucl. Mater. **415**, S327-S333 (2011).
[2] K. Hoshino, et al., Nucl. Fusion **51**, 083027 (2011)
[3] Y. Shimizu, et al., Plasma Fusion Res. **10**, 3403062 (2015).
[4] C. Angioni, et al., Nucl. Fusion **54**, 083028 (2014).
[5] Y. Shimizu, et al., submitted to Plasma Fusion Res.
[6] K. L. Wong, et al., Phys. Fluids **B 1** 545 (1989).
[7] K. G. McClements, et al., Plasma Phys. Control. Fusion **51**, 115009 (2009).